Effect of Airfoil Design Parameters and Particle Impact Induced Surface Roughness on Dynamic Stall

By

Jessica G. Shum

DISSERTATION

Submitted in partial satisfaction of the requirements for the degree of

DOCTOR OF PHILOSOPHY

in

Mechanical and Aerospace Engineering

in the

OFFICE OF GRADUATE STUDIES

of the

UNIVERSITY OF CALIFORNIA

DAVIS

Approved:

Prof. Seongkyu Lee, Chair

Prof. Zhaodan Kong

Prof. Vinod Narayanan

Committee in Charge

2024

Contents

Effect of Airfoil Design Parameters and Particle Impact Induced Surface Roughness on Dynamic Stall

Abstract

Dynamic stall is a prevalent phenomenon affecting the aerodynamic performance of a wide array of fluid-dynamic machinery, including maneuvering aircraft, fighter jets, helicopters, and wind turbines. The dynamic stall process induces sudden and undesirable variations in aerodynamic forces and pitching moments, critically affecting the controllability and structural integrity. The characterization of dynamic stall is still an arduous and complicated challenge.

This research investigates the effect of airfoil design parameters, effect of airfoil trailing-edge morphing, and the effect of particle induced surface roughness on dynamic stall through the use of high-fidelity computational fluid dynamics (CFD). OVERFLOW Reynolds-averaged Navier-Stokes (RANS) CFD and delayed detached eddy simulations (DDES) CFD are used to simulate the pitching and ramp-up motion of the airfoil undergoing dynamic stall. An airfoil morphing method investigation involving six parametric airfoil design parameters, including the camber, thickness, thickness crest position, leading-edge radius, trailing-edge camber, and boat-tail angle, is undertaken. The CFD numerical simulations are validated against experimental data for analyzing the aerodynamic loading, which includes the coefficient of lift, drag, and pitching moment. Then, the peaks of these coefficients are compared to identify the trends. Morris' sensitivity analysis is also used to analyze the effects of the different design parameters and further rank and assess their relative influences on the dynamic stall characteristics. Overall, it is found that the thickness crest position has a sizable influence on all the dynamic stall characteristics. Additionally, it is found that the design parameter that modifies the trailing-edge (boat-tail angle) is able to to markedly diminish the pitching moment, while concurrently sustaining a comparable lift coefficient. The complex features of the dynamic stall development stages and flow physics are further analyzed. The study reveals that morphed trailing-edge airfoil with the largest positive selected boat-tail angle design parameter causes the laminar separation bubble (LSB) to burst at an earlier stage, resulting in the dynamic stall vortex (DSV) occurring at an earlier stage. Mainly, the results indicate that morphed trailing-edge airfoils exhibit stronger secondary shear layer separation in the middle and aft airfoil sections at higher angles of attack (AoAs), compared to the baseline airfoil. Finally,

the effects of particle impact induced surface roughness are examined. Lawrence Livermore National Laboratory's (LLNL) code called ParticleTSim is used to obtain the particle strike maps to record the range of particle strikes during the dynamic stall motion. A comparison study between different roughness height values and impacted surface areas is performed. The results illustrate that, as the surface roughness height and impacted surface roughness area increase, the dynamic stall progression stages develop much quicker, the stall behavior occurs at an earlier AoA, and the accumulation of kinetic energy above the airfoil diminishes. This research dissertation ventures into the comprehension and mitigation methods for the adverse ramifications of dynamic stall.

Acknowledgments

I would like to express deep appreciation to my advisor, Prof. Seongkyu Lee for his patience, guidance, and support in teaching me about research in aerospace engineering, fluid mechanics, dynamic stall, and CFD. I have known Professor Lee since I was an undergraduate student. I am grateful that Professor Lee has taught me about the importance and significance of having an advanced education and encouraged me to further my education and pursue a PhD degree. I would like to thank Prof. Zhaodan Kong and Prof. Vinod Narayanan for serving on my dissertation committee and PhD qualifying exam committee, and for their help and support throughout my undergraduate and graduate school years. I would also like to thank Prof. Jean-Pierre Delplanque and Prof. Wolfgang Kollmann for attending my PhD qualifying exam, and for their mentoring and advising throughout my graduate school years.

Additionally, I would like to thank my mentors at Lawrence Livermore National Laboratory (LLNL), Dr. Rose McCallen and Dr. Kambiz Salari for providing me with the opportunities, including internships, student employee positions, and Academic Collaboration Team (ACT) Awards Program, and for their valuable suggestions and resources for my research. I am also grateful for the guidance, instruction, and support provided by my other mentors at LLNL, including Dr. Jeremy White, Dr. Daniel Taller, Dr. Willow Wan, and Dr. Stephen Moon. Furthermore, I would like to thank my mentors at Sandia National Laboratories (SNL), Dr. Ethan Hecht, and Dr. Myra Blaylock for mentoring me during my summer internship at SNL and for supporting my future academic and professional endeavors.

Finally, I would also like to acknowledge and thank the financial support (TA-ship tuition fee remissions) from the MAE Department. Being a Teaching Assistant (TA) and Associate Instructor (AI) were immensely rewarding and enjoyable experiences during my graduate school years. Thank you to everyone for supporting me in this journey to complete my PhD degree and for making this achievement possible!

Nomenclature

a speed of sound, $\frac{m}{s}$

c chord, m

C_d drag coefficient, $\frac{D}{qA}$

C_f skin friction coefficient, $\frac{\tau_w}{qA}$

C_l lift coefficient, $\frac{L}{qA}$

C_m pitching-moment coefficient, $\frac{M}{qA}$

C_p pressure coefficient, $\frac{P-P_\infty}{q}$

D drag, N

k reduced frequency, $\frac{\omega c}{2U}$

L lift, N

M pitching moment, $N-m$

Ma Mach number, $\frac{U}{a}$

P pressure, $\frac{N}{m^2}$

q dynamic pressure, $\frac{1}{2}\rho U^2$

Re Reynolds number, $\frac{Uc}{\nu}$

t time, s

U, V freestream velocity, $\frac{m}{s}$

x distance, m

x/c nondimensional chord length location

y^+ dimensionless wall distance

Greek Symbols

α angle of attack, deg

μ dynamic viscosity, $\frac{kg}{ms}$

ν kinematic viscosity, $\frac{m^2}{s}$

ρ air density, $\frac{kg}{m^3}$

τ_w wall shear stress, Pa

ω rotational frequency, $\frac{rad}{s}$

List of Figures

List of Tables

CHAPTER 1

Introduction

1.1. Background and Motivation

This section provides a brief introduction into the background and motivation of dynamic stall and computational fluid dynamics (CFD). The subsequent chapters will provide a detailed literature review related to the specific research topics in dynamic stall and the CFD approaches and methods.

1.1.1. Dynamic Stall. Maneuvering wings or aircraft that undergo rapid unsteady motion, such as pitching, flapping, and plunging, are characterized by intricate unsteady flow patterns associated with dynamic stall. Existing literature has shed light on various aspects of dynamic stall, including its regimes, characteristics, and unsteady flow patterns. During the dynamic stall motion, the angle of attack (AoA) of the airfoil goes beyond the static stall angle. The dynamic stall phenomenon is initially developed by a delayed boundary-layer separation coupled with the accumulation of circulation. This phase is followed by an abrupt commencement of unsteady separation that reaches its peak with the creation of a large-scale dynamic stall vortex (DSV). The shedding of the DSV from the leading edge and its subsequent movement along the airfoil induce abrupt variations in aerodynamic forces and pitching moments, critically affecting controllability, vibrations, structural integrity, and noise generation. During a dynamic stall process, various flow structures leave their pressure footprints on a wing surface. Accordingly, the surface pressure evolution during dynamic stall are able to aide in assessing the development of different flow stages and predict critical flow events during this process. Figure 1.1 includes examples of the simulation frames showing changes in the pressure coefficients to illustrate certain stages of the dynamic stall upstroke pitching motion. The characterization of dynamic stall is an arduous and complicated challenge. The improvement in dynamic stall prediction techniques for modeling unsteady air loads is important in the development of future technology. Dynamic stall is a prevalent phenomenon in a wide array of engineering applications, influencing the aerodynamic performance of numerous fluid

dynamic machinery, including winged space vehicles, maneuvering aircraft, fighter jets, helicopters, wind turbines, and gust encounters [8, 9, 13, 26, 34, 55, 68, 102]. In many instances, dynamic stall is the limiting performance factor of these associated vehicles and structures.

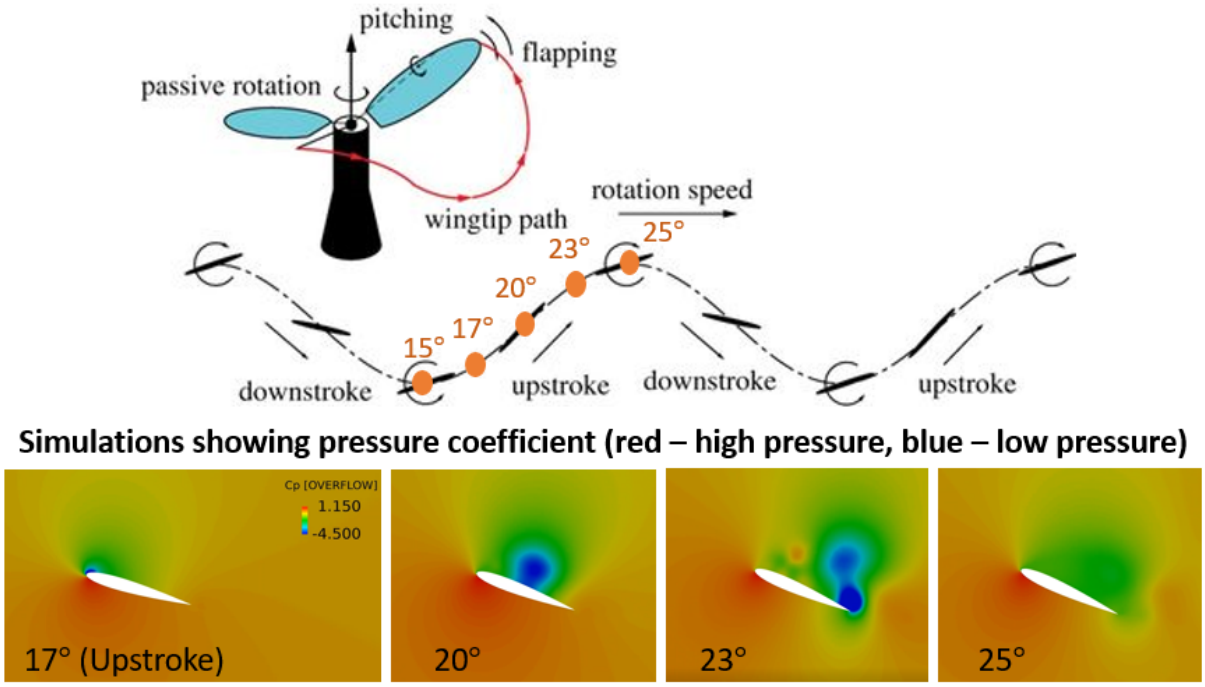

FIGURE 1.1. Stages of the dynamic stall pitching motion [54, 86]

Other works have provided a great deal of information on the dynamic stall regimes and their unsteady flows, wake and viscous effects, and stall flutter effects [8,26,53,68,69,102]. Furthermore, other techniques and experiments like flow visualization [66], surface pressure [14], particle image velocimetry (PIV) [103], and interferometry [20] have been performed to analyze the different phases of dynamic stall. The significance of this subject has motivated an extensive body of work for the past several decades and continues to be an active research topic today.

The topic of dynamic stall is technologically important due to the motivation and necessity to develop more robust and powerful next-generation flight vehicles. In my PhD research work, I have studied the effect of airfoil design parameters, effect of airfoil trailing-edge morphing, and the effect of particle-induced surface roughness on dynamic stall. Specifically, I have analyzed the aerodynamic loading characteristics and flow physics of dynamic stall with the objective of finding ways to better understand and mitigate the adverse ramifications of dynamic stall.

1.1.2. Computational Fluid Dynamics (CFD). Computational fluid dynamics (CFD) is one of the largest users of high-performance computing (HPC) applications [11]. HPC uses supercomputers and computer clusters to solve advanced computation problems. HPC had led to significant advances in CFD numerical simulations for engineering flows. CFD is a branch of fluid mechanics that uses numerical analysis, algorithms, and data structures to analyze and solve problems that involve fluid flows. The CFD methods and modeling approaches can also be applied to research and further investigate the complex physics of fluid flow problems in mechanical and aerospace engineering subject areas.

CFD produces predictions based on the conservation laws (conservation of mass, momentum, and energy) governing fluid motion. These predictions occur under the conditions defined in terms of the flow geometry (e.g. airfoil, wing), the physical properties of a fluid, and the boundary and initial conditions of a flow field [35]. CFD is a well-established methodology used in engineering for design and analysis. Additionally, CFD has been a crucial component in developing updated designs through computational simulations for research purposes. In my research, I have examined the effect of airfoil design parameters, trailing-edge morphing, and surface roughness on dynamic stall. The CFD methodology provides a way to simulate and visualize the results without undertaking a real commitment to execute the physical experiment or any other design alterations. This is a great advantage and the experiment is now done through a computer resulting in lower operating costs and enhanced efficiency. A computer model is created, and computer programmers code the equations representing the physical laws that govern the flow of the molecules of fluid. Then, the CFD results are output into files that can be visualized and analyzed [100]. CFD is a common computational method that has been extensively used for prediction of airfoil dynamic stall [25]. I have been using NASA's OVERFLOW CFD code [72] for simulating the results in my research. This CFD code enables the detailed characterization of fluid flow. The numerical simulations in my research involve Reynolds-averaged Navier-Stokes (RANS) CFD [76] and detached eddy simulations (DES) [93]. The DES is a useful hybrid model between RANS and large eddy simulations (LES), in which RANS is invoked in the boundary layers near the solid surfaces and LES is outside the boundary layers. DES surpasses traditional RANS on the basis of accuracy, and surpasses traditional LES on the basis of computational cost. Later, a modification to the DES modeling concept led to the development of delayed detached eddy simulations (DDES) [92] for improved

accuracy. Once the CFD simulations have completed, the next steps are to analyze and interpret the obtained simulation results. It is mandatory to perform the post-processing calculations and to construct relevant graphs, contours, and visualizations for analysis. Therefore, I subsequently use Tecplot's FieldView Postprocessor, FORTRAN, and MATLAB to postprocess and visualize the CFD results.

1.2. Research Goals and Objectives

The ultimate goal of my PhD research is to advance the fundamental knowledge of the effect of airfoil design parameters and harsh environments on dynamic stall. It is known that dynamic stall limits the performance and speed of rotorcraft and other flight vehicles. The purpose of my research is crucial to overcoming and controlling the dynamic stall problem in some of the most extreme operating conditions to ensure the safety and security of flight vehicles for faster and longer range flight. The specific goals of my PhD dissertation are outlined below:

- Advance the fundamental knowledge of the effect of airfoil design parameters (airfoil shapes) in deep dynamic stall scenarios using a newly developed airfoil parameterization method (PARFOIL).
- Analyze how each airfoil design parameter influences the dynamic stall aerodynamic loading characteristics (coefficients of lift, drag, and moment) and perform a sensitivity analysis (Morris' method) to rank and assess the quantitative effects of these design parameters on the dynamic stall characteristics.
- Examine the significance and benefits of trailing-edge morphing on mitigating the effects of dynamic stall. Specifically, this includes investigating the local flow characteristics of the trailing-edge separation vortex and its effect on delaying the bursting of the LSB.
- Analyze the detailed flow physics (including the DSV formation, vorticity and flow contours, velocity fluctuations, and surface pressure and skin friction coefficients) during the dynamic stall stages to understand the effect of airfoil morphing on the dynamic stall characteristics.
- Investigate the effects of particle impact induced surface roughness on dynamic stall and obtain the particle strike maps using Lawrence Livermore National Laboratory's (LLNL) code called ParticleTSim.

- Analyze the changes in the aerodynamic loading characteristics and the detailed flow physics during the dynamic stall stages to understand the effect of particle impact induced surface roughness on the dynamic stall process.

1.3. Outline of Thesis

This PhD dissertation includes five chapters and an Appendix that summarize my developed and published research works. Chapter 1 starts with an introduction of my research topic and methods. This includes the background and motivation for my research in dynamic stall, an overview of the methods and purposes of CFD, and my research goals and objectives. Chapters 2, 3, and 4 are the main content chapters of this dissertation. Each of these chapters respectively include an extensive literature review for the specific research subject. Chapter 2 discusses the research work done on analyzing the effect of airfoil design parameters on dynamic stall. This chapter goes over the airfoil design morphing method and numerical scheme, an provides the numerical results and analysis for the dynamic stall characteristics of the six airfoil design parameters (camber, leading-edge radius, thickness, thickness crest position, boat-tail angle, and trailing-edge camber). Then a sensitivity analysis is conduced to find the most influential design parameters. Chapter 3 further investigates the effect of one of the airfoil design parameters (boat-tail angle) on dynamic stall. This chapter explores the profound effects of trailing-edge morphing on dynamic stall. The methodology and numerical results and analysis on the aerodynamic loading characteristics, dynamic stall stages and development, and general flow physics are presented and examined. Chapter 4 studies the effect of particle impact induced surface roughness on dynamic stall. This chapter goes over the methodology for relating surface impact and surface roughness. The numerical results include the particle impact strike maps, and a detailed analysis and discussion on the aerodynamic loading characteristics, dynamic stall stages and development, and flow physics and energy. Chapter 5 concludes the findings of the research topics presented in this dissertation while highlighting the significance of the research results. This chapter also provides some recommendations for future works and a description of the other works that were completed during my graduate school years. Chapter 6 contains a complete list of my publications, many of which are directly associated with the content chapters of this dissertation. More information and results associated with these topics are described in the subsequent corresponding chapters.

CHAPTER 2

Effect of Airfoil Design Parameters

2.1. Introduction

It is known that the characterization of dynamic stall is still an arduous and multifaceted challenge. Though there has been progress in understanding these concepts, the characterization of dynamic stall still continues to be a challenging and complex problem. This is due to the complexity of the unsteady flowfields, the different types of pitching motions, and the combinations of the freestream conditions (i.e. Mach number and Reynolds number). Additionally, there is a lack of a method or mechanism that can be used to analyze the effects of different airfoil geometry parameters on dynamic stall results. Airfoil shapes can significantly alter the behavior of dynamic stall. In particular, airfoil morphing has been used to delay dynamic stall. For example, alterations in the shape of the leading edge have pronounced effects on pressure distribution, flow trajectories, separation phenomena, and reattachment processes [26]. Barger [3] outlined several procedures to design lower-pitching airfoils through modifying different parameters of the airfoil, including the leading edge. It has been posited that enhanced roundness of the leading edge could potentially lead to a postponement in the separation of the leading edge, culminating in the delayed formation of dynamic vortices. Carr and McAlister [12] investigated the effect of a leading-edge slat on the dynamic stall of an oscillating airfoil and analyzed the associated flow behavior and DSV movement. Furthermore, an aerodynamically streamlined and variably drooping leading edge demonstrated a superior maximum lift coefficient compared to the reference airfoil, whilst significantly reducing the negative pitching moment [45]. Similar passive flow control methods have also been applied to improve the aerodynamic performance and control dynamic stall for wind turbine airfoils [21, 56, 57]. De Gaspari et al. [23] evaluated the aerodynamic performance of morphed wings using different models and shape designs. In their study, they performed leading-edge and trailing-edge shape optimizations to design a compliant mechanism that meets both kinematic (motion) and structural (load-carrying) requirements. In another notable study, Sharma and Visbal [82] explored

the influence of airfoil thickness on the initiation of dynamic stall. Their investigation revealed that the mechanisms underlying the onset of dynamic stall differs with incremental changes in airfoil thickness. Collectively, these studies underscore the premise that variations in the geometric parameters of an airfoil, or a combination of these parameters, can result in significantly different dynamic stall behaviors.

In other recent developments, an aerodynamic shape optimization approach was used to mitigate and postpone the onset of dynamic stall. Raul and Leifsson [75] utilized cokriging metamodeling to estimate objective and constraint functions and engaged PARSEC parameters [91] as design variables for airfoil shape optimization to delay the dynamic stall events. With advanced turbulence and transition closures and improvements in high performance computing, Visbal and Benton [101] have developed improved flow control strategies to characterize the delay of dynamic stall on a pitching airfoil and its flow physics for stability analysis. Glatz et al. [29] used full-order solutions generated by the OVERFLOW CFD code and a surrogate-based recurrence framework (SBRF) to mimic full-order solutions of unsteady lift, drag, and moment coefficients at a reduced cost. Tran and He [97] have performed simultaneous optimization considering airfoil shapes and propeller parameters to achieve drag reduction over a wide range of Reynolds and Mach Numbers applicable to unsteady wing-propeller aerodynamic design. Many parameterization methods exist for airfoil shape morphing, and each method has distinct applications. Recently, Lim [59,60] developed a novel parametric airfoil design tool, named PARFOIL, and integrated it into a framework for rotor optimization. This parameterization technique is capable of altering eight distinct design parameters from a baseline airfoil, including the camber, camber crest position, thickness, thickness crest position, leading-edge radius, trailing-edge camber, trailing-edge camber crest position, and boat-tail angle. This new airfoil parameterization method would offer a valuable opportunity to study how dynamic stall behaviors change according to each separate airfoil design parameter or a combination of these parameters.

Many of these earlier works have only focused on a limited topic in airfoil design and morphing. Further exploration in other design concepts and methods, and on the holistic effects of airfoil morphing on dynamic stall is necessary. The objectives of this chapter are to incorporate the PARFOIL technique in predicting the dynamic stall phenomena, and to analyze the influence of various airfoil design parameters on aerodynamic performance and dynamic stall characteristics

using high-fidelity computational fluid dynamics (CFD). This chapter also seeks to further explore and examine the role of the most important design parameter in mitigating the adverse effects of dynamic stall. Lastly, this chapter undertakes a sensitivity analysis of these design parameters by employing Morris' method to evaluate their relative contributions through quantitative metrics.

2.2. Methodology

This section provides an overview of the methodology and solution approach employed in this chapter. In the subsequent subsections, the details of the OVERFLOW CFD and governing equations, Reynolds-Averaged Navier-Stokes (RANS) equations, the PARFOIL method, mesh generation, and boundary conditions and numerical schemes are presented.

2.2.1. OVERFLOW CFD and Governing Equations. The simulations and results in the chapters of my PhD research work utilize the OVERFLOW 2.3 structured computational fluid dynamics (CFD) solver [72], a time-marching implicit Navier-Stokes code that employs structured overset grid systems. This CFD code is proficient in calculating both time-accurate and steady-state solutions, offering a range of options for temporal and spatial discretization. The OVERFLOW code has widespread applications and has been extensively used in the investigation and prediction of unsteady 2-D and 3-D dynamic stall flows [4, 16, 37, 86, 87, 88], as well as in rotorcraft simulations [38, 39, 40, 41, 42, 78, 79].

OVERFLOW 2.3 [72] solves the Navier-Stokes equations in generalized coordinates. The Navier-Stokes equations are written in vector form with respect to a generalized coordinate system:

$$\frac{\partial \vec{q}}{\partial t} + \frac{\partial \vec{E}}{\partial \xi} + \frac{\partial \vec{F}}{\partial \eta} + \frac{\partial \vec{G}}{\partial \zeta} = 0 \tag{2.1}$$

where $\vec{q}$ is a vector of conserved variables, and ξ, η, and ζ represent the generalized coordinates. The fluxes in each direction are signified as $\vec{E}$, $\vec{F}$, and $\vec{G}$. The vector of conserved scalars is shown as:

$$\vec{q} = V \begin{bmatrix} \rho \\ \rho u_1 \\ \rho u_2 \\ \rho u_3 \\ \rho e_0 \end{bmatrix} \tag{2.2}$$

where ρ, u_1, u_2, u_3, and e_0 are the unknown field variables of density, velocities, and total energy per unit mass, respectively. The control volume is indicated by the variable, V. A pseudo-time term is added to these linearized equations to allow for sub-iteration and faster iterative numerical schemes to be employed.

The linearized Euler implicit form of Eq. (2.1) including sub-iterations is given by

$$\left[I + \frac{\Delta\tau}{S_D}(\partial_\xi A + \partial_\eta B + \partial_\zeta C)]\right] \Delta q^{n+1,m+1} = \left[\frac{(1+\theta)\Delta\tau}{S_D \Delta t}(q^{n+1,m} - q^n) - \frac{\theta\Delta\tau}{S_D\Delta t}\Delta q^n + \frac{\Delta\tau}{S_D} RHS^{n+1,m}\right] \tag{2.3}$$

Here $\theta = 0$ for first order time differencing and $\theta = 1/2$ for second order time differencing. An artificial time term $\left(\frac{\Delta t}{(1+\theta)\Delta\tau}\right)$ has been explicitly added for dual time stepping. This term is not included when using the Newton sub-iterations. However, the cases presented in the chapters do include sub-iterations. The psuedo time ($\Delta\tau$) may vary throughout the flow field when a local time step is employed. The artificial time term must converge at each physical time step (i.e., $\Delta q^{n+1,m+1} = 0$) to assure time accuracy. The S_D term is defined as $\left(1 + \frac{(1+\theta)\Delta\tau}{\Delta t}\right)$ for dual time stepping and as $(1+\theta)$ for Newton sub-iterations. The two time steps are equal to each other and do not vary in the field for the Newton sub-iteration ($\Delta t = \Delta\tau$). The explicit viscous and inviscid fluxes are included in the term RHS given by

$$RHS = \frac{\partial \vec{E}}{\partial \xi} + \frac{\partial \vec{F}}{\partial \eta} + \frac{\partial \vec{G}}{\partial \zeta} \tag{2.4}$$

A detailed overview of the solution process and the user's manual of the OVERFLOW CFD code can be found in Ref. [72].

Note that the OVERFLOW CFD method and governing equations presented in this Sec 2.2.1 are also applicable to the following chapters and sections in this research dissertation.

2.2.2. Reynolds-Averaged Navier-Stokes (RANS) Equations. The simulations in this chapter use the Reynolds-averaged Navier-Stokes (RANS) numerical method to model flow [76, 95, 104]. The RANS capability is already available in the OVERFLOW [72] CFD code. In RANS, the instantaneous flow quantities are decomposed into their time-averaged and fluctuating quantities. This is a technique known as the Reynolds decomposition. In this case, the Reynolds decomposition refers to a solution involving the separation of the flow variable (e.g. velocity) into the mean (time-averaged) component and the fluctuating component. Hence,

$$u(x,t) = \overline{u}(x) + u'(x,t) \tag{2.5}$$

where $x = (x, y, z)$ is a position vector. Note that u, $\overline{u}$, and u' are used to represent the instantaneous, mean, and fluctuating terms respectively. Another aspect of these properties is that the mean of the fluctuating quantity is equal to zero ($\overline{u'} = 0$). Using the properties of the Reynolds operators, the Navier-Stokes equations of motions can be split into time-averaged and fluctuating components to derive the nonlinear RANS equations describing flow (expressed in tensor notation):

$$\rho\overline{u}_j\frac{\partial\overline{u}_i}{\partial x_j} = \rho\overline{f}_i + \frac{\partial}{\partial x_j}[-\overline{p}\delta_{ij} + 2\mu\overline{S}_{ij} - \rho\overline{u'_i u'_j}] \tag{2.6}$$

where the mean of the strain rate tensor, $\overline{S}_{ij}$, is given as:

$$\overline{S}_{ij} = \frac{1}{2}(\frac{\partial\overline{u}_i}{\partial x_j} + \frac{\partial\overline{u}_j}{\partial x_i}) \tag{2.7}$$

Equation 2.6 gives the momentum portion of the RANS results. The last term in the Eq. 2.6, $\rho\overline{u'_i u'_j}$, is a nonlinear term representing the Reynolds stress model. This term accounts for the anisotropic turbulence. Therefore, additional turbulence models are needed to account for this nonlinear term in the stress tensor. The complete and explicit details of the derivation of the RANS equations can be found in Refs [76, 95, 104]. The chosen turbulence model for the study

in this chapter is the $k-\omega$ Shear Stress Transport (SST) Model. Details will be discussed in Section 2.2.5.

2.2.3. PARFOIL. Lim [59] developed a parametric airfoil design tool, PARFOIL for rotor airfoil design. The airfoil geometry is parameterized using a number of design parameters in order to control or morph the airfoil coordinates. Unlike other parameterization methods, PARFOIL performs a parameterization starting from a baseline airfoil geometry and then morphs it into a desired airfoil geometry by modifying the design parameters: camber (m), camber crest position (p_0), thickness (t), thickness crest position (x_0), leading-edge radius (k), trailing-edge camber (n), trailing-edge camber crest position (y_R), and boat-tail angle (b), as shown in Fig. 2.1 [62].

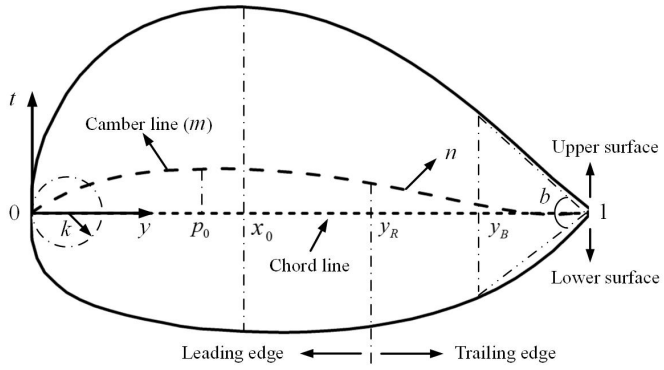

FIGURE 2.1. Diagram of airfoil coordinates with design parameters [62]

This new method has an improved feature since it takes an advantage of using the shape of the selected airfoil geometry and every design parameter also has a physical meaning. During the process, the grid points in the airfoil coordinates are redistributed using a Non-Uniform Rational Basis Spline (NURBS) interpolation [74]. As mentioned previously, PARFOIL originally contains eight design parameters, but this research work will only consider six of these design parameters. This includes the camber scaling factor (f_m), thickness scaling factor (f_t), leading-edge radius scaling factor (f_k), morphed thickness crest position (x_1), change in the trailing-edge camber (Δn), and change in the boat-tail angle (Δb). As shown in Fig. 2.1, a parameterization is performed for two regions: 1) a leading-edge region covering from the leading-edge to the camber crest, and 2) a trailing-edge region from the camber crest or a pre-defined point to the trailing edge. Liu and Lee have made minor adjustments to the PARFOIL equations [62] when they applied PARFOIL

for airfoil trailing-edge noise problems. Airfoil coordinates are typically represented by means of a polynomial [1, 49]. The definitions of these parameters are given in [59, 62].

In a parametric model, the camber m is modified by a scaling factor, f_m, that is multiplied to the baseline camber value, m_{BL}. This change scales the airfoil vertical coordinate in the camber. The updated camber can be expressed as follows:

$$m = f_m \cdot m_{BL} \tag{2.8}$$

In the above expression, a baseline airfoil is expressed with $f_m = 1$ (no change in camber) and a symmetric airfoil can be generated with $f_m = 0$ (zero camber). On the other hand, when a symmetric airfoil is used as a baseline, a small value of 0.0001c is added to the baseline camber value prior to scaling.

The alteration in thickness is similar to that of the camber. The updated thickness t can be obtained by multiplying the scaling factor, f_t, with the baseline thickness value, t_{BL}. This can be mathematically expressed as:

$$t = f_t \cdot t_{BL} \tag{2.9}$$

In the above expression, the baseline airfoil has a scaling factor $f_t = 1$ (no change in thickness).

The updated leading-edge radius, denoted as k, can also be obtained in a manner similar to the camber and thickness, by multiplying the scaling factor, f_k, with the baseline leading-edge radius value, k_{BL}. This can be mathematically expressed as:

$$k = f_k \cdot k_{BL} \tag{2.10}$$

In the above expression, the baseline airfoil has a scaling factor $f_k = 1$ (no change in leading-edge radius).

When there is a change in the position of the camber or thickness crest, the difference in the airfoil horizontal coordinate, denoted as Δy, is added to the baseline value for both the leading-edge and trailing-edge regions. The same polynomial function can be employed to describe the changes

in the airfoil coordinates for these two crest positions. For instance, the change in the position of the thickness crest can be mathematically represented as:

$$y_1 = y_0 + \Delta y \tag{2.11}$$

where y_1 represents the updated position of the thickness crest, and y_0 is the baseline position of the thickness crest.

When the trailing-edge camber undergoes a change in magnitude, denoted as Δn, the corresponding change in airfoil thickness, denoted as Δt_n, is added to the baseline vertical coordinates in the trailing-edge region. The updated trailing-edge camber in the morphed airfoil geometries can be mathematically expressed as:

$$t_n(y) = t(y) + \Delta t_n \tag{2.12}$$

where t_n represents the updated trailing-edge camber, and t is the baseline trailing-edge camber.

Similarly, when the boat-tail angle changes in magnitude (Δb), the thickness (t_b) due to a change in boat-tail angle is modified for the trailing-edge region as follows:

$$t_b(y) = t(y) + \Delta t_b \tag{2.13}$$

The aforementioned equations establish the relationships between the baseline airfoil geometry and the morphed airfoils, demonstrating the capability of PARFOIL to generate an extensive range of parametric airfoil geometries. For a more comprehensive understanding of the mathematical expressions and details for the design parameters, readers are encouraged to consult the references [59, 62]. Additional detailed equations for the thickness crest position, trailing-edge camber, and boat-tail angle design parameters are provided in Appendix A.

2.2.4. Mesh Generation. NASA's mesh software, OVERGRID [18], is employed for constructing the mesh, and it is compatible with Chimera grid tools [19]. The mesh of the 3-D airfoil

geometry is depicted in Fig. 2.2. An O-type grid, characterized by a rounded trailing edge, is utilized. The airfoil surface comprises 500 grid points in the chordwise direction, with 350 allocated on the upper surface and 150 on the lower surface. The distance of the far-field boundary is set at 100 times the chord length, measured from the airfoil surface. There are 100 points designated in the normal direction, where the half of the points are concentrated in the first chord length and the remaining ninety-nine chord lengths collectively share the other half. The spanwise extent of the model is equivalent to 10% of the chord length, with a distribution of 50 points that are uniformly spaced in the spanwise direction. The grid resolution is set as 0.05% of the chord length at the leading edge, and 0.02% of the chord length at the trailing edge. The first wall-normal grid height is calibrated to ensure that the non-dimensional wall distance, y^+, remains below 1. The grid resolutions were selected in adherence to best practices and conclusions derived from prior studies [37, 58, 86, 102]. Khalifa et al. [47] further asserted that 3-D results are more accurate in capturing dynamic stall phenomena due to their ability to resolve finer turbulence scales in highly separated flows. More information on the comparison between the 2-D and 3-D mesh results are included in Appendix B. Moreover, the equations from PARFOIL are integrated into the process to construct the meshes for the morphed airfoils.

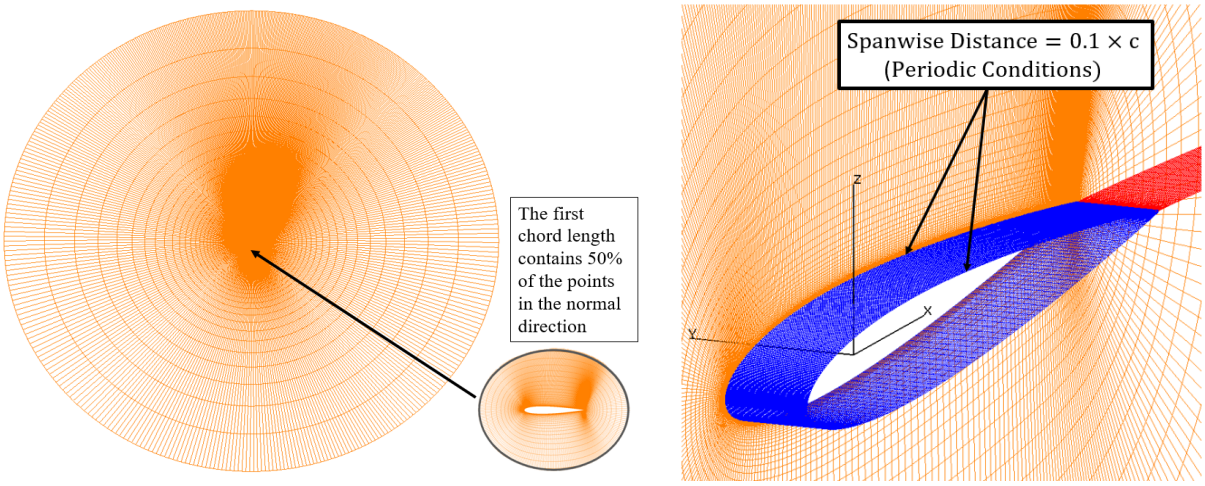

(a) (b)

FIGURE 2.2. 3-D overview of the airfoil section mesh (NACA 0012): (a) O-type mesh; (b) mesh near the airfoil surface and boundary conditions.

2.2.5. Boundary Conditions and Numerical Scheme. The following boundary conditions are prescribed and imposed: no-slip adiabatic condition on the airfoil surface, spanwise periodic

conditions, and periodicity in the chordwise direction at the trailing edge. The last boundary condition means that the solution remains the same across the line originating from the midpoint of the trailing edge and extending towards the far field. All of these listed boundary conditions are shown in Fig. 4.1.

The OVERFLOW [72] CFD solver was based on Reynolds-averaged Navier-Stokes (RANS). The fifth-order central difference spatial scheme and the second-order backward temporal scheme was implemented. A temporal resolution of 36,000 time steps per cycle and 10 sub-iterations was applied. The TLNS3D dissipation scheme with 2nd and 4th-order dissipation on RHS and LHS along with smoothing [58,86] was also used. The CFD cycle iterations are continued until the solutions are converged. The solutions usually take up to 4 cycles to reach convergence. Rumsey [77] stated that fully turbulent flow computations have shown inconsistent and undesirable results because there is a lack of transitional modelling. Hence, Rumsey argued that it is necessary to incorporate transitional modelling because the turbulent models will not kick in until some distance from the stagnation point. Jain et al. [37] also showed that the transitional turbulence model provides more accurate predictions of dynamic stall. More information on the comparison between the fully turbulent model and transition model simulation results are included in Appendix B. According to these recommendations, the correlation based two equation Langtry-Menter transition model [50] is used, which is based on the year 2003 version of Menter's shear stress transport (SST) model.

2.3. Numerical Results and Discussion

This section first shows the details and setup for the airfoil geometry and baseline test case. The validation of the numerical simulations against the experimental data for the baseline case are given. Then the aerodynamic loading results and peak coefficients for six of the design parameters are presented. This includes the camber scaling factor (f_m), leading-edge radius scaling factor (f_k), thickness scaling factor (f_t), thickness crest position (x_1), boat-tail angle (Δb), and trailing-edge camber (Δn). This section also explores the statistical analysis of all six design parameters and further investigates one of the most significant design parameters, the boat-tail angle.

2.3.1. Airfoil Geometry and Baseline Test Case. The NACA 0012 is selected as a baseline airfoil for the validation of numerical simulations and the airfoil shape morphing. This airfoil is

subjected to a pitching motion with a freestream Mach number of 0.3. The airfoil features a chord length of 0.61 meters, corresponding to a Reynolds number of 3.76×10^6, and undergoes oscillations as depicted in Eq. (2.14) [65]:

$$\alpha(t) = \alpha_0 + \alpha_a \sin(\omega t) \tag{2.14}$$

in which the mean angle of attack (α_0) is 15°, the oscillation amplitude is (α_a) is 10°, and ω, the angular frequency, is approximately 34.1 rad/s. In dynamic stall, the frequency is often used as a dimensionless number that defines the degree of unsteadiness in unsteady aerodynamics. The reduced frequency is described by Eq. (2.15) as follows:

$$k = \frac{\omega c}{2U_\infty} \tag{2.15}$$

in which c is the chord length, and U_∞ is the freestream velocity. In the current study, the reduced frequency is set to be 0.101.

2.3.2. Validation. The baseline validation test conditions were described in subsection 3.3.1. The OVERFLOW CFD predictions pertaining to the lift coefficient (C_l), drag coefficient (C_d), and moment coefficient (C_m) are depicted in Fig. 2.3. These results are compared with the experimental data obtained by McAllister et al. [67] corresponding to the baseline scenario. Note that the experimental data was ensemble-averaged. The conditions for the baseline validation test have been detailed in the previous section. The predictions exhibit a mildly oscillatory pattern in the downstroke region due to unsteadiness associated with flow separation, and the use of a deterministic model for a stochastic process. It is found that the magnitudes of the peaks are in close alignment with the experimental dataset. The stall AoAs exhibit a mean variation difference of 0.49% and the peak coefficients exhibit a mean variation difference of 11.7% across all aerodynamic loading coefficients between the experimental data and prediction for the baseline case. The corresponding C_l and C_m peak values for the six design parameters are presented in Figs. 2.4, 2.5, 2.6, 2.7, and 2.8, and 2.9.

2.3.3. Effect of the Camber. Figure 2.4(a) shows the airfoil geometry with a change in the airfoil camber. As the camber scaling factor (f_m) increases, the airfoil geometry shifts upwards. Figure 2.4(b) and (c) shows that the peak magnitudes of the lift and moment coefficients increase with an increase in the camber scaling factor. Likewise, the peak values' corresponding angle of attack (AoA), or stall AoA, also increases with increasing f_m value. For the coefficient of moment, as the camber scaling factor increases, the stall AoA increases, and the value of the coefficient of moment decreases, which indicates a higher negative pitching moment.

2.3.4. Effect of the Leading-Edge Radius. Figure 2.5(a) shows the airfoil geometry with a change in the airfoil leading-edge radius. As the leading-edge radius scaling factor (f_k) increases, the leading edge of the airfoil becomes wider. Generally, as the leading-edge radius scaling factor (f_k) increases, the magnitudes of the coefficient of lift and its stall AoA also increase.The results show that there is a more rapid increase in both the C_l and C_m stall AoAs from f_k of 0.2 to 1 (baseline). This behavior is shown in Fig. 2.5(b) and (c). For all of the cases, once the f_k scaling factor reaches 1.6, there is no longer a clear observable difference in the peak values and location of stall AoAs. One can conclude that the results for the f_k values above the baseline case (f_k=1) are less sensitive to change, and the change is even more minimal above f_k=1.6. Furthermore, the C_m peak values are relatively constant as the f_k value increases. Figure 2.5(c) shows a slight fluctuation in the C_m peak values but the values are quite close in magnitude such that the behavior can be considered to be relatively constant.

2.3.5. Effect of the Thickness. Figure 2.6(a) shows the airfoil geometry when there is a change in the airfoil thickness. As the thickness scaling factor (f_t) increases, the airfoil becomes thicker and the whole area of the airfoil increases. When f_t decreases, the airfoil becomes thinner and the whole area of the airfoil decreases. The minimum f_t value of 0.67 represents an airfoil thickness ratio of 8% and the maximum f_t value of 1.33 represents a thickness ratio of 16%. The baseline f_t value of 1 represents a thickness ratio of 12%. Figure 2.6(b) and (c) show that the results for the lift and moment stall AoAs steadily increase as f_t increases. After the baseline case, the C_l peak values alternate between rising rapidly and rising constantly. It can be seen that the C_l peaks for f_t of 1.083 and 1.17 are relatively constant, and the C_l peaks for f_t of 1.25 and 1.33 are also relatively constant. The C_m peak values are essentially constant. There is barely any

fluctuation in the C_m peak values since the maximum and minimum values range from -0.496 and 0.507, which is only a 2% fluctuation.

2.3.6. Effect of the Thickness Crest Position. Figure 2.7(a) shows the airfoil geometry when there is a change in the airfoil thickness crest position. As the thickness crest position (x_1) increases, the airfoil maximum thickness location moves in the trailing-edge direction of the horizontal coordinates and the thickness of the leading-edge geometry becomes narrower. The baseline x_1 value of 0.3 represents a maximum thickness location at $0.3c$. Figure 2.7(b) shows that both the C_l peak values and the stall AoAs decrease as the thickness crest position increases. Similarly, the stall AoA corresponding to the C_m peaks in Fig 2.7(c) also decreases as x_1 increases. In other words, as the thickness crest position decreases or as the maximum thickness moves to the leading edge, both the C_l peak and the stall AoA increase. Despite the small sinusoidal fluctuations shown in the C_m peak value trends, the C_m peak values are essentially the same at the maximum and minimum thickness crest positions.

2.3.7. Effect of the Boat-Tail Angle. Figure 2.8(a) shows the airfoil geometry when there is a change in the airfoil boat-tail angle. As the boat-tail angle (Δb) increases, the trailing edge of the airfoil becomes wider and the whole area of the airfoil increases. When Δb decreases, the trailing edge of the airfoil becomes narrower and the whole area of the airfoil decreases. Figure 2.8(b) and (c) show that the peak magnitudes of both the lift and moment coefficients decrease and there is barely any change in the location of their stall AoAs as the boat-tail angle increases. The magnitude of the coefficient of moment decreases more drastically compared to the coefficient of lift. Overall, the coefficient of lift is reduced by 2% while the coefficient of moment is reduced by 13% in the the range of the Δb from 0 to 2. This indicates that the use of the boat-tail angle is beneficial to reducing the dynamic stall effect without compromising the loss of lift too much.

2.3.8. Effect of the Trailing-Edge Camber. Figure 2.9(a) shows the airfoil geometry when there is a change in the airfoil trailing-edge camber. As the trailing-edge camber (Δn) increases, the trailing edge on the suction side of the airfoil becomes wider (bends outwards) and the trailing edge on the pressure side of the airfoil becomes narrower (bends inwards). Figure 2.9(b) shows that the magnitude of the coefficient of lift increases as the trailing edge camber increases. It can be seen that the C_l peaks rise rapidly in the negative Δn value range and steadily fluctuates upward

in the initial positive Δn value range. Once Δn reaches 0.0045, the C_l peak value rises rapidly again. Figure 2.9(c) shows that the magnitude of the coefficient of moment slightly and steadily increases as the trailing edge camber increases. The magnitude of the C_m peaks in the positive Δn value range moderately fluctuates as the trailing edge camber increases. There is also barely any change in the location of the lift and moment stall AoAs as the trailing-edge camber increases.

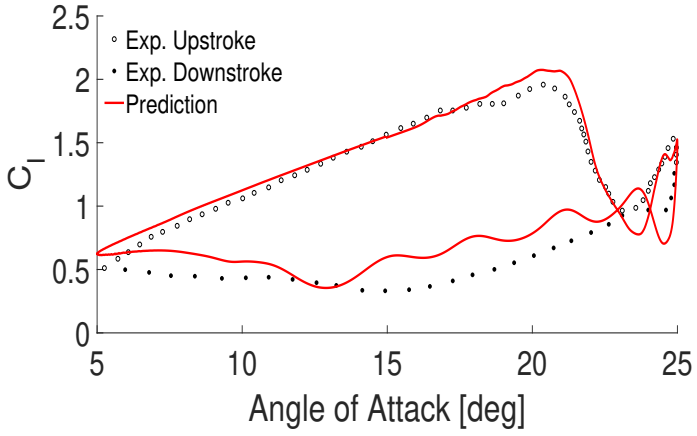

(a)

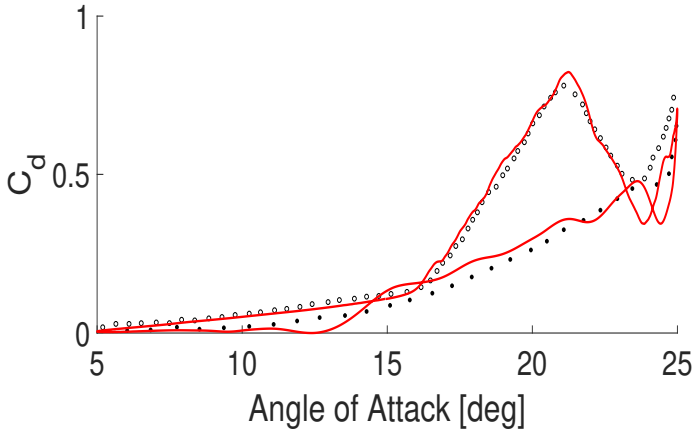

(b)

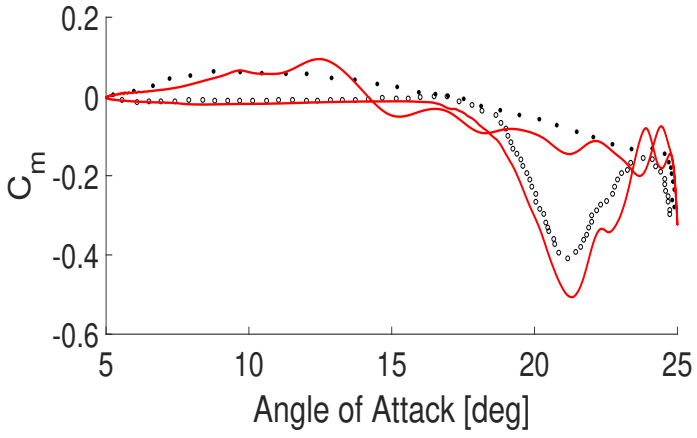

(c)

FIGURE 2.3. Aerodynamic loads for baseline airfoil undergoing a sinusoidal pitching motion: (a) coefficient of lift, (b) coefficient of drag, and (c) coefficient of pitching moment. Validation of simulations is made with Ref. [67]

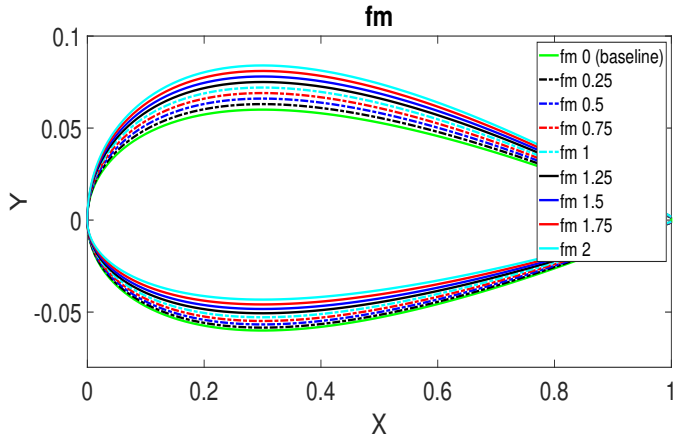

(a)

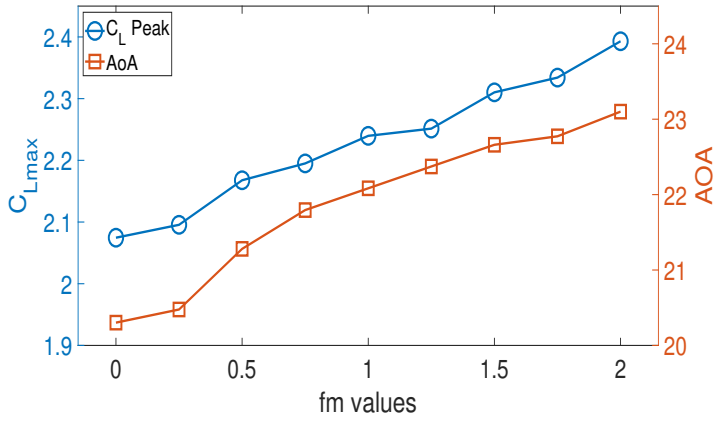

(b)

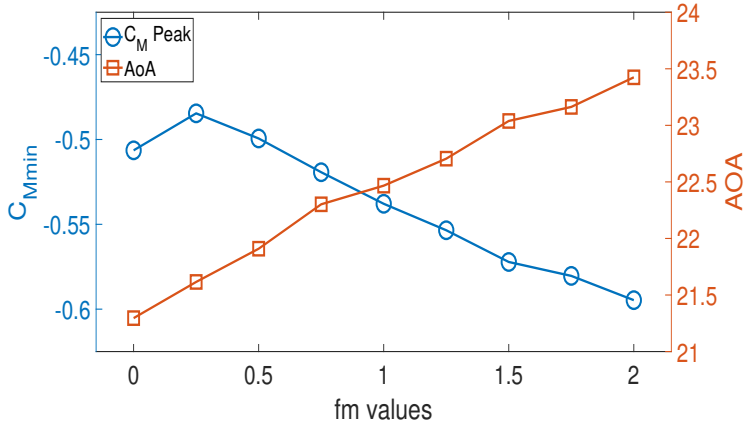

(c)

FIGURE 2.4. Effect of camber on airfoil dynamic stall: (a) airfoil geometry, (b) lift peak values, and (c) pitching moment peak values.

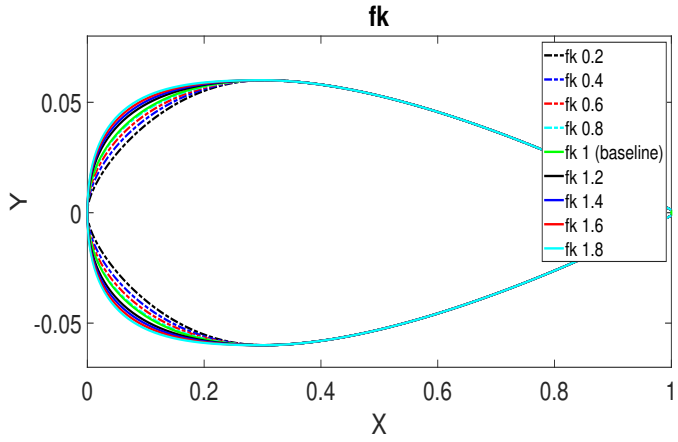

(a)

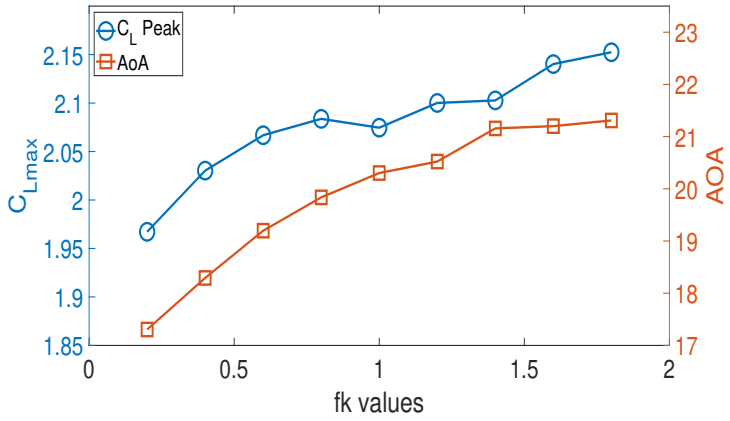

(b)

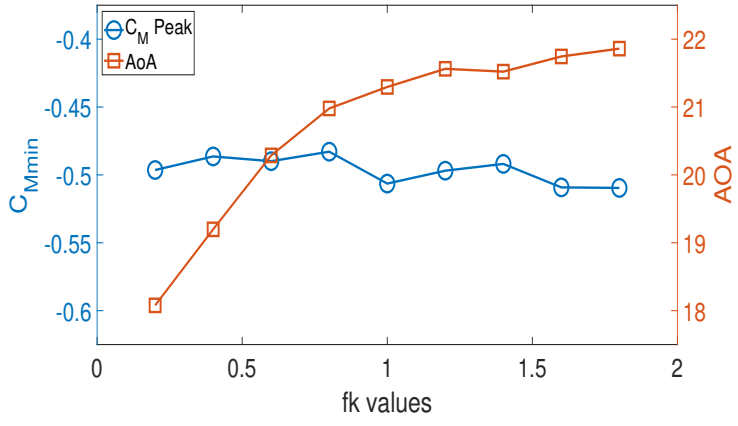

(c)

FIGURE 2.5. Effect of leading-edge radius on airfoil dynamic stall: (a) airfoil geometry, (b) lift peak values, and (c) pitching moment peak values.

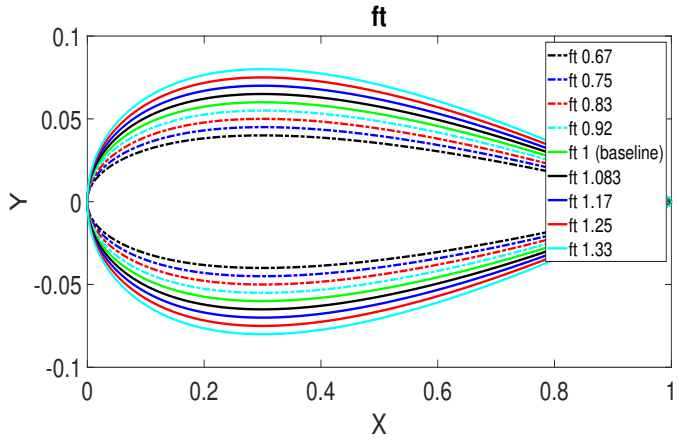

(a)

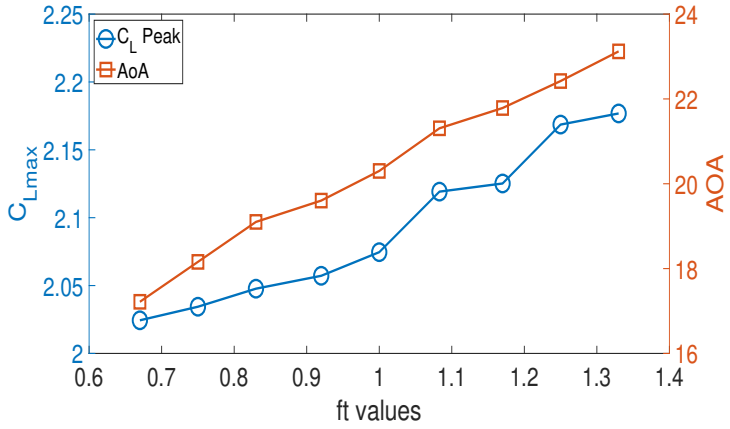

(b)

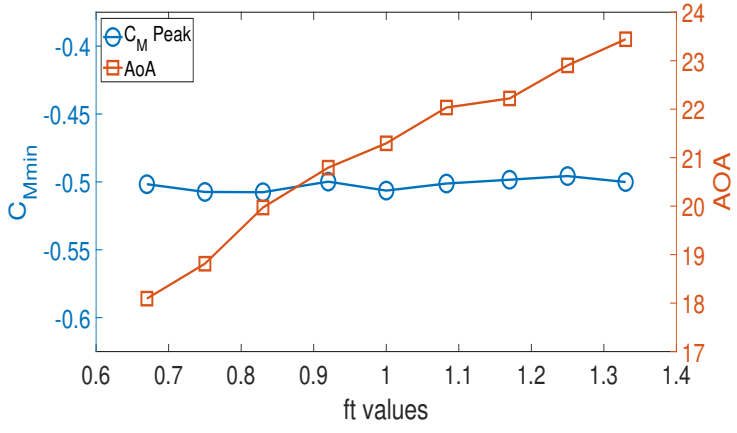

(c)

FIGURE 2.6. Effect of thickness on airfoil dynamic stall: (a) airfoil geometry, (b) lift peak values, and (c) pitching moment peak values.

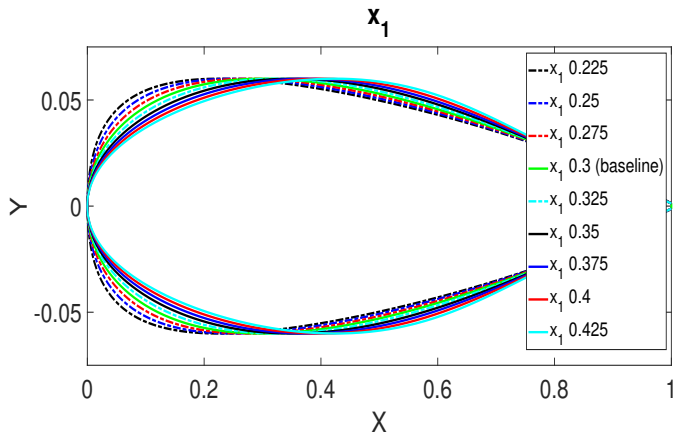

(a)

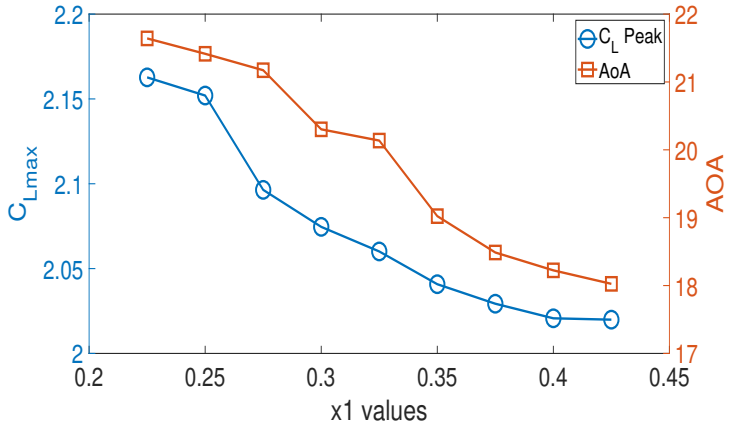

(b)

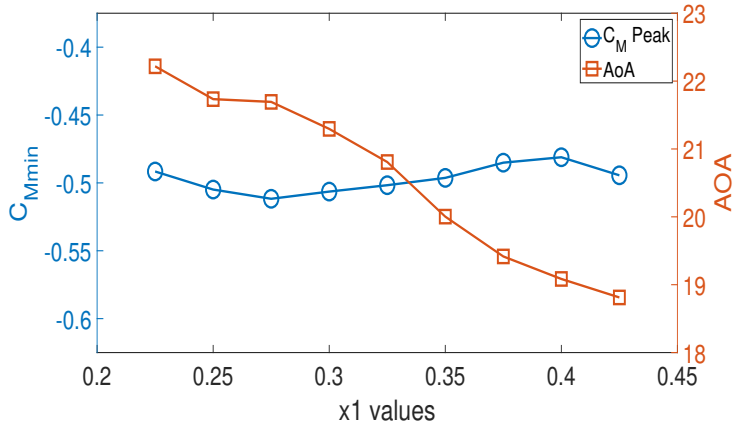

(c)

FIGURE 2.7. Effect of thickness crest position on airfoil dynamic stall: (a) airfoil geometry, (b) lift peak values, and (c) pitching moment peak values.

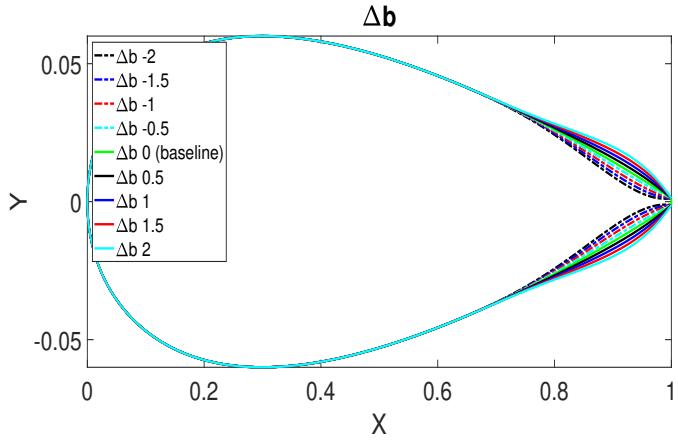

(a)

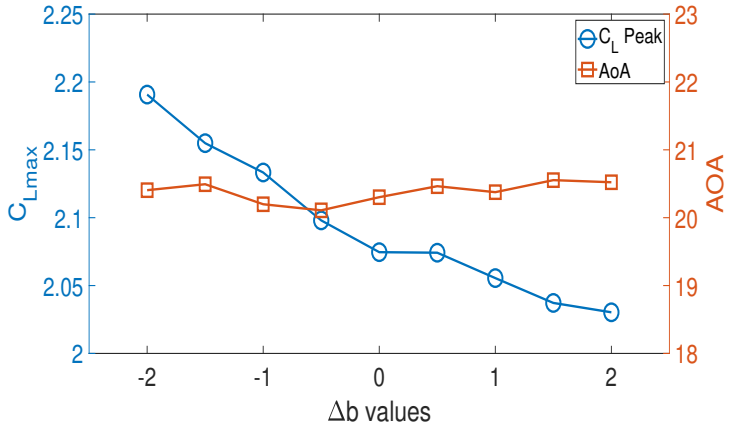

(b)

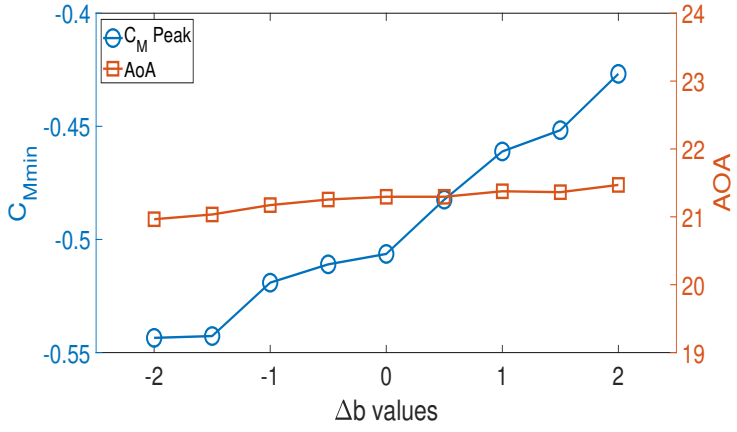

(c)

FIGURE 2.8. Effect of the boat tail angle on airfoil dynamic stall: (a) airfoil geometry, (b) lift peak values, and (c) pitching moment peak values.

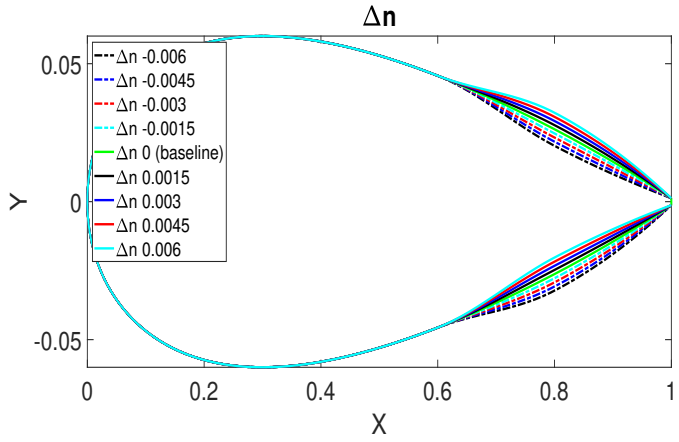

(a)

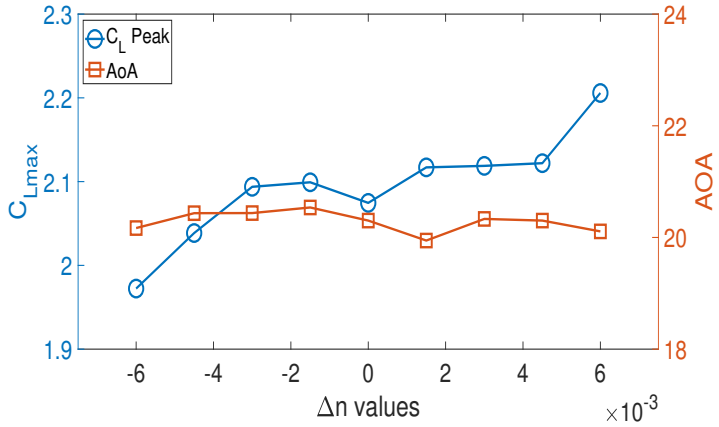

(b)

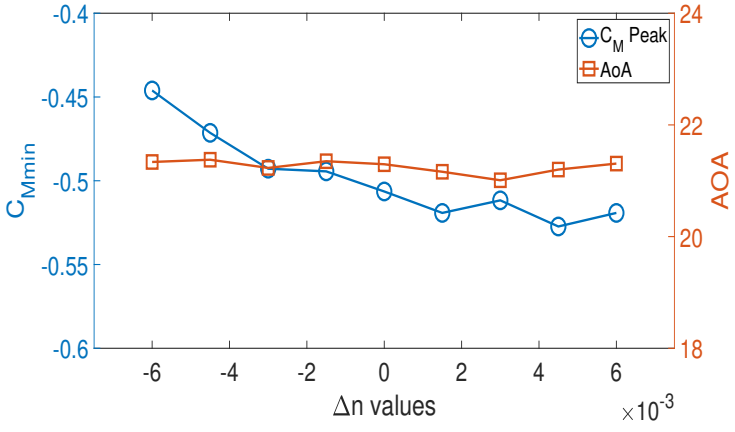

(c)

FIGURE 2.9. Effect of trailing-edge camber on airfoil dynamic stall: (a) airfoil geometry, (b) lift peak values, and (c) pitching moment peak values.

2.3.9. Comprehensive Statistical Analysis of the Airfoil Design Parameters. Figure 2.10 summarizes the range of the airfoil geometries for all six design parameters. The baseline airfoil, and the upper and lower bounds of the scaling factors for all six design parameter are shown in the figure. The bounds for all of the design parameters are spaced in eight equal increments. As discussed previously, these parameters include the camber scaling factor (f_m), leading-edge radius scaling factor (f_k), thickness scaling factor (f_t), thickness crest position (x_1), variation in the trailing-edge camber (Δn), and alternation in the boat-tail angle (Δb).

An extensive numerical analysis on the six design parameters is performed. Figure 2.11 provides a comprehensive summary of the percentage differences in peak values of C_l and C_m, alongside the stall angles of attack (AoAs), for all design parameter values compared to the baseline cases. The error bars in the figure denote the maximum and minimum percentage differences observed. In Fig 2.11(a) and (b), it is evident that the f_m scaling factor exhibits the most significant mean percentage differences, with 8.4% for the lift coefficient and 8.6% for the moment coefficient. This factor also shows the widest range of fluctuation between the maximum and minimum values. There is a notable consistency in the trends of percentage differences for both C_l and C_m, with the exception of Δb. Specifically, a change in Δb is able to significantly alter the pitching moment while maintaining a relatively stable lift coefficient. This observation suggests that further investigation into the boat-tail angle (Δb) as a design parameter could be instrumental in mitigating the effects of dynamic stall. The results also indicate that the moment coefficient also remains relatively constant across all scaling factors of fk, ft, and x_1. Additionally, Fig 2.11(c) and (d) reveal that both the lift and moment stall AoAs demonstrate the largest mean percentage differences for the f_m and f_t factors, and substantial percentage fluctuation for f_k. However, across the entire range of the Δb and Δn factors, the lift and moment stall AoAs are relatively unvarying, with a mean percentage difference below 0.8% for the entire scaling factor range. It is important to note that these findings are based on simulations using a baseline NACA 0012 airfoil. It is crucial to recognize that the influence of design parameters may vary with different baseline airfoils. To gain a more comprehensive understanding, an extensive statistical and sensitivity analysis is conducted using Morris' method later.

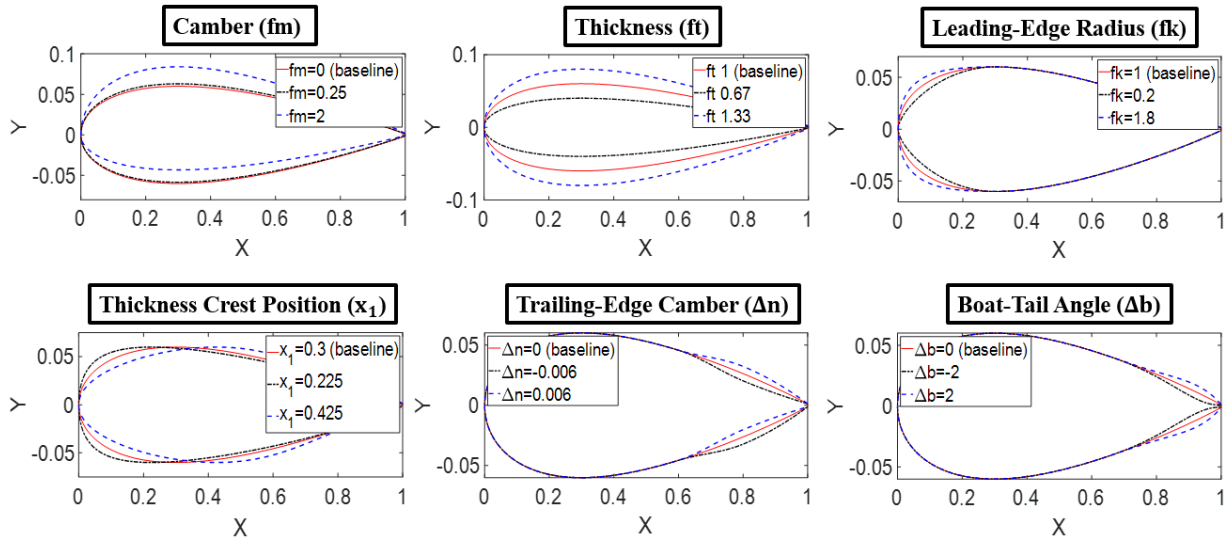

FIGURE 2.10. Diagram of the airfoil geometries for the design parameter ranges.

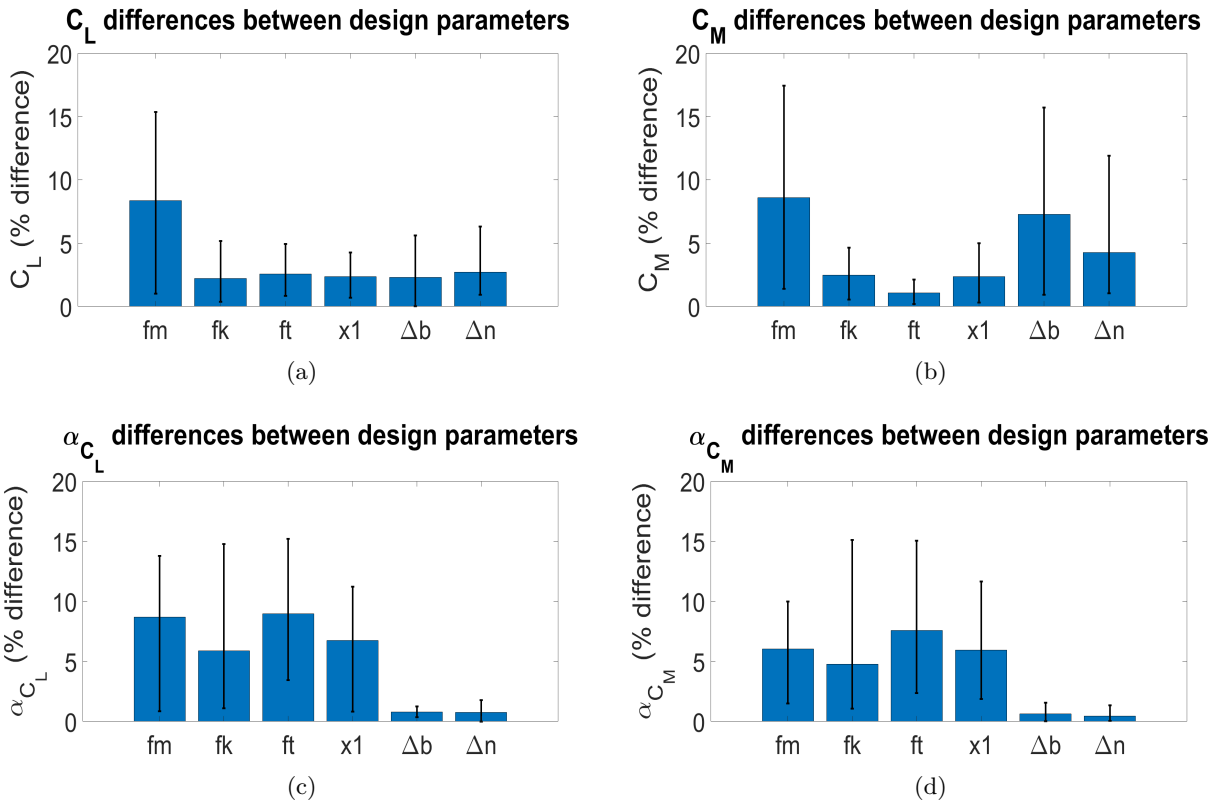

FIGURE 2.11. Comparison of the percentage differences between (a) C_l peaks, (b) C_m peaks, (c) lift stall AoAs, and (d) moment stall AoAs with the baseline cases.

2.3.10. Further Investigation of the Boat-Tail Angle. Figure 2.12(a) presents the airfoil geometry as it undergoes further variations in the boat-tail angle (Δb). In this further study, the effect of the change in the boat-tail angle up to a scaling factor of Δb=4 is investigated. With this additional increase in Δb, the airfoil trailing edge continues to expand outwards, and concurrently, the total area of the airfoil increases. Figure 2.12(b) and (c) reveal that the peak magnitudes of both the lift and moment coefficients exhibit a declining trend with an increasing boat-tail angle. The decrease in the magnitude of the moment coefficient is considerably more pronounced than that of the lift coefficient. Specifically, over the range of Δb from 0 to 4, the lift coefficient experiences a modest reduction of 4.7%, whereas the moment coefficient has a more substantial reduction of 20.3%. The stall AoAs remain largely unaffected during this range. The results suggest that the incorporation of the boat-tail angle design parameter is considered to be advantageous in mitigating the pitching moment. This means the dynamic stall effect can be attenuated with just a relatively minor sacrifice in lift. The outcome further underscores the potential utility of manipulating the boat-tail angle as a means of optimizing airfoil performance characteristics. Furthermore, this highlights the significance of trailing-edge morphing in the context of controlling the dynamic stall phenomena without incurring significant losses in lift.

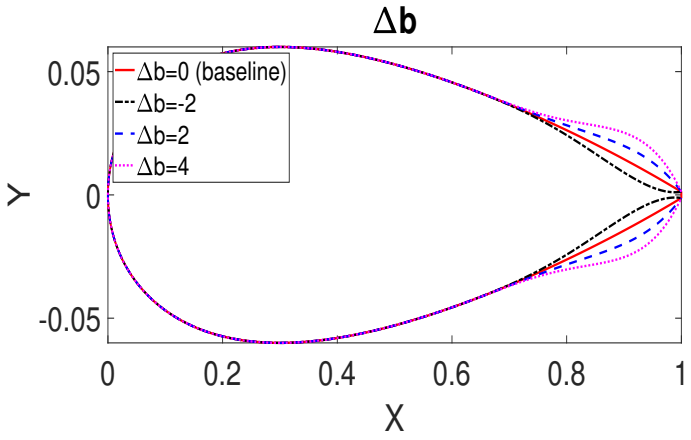

(a)

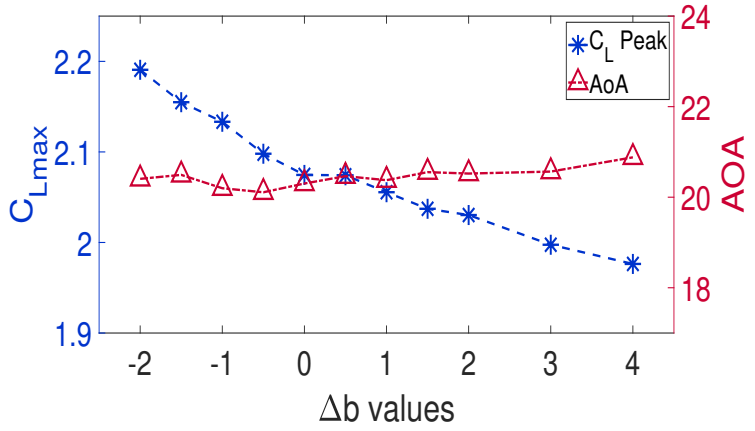

(b)

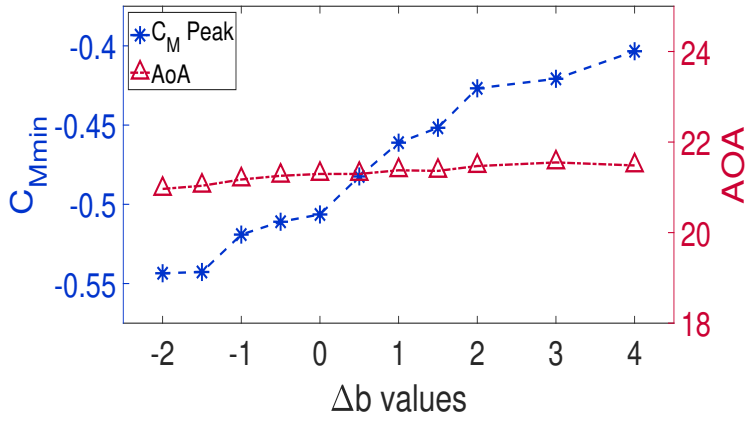

(c)

FIGURE 2.12. Effect of the boat-tail angle design parameter: (a) airfoil geometry, (b) lift peak values, and (c) pitching moment peak values.

2.4. Sensitivity Analysis

2.4.1. Morris' Method. A sensitivity analysis can be used to study the impact of the variability in the inputs of the model on the outputs. The numerical comparison of the main global sensitivity analysis methods has been performed in industrial benchmark cases. For the design of aerospace vehicles that involve computationally expensive models and a large number of input factors, screening methods can identify the factors that have the strongest effects on the output variability. The one-at-a-time (OAT) analysis is performed by varying one of the inputs in an interval while the other input factors are fixed to the baseline value. This method follows a complete factorial design method. The number of simulations increases with the power law based on the number of input parameters. Therefore, this design of experiment is extremely time consuming and unfeasible for most practical cases. Furthermore, this approach is not capable of taking into account the effects induced by interactions between dependent parameters [10, 44].

Morris [71] developed a powerful method that is based on a repetition of a set of randomized OAT design experiments. This method makes it possible to overcome the limiting assumptions of the OAT method. For a computational model that consists of r input parameters, Morris' method is composed of n repeating times of randomized one-factor-at-a-time designs in the selected range of input variables, which leads to a number of $n(r+1)$ simulations. The method starts with start values (baseline case) within the defined ranges of possible values for all input parameters. The second step changes the values for one parameter (all other inputs remaining at their start values). Next, the value for another parameter is changed (the previous variable is kept at its changed value and all other ones kept at their start values). This goes on until all input variables are changed. As mentioned previously, the change order and change values of inputs in the entire experimental design should be randomly selected. In a computational model that consists of r input parameters, each repetition i $(i = 1, ..., n)$ allows to evaluate an elementary effect $E_j^{(i)}$ (between two successive calculations) by the input parameters X_j $(j = 1, 2, ..., r)$ [71, 81]. In this case, the elementary effects include the difference of the peak values for the coefficient of lift and moment, and their corresponding angles of attack for the successive repetitions. The input parameters include all six of the airfoil design parameters in this study. Ultimately, when ranking the most important variable is of interest, Morris' method is proven to be the most robust for any differentiable function (linear or non linear) [10, 44].

The entire experimental design provides an n-sample of effects for each input, from which the following sensitivity indices are derived:

$$\mu = \frac{1}{n}\Sigma_{i=1}^{n} E_j^{(i)} \tag{2.16}$$

$$\mu^* = \frac{1}{n}\Sigma_{i=1}^{n} |E_j^{(i)}| \tag{2.17}$$

$$\sigma = \sqrt{(1/n-1)\Sigma_{i=1}^{n}(E_j^{(i)} - \mu)^2} \tag{2.18}$$

In the above equations, μ is the average of the values of the effects, μ^* is the average of the absolute values of the effects, and σ is the standard deviation of the effects. All three of these values are evaluated for the jth input parameter. The sensitivity of the input parameters are represented in Eqs. (2.17) and (2.18). The μ^* indicates the importance of the jth parameter on the output. The σ indicates the linearity of the model or interactions with other parameters. Therefore, a low μ^* and low σ represent the inputs with negligible effects; a high μ^* and low σ represent the inputs with linear effects and no interactions with other parameters; a high σ represents the inputs with nonlinear effects and/or interactions with other parameters.

2.4.2. Case Study. The parameter study presented in Section 2.3 gave the effect of each parameter on the dynamic stall characteristics. In this case study, Morris' method is employed to quantitatively evaluate, identify, and rank the importance of each parameter in terms of the dynamic stall characteristics (i.e. the peak values for the coefficients of lift and moment, and their corresponding angles of attack). As mentioned in the previous subsection, the change in the order and the change in the values of the inputs in the entire experimental design should be selected randomly. In this study, the change in the order is generated through a random sort and the change in the values are obtained using a Latin hypercube sampling method.

There are six different parameters that are used for the study in this chapter. In this case study, the repeating time n is chosen to be equal to 6. In all of these repetitions, the simulation

starts from a random order and value of baseline design parameters that are given in Table 2.1. Next, Table 2.2 shows the change in the order and values of the design parameters used for the sensitivity analysis in the case study. In each repetition, the change of the order and the change of the values of the design parameters are different. All of the cases used for the sensitivity analysis are conducted using the setup conditions outlined in Sec. 3.3.1.

Figure 2.13 shows the statistical outcomes of Morris' method for the coefficient of lift and the location of the lift stall AoAs across six design parameters. In Fig 2.13(a), in most cases, the change in the average of the values of the effects is less than 0.05 for the coefficient of lift and less than 1 for the location of the lift stall AoA. It is shown that x_1 has the most significant impact on the change in the average value of the effects. This design parameter exhibits an increase of 0.00601 for the coefficient of lift and an increase of 1.162 for the lift stall AoA. Figure 2.13(b) shows the average of the absolute values of the effects μ^* for the coefficient of lift and the location of the lift stall AoA. The f_t has the smallest change in the average of the absolute value for the coefficient of lift. All the other design parameters have a change in the average of the absolute value at 0.05 or greater for the coefficient of lift. For the location of the lift stall AoA, the Δb, Δn, and f_m have the smaller change in the average of the absolute value while f_t and x_1 have the larger change in the average of the absolute value. Again, the x_1 has the most significant impact on the change in the average of the absolute values of the effects. The standard deviation of the effects (σ) provides the information on how dispersed the data is in relation to the mean value given by μ, which is shown in Fig 2.13(c). Similar to the results of of μ^*, the value of σ for different parameters have a similar variation trend. For the coefficient of lift, the most influential parameters are f_k and x_1 while the least influential parameters are the f_t and Δb. For the location of the lift stall AoA, the most influential parameters are the f_t and x_1 while the least influential parameters are Δb and Δn. To sum up, the x_1 and f_k have large values of μ^* and σ in the lift coefficient, which indicates that these two parameters are not only important parameters but also have either a nonlinear behavior or interactions with other parameters. Morris' method does not make a distinction between the two. Similarly, the f_t and x_1 design parameters have large values of μ^* and σ in the lift stall AoA.

Figure 2.14 shows the statistical outcomes of Morris' method for the coefficient of moment and the location of the moment stall AoAs across six design parameters. Figure 2.14(a) reveals that Δb, x_1, f_k, and Δn have substantial μ magnitudes of 0.0122, 0.0118, 0.00905, and 0.00858, respectively,

for the coefficient of moment. The f_t has a modest μ magnitude of 0.00325, and f_m has a very small μ magnitude of just 0.000433 for the coefficient of moment. Furthermore, f_t and x_1 manifest a more pronounced μ for the moment stall AoA with magnitudes of 1.06° and 1.17°, respectively. The Δb, f_k, f_m, and Δn all have a very small μ magnitude (below 0.122) for the moment stall AoA. In Fig. 2.14(b), x_1 and Δn have the greatest μ^* magnitudes of 0.0321 and 0.0270, respectively, for the coefficient of moment. The f_t has the lowest μ^*, which is still a considerable magnitude of 0.0096. Moreover, f_t and x_1 have the greatest μ^* magnitudes of 1.57° and 1.31°, respectively, for the moment stall AoA. This is followed by f_k and f_m with μ^* magnitudes of 0.7188° and 0.610°, respectively. Likewise, Δb and Δn exhibit a very minor μ^* for the moment stall AoA. In Fig 2.14(c), the σ results summarize the main findings. It is important to note that the design parameters characterized by high σ values demonstrate nonlinear effects and/or interactions with other parameters. The moment coefficient's influential design parameters are ranked in ascending order as follows: f_t, f_m, Δb, f_k, x_1, and Δn. For the location of the moment stall AoA, the ascending order ranking is as follows: Δn, Δb, f_m, f_k, x_1, and f_t. In conclusion, it is essential to recognize that the thickness crest position (x_1) has the greatest overall influence for the moment coefficient and the moment stall AoA. Also, the boat-tail angle (Δb) and trailing-edge camber (Δn) have negligible effects on the moment AoA due to very small μ^* and σ values. Overall, it is important to note that the thickness crest position is a dominant parameter in the lift and moment coefficients and their stall AoAs.

TABLE 2.1. The order and values of the baseline design parameters in each iteration used for sensitivity analysis.

n	Change order (changed value) - baseline					
1	t_0 (0.13276)	x_0 (0.31632)	$\triangle n$ (-0.0018912)	$\triangle b$ (-0.3664)	f_m (1.129)	f_k (0.83232)
2	f_m (0.7954)	t_0 (0.116032)	$\triangle b$ (-0.6004)	x_0 (0.36686)	f_k (0.68864)	$\triangle n$ (0.0043008)
3	t_0 (0.153808)	f_k (1.31968)	$\triangle n$ (0.00297)	$\triangle b$ (-0.0456)	f_m (0.6148)	x_0 (0.34702)
4	f_k (0.70384)	t_0 (0.090072)	f_m (1.2616)	$\triangle b$ (1.9644)	x_0 (0.3022)	$\triangle n$ (-0.0045)
5	$\triangle b$ (1.4284)	x_0 (0.40978)	t_0 (0.133576)	f_k (1.61008)	f_m (1.5936)	$\triangle n$ (0.0033828)
6	$\triangle n$ (-0.0014568)	x_0 (0.3981)	f_k (0.84912)	$\triangle b$ (1.8176)	t_0 (0.102968)	f_m (0.3166)

TABLE 2.2. The change in the order and value of design parameters used for sensitivity analysis.

n	Change order (changed value)					
1	t (0.098248)	x_1 (0.2878)	$\triangle n$ (0.0056664)	$\triangle b$ (-1.0872)	f_m (0.3048)	f_k (1.47888)
2	f_m (0.4274)	t (0.119808)	$\triangle b$ (-1.8932)	x_1 (0.2646)	f_k (0.43168)	$\triangle n$ (0.0008016)
3	t (0.0818)	f_k (1.03856)	$\triangle n$ (0.0012564)	$\triangle b$ (0.0928)	f_m (1.6462)	x_1 (0.29174)
4	f_k (1.25104)	t (0.102808)	f_m (0.1358)	$\triangle b$ (1.1156)	x_1 (0.3252)	$\triangle n$ (-0.0024804)
5	$\triangle b$ (0.3656)	x_1 (0.3784)	t (0.123024)	f_k (1.73232)	f_m (0.4814)	$\triangle n$ (-0.0046596)
6	$\triangle n$ (0.0004956)	x_1 (0.28844)	f_k (1.57008)	$\triangle b$ (-0.3524)	t (0.134224)	f_m (1.4534)

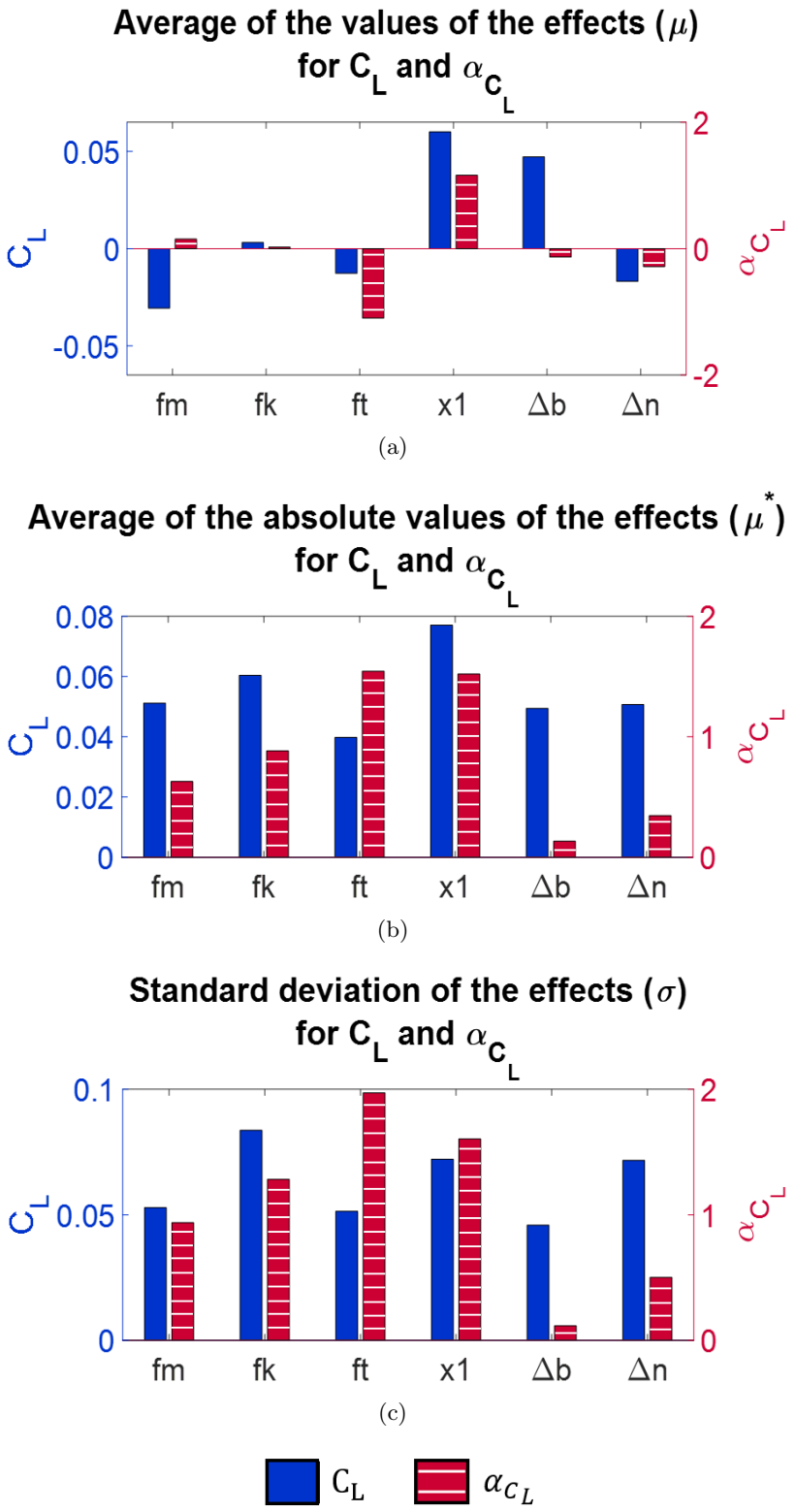

FIGURE 2.13. Morris' method results for lift.

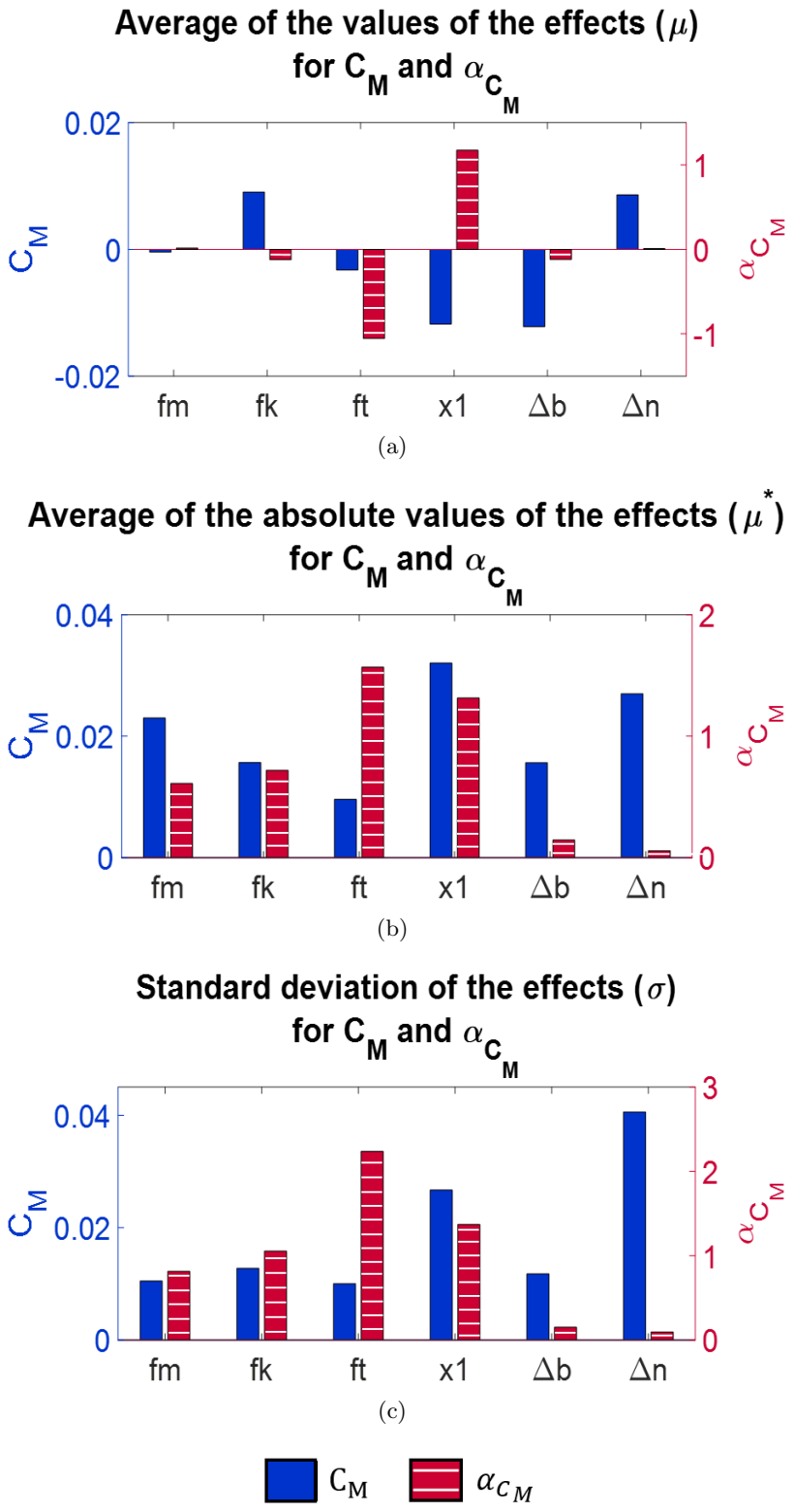

FIGURE 2.14. Morris' method results for pitching moment.

2.5. Summary

This chapter presented a comprehensive numerical analysis of parametric airfoil design, with a focus on exploring the influence of various design parameters on the dynamic stall characteristics under pitching motion. Initially, the validation of the reliability of the numerical simulations in predicting the lift, drag, and moment coefficients against experimental data for a NACA 0012 airfoil was performed. The findings indicated that the OVERFLOW RANS CFD is highly proficient in accurately predicting the dynamic stall characteristics.

Following the validation, an extensive analysis was undertaken for the six distinct design variables: camber, leading-edge radius, thickness, thickness crest position, trailing-edge camber, and boat-tail angle. A NACA 0012 airfoil was used as the baseline airfoil. The analysis revealed that the camber exerted the most significant effect on the peak values of both the lift and moment coefficients. The boat-tail angle exhibited a more pronounced effect on the peak values of the moment coefficient than on the lift coefficient. Furthermore, the camber and thickness were found to have the largest effect on the stall AoAs for both lift and moment. The boat-tail angle and trailing-edge camber demonstrated the smallest effect on these parameters. Most notably, a deeper investigation on the effect of the boat-tail angle has been performed. It was found that a positive alteration in the boat-tail angle scaling factor continues to greatly reduce the pitching moment, while concurrently sustaining a comparable lift coefficient.

In conjunction with the design parameter investigation, a sophisticated sensitivity analysis utilizing Morris' method was executed to systematically evaluate the quantitative impacts of these parameters on the dynamic stall characteristics. In this approach, the baseline airfoil was also changed for a more comprehensive study. The findings acknowledge that the thickness crest position is a critical parameter influencing both the lift and moment coefficients and their stall AoAs. Ultimately, this design parameter study and sensitivity analysis have identified and ranked the key design parameters in relation to their impact on dynamic stall.

CHAPTER 3

Effect of Trailing-Edge Morphing

3.1. Introduction

Dynamic stall depends on several factors. Semi-empirical methods based on classical theories have been developed to model dynamic stall and its flow behavior. These models illustrate the flow separation criteria related to the adverse pressure gradient, the magnitude of circulation determined by the Kutta condition, the leading edge and trailing edge separation of stall onset, responses of different wings, and the effects of gust penetration [64, 96]. Although these early models provide valuable insight for design and analysis, they do not offer a deeper understanding of the physical mechanisms involved in the dynamic stall formation process. McCroskey et al. [70] classified dynamic stall into four categories based on the nature of the boundary layer separation preceding the stall: 1) leading-edge stall, 2) trailing-edge stall, 3) thin airfoil stall, and 4) mixed stall. Shih et al. [84] divided the unsteady flow development past a constantly pitching airfoil into four stages: 1) a vortex formation stage, 2) a vortex convection stage, 3) the stall onset stage, and 4) the stalled stage. In their study, they observed that boundary-layer separation near the airfoil leading edge leads to the formation of a vortical structure, the evolution of which dominates the airfoil's aerodynamic performance. Geissler and Haselmeyer [27] have further investigated the dynamic stall onset, focusing on the unsteady pressure distribution, and development of leading-edge separation bubbles as well as trailing-edge separation areas. Visbal and Garmann [102] analyzed the unsteady boundary-layer behavior and DSV in detail using high-fidelity large eddy simulations (LES), confirming that the laminar separation bubble (LSB) plays a crucial role in the onset of dynamic stall. As the LSB bursts, there is a rapid increase in the reversed flow region near the leading edge. The LSB's breakdown triggers the dynamic stall, and it is instrumental in initiating the events leading to the DSV formation. Gupta and Ansell [33] performed a series of wind-tunnel experiments to understand the unsteady flow physics associated with dynamic stall, particularly analyzing the evolution of the airfoil boundary layer, leading-edge laminar separation bubble, and

DSV. Batther and Lee [4, 5] employed delayed detached eddy simulations (DDES) and obtained results similar to LES concerning the flow physics associated with dynamic stall onset, but with a considerably lower computational cost than LES. Trailing-edge flow separation, which migrates towards the leading edge as the AoA increases, plays a critical role in bursting the LSB and thus triggering a DSV at high Reynolds number flows [6] and high Mach number flows [7]. Sharma and Visbal [82] investigated the effect of airfoil thickness on dynamic stall onset using LES at a chord-based Reynolds number of 200,000. Their study concluded that the dynamic-stall onset mechanism changes with a gradual change in airfoil thickness. For instance, the DSV for a thin airfoil is initiated by the LSB bursting near the leading edge due to an adverse pressure gradient. However, for a thicker airfoil, the LSB bursting is initiated by the merging of the LSB and the flow separation that migrates from the trailing edge, even at low Reynolds number and low Mach number conditions. Tran et al. [98] found that dynamic stall has bifurcation characteristics during multiple cycles, and they proposed the clustered-averaged quantities to analyze dynamic stall events.

Numerous studies have explored modifying the leading edge of an airfoil to control dynamic stall since the aerodynamics of an airfoil are primarily determined by the flow conditions and the vortex effects at the leading edge. Barger [3] described several methods for designing lower-pitching airfoils by modifying various airfoil parameters, including the leading edge. Ericsson and Reding [26] conducted studies in which they altered different characteristics of the airfoil leading edge to investigate its effects on flow physics. They found that changes in the leading edge shape influenced pressure, flow movement, flow separation, and flow reattachment. It is expected that leading edge roundness could delay leading edge separation, consequently delaying the dynamic vortex. Furthermore, Gharali et al. [28] conducted numerical modeling of an oscillating S809 airfoil with erosion under dynamic stall at high reduced frequencies. The study aimed to examine the erosion, particularly leading edge erosion, on operating wind turbines, which is a common issue for in-service wind turbine blades. The eroded airfoil experienced a lift decrease, severely impacting wind turbine performance. Efforts have been made to understand the impact of leading edge geometry.

Although leading-edge morphing has provided favorable results for the mitigation of dynamic stall, the leading edge of an airfoil is susceptible to the effects of harsh environments, and modifying

the leading edge may not always be the most reliable design practice. Surface roughness, dust, rain, sand, ice, and other inclement weather conditions can impose penalties on aerodynamic efficiency and performance, and compromise the capability of leading-edge morphing to control the DSV. The effects of harsh environments should be thoroughly evaluated, analyzed, and considered in the design process before reaching a definitive conclusion. In contrast, the airfoil's trailing edge is less sensitive to environmental changes. There has been limited research on the effects of trailing-edge morphing on dynamic stall. More recently, Wu et al. [105] explored suppressing the pitching oscillation of a NACA 0012 airfoil at a Reynolds number of 1.35×10^5 by employing phase-shifted trailing-edge morphing. Their results suggested that the trailing-edge motion reduces energy extraction and could effectively suppress stall-flutter limit-cycle oscillation amplitude within specific ranges of amplitude and frequency. In the previous chapter, I examined the impact of airfoil design parameters on dynamic stall using Reynolds Averaged Navier-Stokes (RANS) computational fluid dynamics (CFD). One of the findings demonstrated that a positive trailing-edge boat-tail angle leads to a reduction in the pitching moment amplitude by about 10% while the reduction in the lift is only limited by 2% [85, 87].

As discussed in the previous paragraph, trailing-edge morphing could provide a favorable effect on dynamic stall mitigation. However, there is still a limited understanding of how trailing-edge morphing affects the local flow regimes and the global DSV onset phenomena. As mentioned earlier, the trailing-edge stall initiates with flow reversal near the trailing edge, and this reverse flow region gradually expands and migrates upstream to the leading edge, and eventually meets the LSB as the AoA increases. Therefore, modifying the trailing edge could change the local flow characteristics of the trailing-edge separation vortex and potentially help delay the bursting of the LSB. This approach might offer an alternative way to mitigate the effects of dynamic stall under specific conditions. The objectives of this chapter are to evaluate the effectiveness of trailing-edge morphing with a simple and fixed geometry change in mitigating dynamic stall and to investigate the detailed flow physics of dynamic stall with trailing-edge morphing using DDES.

3.2. Methodology

This section provides an overview of the methodology and solution approach employed in this chapter. In the subsequent subsections, the details of the Delayed Detached Eddy Simulation

(DDES) equations, trailing-edge morphing method, mesh generation, and boundary conditions and numerical schemes are presented.

3.2.1. Delayed Detached Eddy Simulation (DDES) Equations. The simulations in this chapter use the Delayed Detached Eddy Simulation (DDES) numerical method to model flow. The DDES model is already available in the OVERFLOW [72] CFD code. When the Detached Eddy Simulation (DES) approach is implemented, the whole or at least major part of the attached boundary is treated by RANS, while LES is applied only in the separated flow region. In this hybridization, the RANS and LES approaches are coupled through a hybrid turbulent length-scale based on the blending of the RANS and LES length scales:

$$\tilde{l} = f_{hyb}(1 + f_{restore}\Psi)l_{RANS} + (1 - f_{hyb})C_{DES}\Psi\Delta \tag{3.1}$$

where Δ is the subgrid length-scale and C_{DES} is the empirical constant of the LES branch of DES. In the concept of DES, in order to create the hybrid model, the hybrid length scale $\tilde{l}$ defined in Eq. 3.1 will be substituted into the background RANS model in place of the RANS length scale, l_{RANS}. For example, for the Spalart Allmaras (SA) model, the length scale is equal to the distance to the wall, $l_{RANS} = d_w$ while for the $k - \omega$ SST model of Menter, $l_{RANS} = k^{1/2}/(C_\mu\omega)$.

The hybrid function f_{hyb} includes DDES and Wall-Modelled Large Eddy Simulation (WMLES) branches.

$$f_{hyb} = max(1 - f_d), f_{step} \tag{3.2}$$

Here, f_d is the delay function of DDES, which is given as follows:

$$f_d = 1 - tanh[(8r_d)^3], r_d = \frac{1}{(\kappa^2 d_w^2)} \frac{\nu_t}{max[(\partial u_i/\partial x_j)(\partial u_i/\partial x_j)]^{1/2}, 10^{-10}} \tag{3.3}$$

where κ is the Karman constant. Furthermore, the function f_{step} is active only when the model operates in WMLES mode with the purpose of providing a rapid switch from RANS to LES deep inside the boundary layer. Another function used in the hybrid length scale definition is the low-Reynolds number correction Ψ from the DDES model. This function Ψ depends on the background

RANS model and also provides the amplification effect of $f_{restore}$. The complete and explicit details of the derivation of the DDES equations can be found in Refs. [90, 92, 99].

3.2.2. Trailing-Edge Morphing. To modify the trailing edge, a parametric airfoil design tool, PARFOIL is used. This tool was originally developed by Lim [59] and later modified by Liu and Lee [62, 63] when they applied PARFOIL to airfoil trailing-edge noise problems. This tool was initially developed for rotor airfoil design. The airfoil geometry is parameterized using several design parameters to control or morph the airfoil coordinates. One of the modifiable parameters in PARFOIL is the trailing edge boat-tail angle, which is an interior angle between the upper and lower surfaces near the trailing edge. In contrast to other parameterization methods, PARFOIL begins with a baseline airfoil geometry and then morphs it into the desired airfoil geometry by adjusting a design parameter. This innovative method benefits from the shape of the selected airfoil geometry, and each design parameter also has a physical meaning. During the process, the grid points in the airfoil coordinates are redistributed using Non-Uniform Rational Basis Spline (NURBS) interpolation [74].

As depicted in Fig. 3.1, a parameterization is performed for the trailing-edge region, extending from a predefined point to the trailing edge. In the parametric model, the thickness (t_b) of the trailing-edge region is modified as follows:

$$t_b(y) = t(y) + \Delta t_b \tag{3.4}$$

$$\Delta t_b = \Delta b \cdot \frac{(y - y_R)^4}{(y_B - y_R)^4} \frac{(y-1)}{(y_B - 1)} \tag{3.5}$$

where y_R is the reference position representing a boundary point of the trailing-edge region, and y_R is set to 0.60c. The y_B is the horizontal position where the boat-tail angle is measured, and y_B is set to 0.80c in this study. As the boat-tail angle scaling factor (Δb) increases, the trailing edge of the airfoil becomes wider and the overall area of the airfoil expands. This effectively represents the de-cambering of the trailing-edge section. Only positive values of Δb are selected since the earlier work by Shum and Lee [85, 87] demonstrated the positive values of Δb provide favorable effects in dynamic stall. In Fig. 3.1, $\Delta b = -3$, $\Delta b = 3$, and $\Delta b = 4$ are examples of the morphed trailing-edge

airfoil. In the results section, these design parameter values will be used, and the effect of these parameter values on dynamic stall will be investigated.

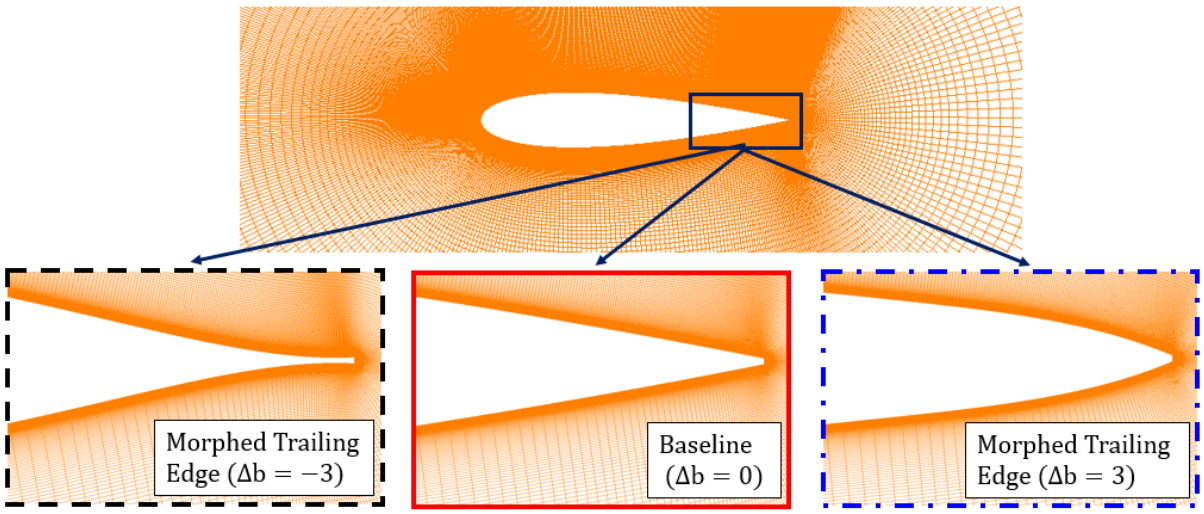

(a)

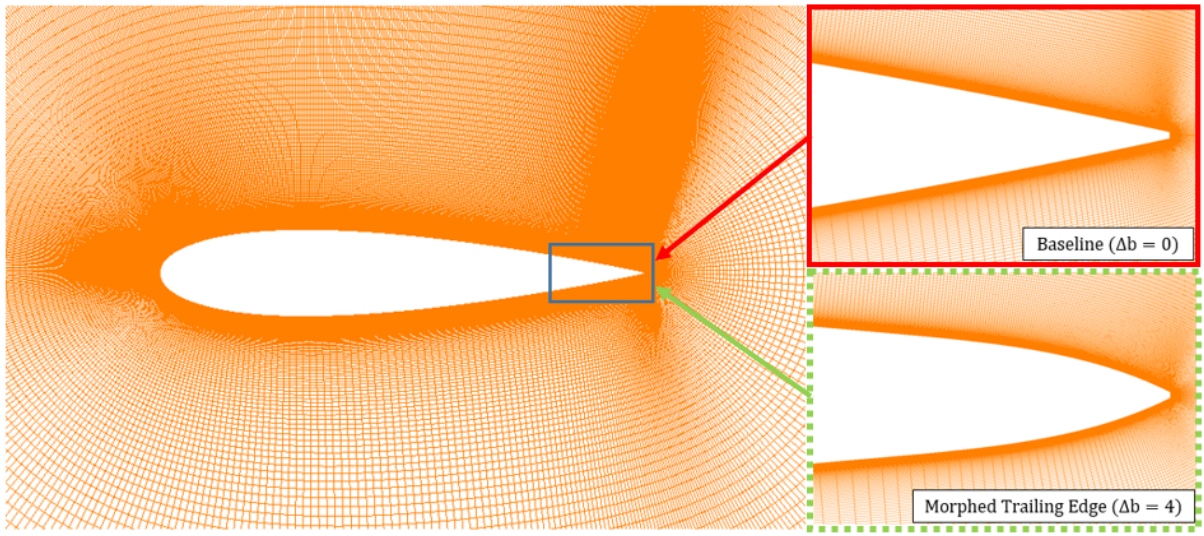

(b)

FIGURE 3.1. OVERGRID meshes showing examples of the trailing-edge morphing: baseline airfoil and morphed airfoil geometries near the trailing edge.

3.2.3. Mesh Generation. NASA's mesh software, OVERGRID [18], is employed to construct the mesh, which is compatible with Chimera grid tools [19]. The 3-D airfoil geometry mesh is depicted in Fig. 3.2. An O-type grid with a blunt trailing edge is used. The airfoil surface contains 800 grid points in the chordwise direction, with 600 points allocated on the upper surface and

200 points on the lower surface. The far-field boundary is positioned 100 chord lengths away from the airfoil surface. There are 200 points employed in the normal direction, with the majority (150 points) concentrated within the first chord length and the remaining 50 points distributed across the subsequent ninety-nine chord lengths. This distribution promotes significant grid stretching, aiding in the effective dissipation of flow variables at the far-field boundary. Despite the rapid grid stretching, the stretching ratio is maintained below 1.3, in line with OVERGRID best practices [18, 86]. The grid resolution is 0.02% of the chord length at both the leading and trailing edges. The chosen grid resolutions ensure adequate resolution for capturing flow physics and are based on best practices from previous studies [4,5,37,58,85,86,87]. The spanwise extent measures 10% of the chord length. Visbal and Garmann [102] investigated the impact of spanwise extents ranging from 10% to 160% of the chord length during the dynamic stall process for the airfoil section. They found that 10% extent is sufficient to capture the detailed flow features associated with the onset of the DSV. Furthermore, they suggested that grid stretching toward the far-field boundary enhances the accuracy of the results. The first wall-normal grid height is determined from a y^+ of approximately 0.488. This y^+ calculation is achieved through an iterative process of adjusting flat plate approximations and cross-referencing with solution data from the test cases.

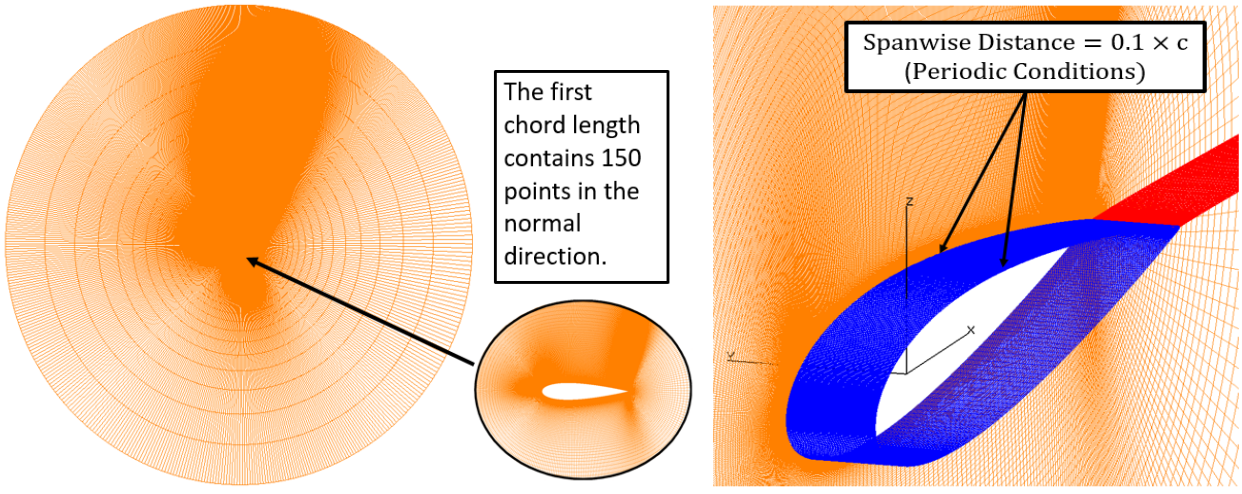

FIGURE 3.2. 3-D overview of the airfoil section mesh (NACA 0018): (a) O-type mesh and (b) mesh near the airfoil surface and boundary conditions.

3.2.4. Boundary Conditions and Numerical Scheme. The following boundary conditions are prescribed and imposed: no-slip adiabatic condition on the airfoil surface, spanwise periodic conditions, and periodicity in the chordwise direction at the trailing edge. The last boundary condition means that the solution remains the same across the line originating from the midpoint of the trailing edge and extending towards the far field. These listed boundary conditions are visually shown in Fig. 3.2. The spanwise periodic conditions are enforced to maintain a nominal 2-D configuration. This approach eliminates finite 3-D effects such as the influence of tip vortices, while still including spanwise flow and turbulence features and effects.

The OVERFLOW CFD solver was based on delayed detached eddy simulations (DDES). Prior to initiating the pitch-up motion, a well-resolved static solution is employed. The ramp-up motion pitch rate Eq. (3.6), described in Section 3.3.1, corresponds to a temporal resolution of 35,000 time steps. Additionally, 30 sub-iterations are used for numerical convergence in this study. These setup variables and temporal resolutions have demonstrated promising results in previous studies [58,86]. A small non-dimensional time step, $\Delta t^* = 0.000271$, is adopted in this study. Batther and Lee [4,5] have indicated that this small time step ensures numerical accuracy and provides sufficient temporal resolution for capturing complex flow features in dynamic stall. According to Rumsey [77], fully turbulent flow computations have produced inconsistent and undesirable results due to the absence of transitional modeling. Consequently, Rumsey argued that incorporating transitional modeling is necessary, as turbulent models do not activate until some distance from the stagnation point. Jain et al. [37] also demonstrated that the transitional turbulence model yields more accurate predictions of dynamic stall. In this study, the Coder SA-AFT (Amplification Factor Transport) transition model [22] was selected. The AFT model predicts the development of the instability envelope amplification factor by solving an advection-diffusion equation. This model is fully localized and Galilean invariant, which are essential features for compatibility with general CFD applications.

3.3. Numerical Results and Discussion

This section first shows the details and setup for the airfoil geometry and baseline test case. The analysis of the aerodynamic loading for the baseline case and morphed airfoil cases are presented. Then the dynamic stall stages and general flow physics are discussed. This includes the spanwise-averaged coefficient of pressure (C_p) and coefficient of skin friction (C_f), and contours of

the vorticity magnitude, normalized eddy viscosity, and normalized velocity during different stages in the dynamic stall process. This section also further investigates and compares one of the counter values for the trailing-edge morphing design parameter.

3.3.1. Airfoil Geometry and Test Case. A NACA 0018 airfoil is used for the baseline airfoil, which undergoes a pitching motion at a freestream Mach number of 0.1 and a Reynolds number of 200,000. This airfoil has a 1m chord length and a blunt trailing edge. The ramp-up motion, represented by the pitch rate, $\dot{\alpha}$, is provided in Eq. (3.6):

$$\dot{\alpha}(t^*) = \psi_o^+(1 - e^{-4.6t^*/t_o}) \tag{3.6}$$

where $t^* = tU_\infty/c$ denotes the non-dimensional time, t_o=0.5, and ψ_o^+ is 0.05. This allows the pitch rate to reach 99% of its asymptotic value, ψ_o^*, fairly quickly ($t_o = 0.5$). Figure 4.2 shows the angle of attack and non-dimensional pitch rate as a function of the non-dimensional time.

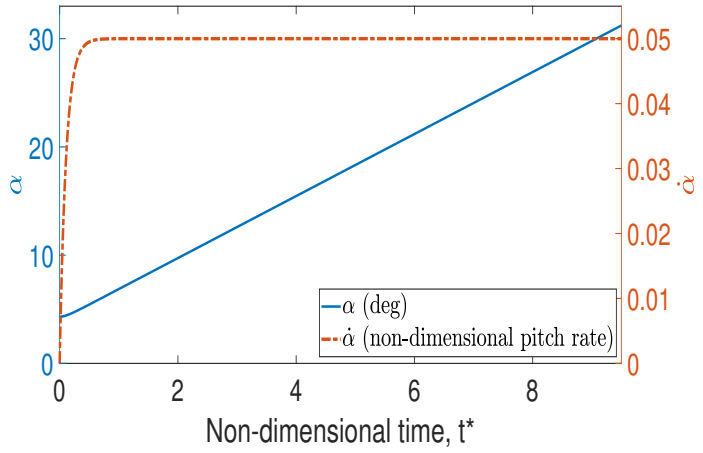

(a)

FIGURE 3.3. Prescribed ramp-up pitching motion for the NACA0018 airfoil

3.3.2. Analysis of the Aerodynamic Loading. Figure 3.4 shows a comparison of the results for the coefficient of lift (C_l), coefficient of drag (C_d), and coefficient of moment (C_m) for the baseline NACA 0018 airfoil case and the trailing-edge morphed cases (with Δb being equal to 3 and 4). As the boat-tail angle scaling factor increases, the magnitudes of C_l, C_d, and C_m all decrease, and the corresponding stall AoA decreases for the $\Delta b = 4$ case. The $\Delta b = 3$ case shows a

slight delay in the drop of C_m compared to the baseline case around 24°. However, it has a steeper slope beyond 25° and reaches a similar AoA where the minimum of C_m occurs. Both morphed cases exhibit more fluctuations of the aerodynamic loading compared to the baseline case before the drop of C_m. In both morphed cases, the C_m magnitude decreases more significantly compared to C_l. Overall, C_l is reduced by 0.7% and C_m by 7.8% between the baseline case (Δb=0) and the Δb=3 case. C_l is reduced by 2.7% and C_m by 8.3% between the baseline case (Δb=0) and the Δb=4 case. Furthermore, the reduction trend of C_l and C_m is not linear as the boat-tail angle scaling factor increases. In summary, trailing-edge morphing influences the aerodynamic loading and reduces the magnitude of C_m, though the effect is relatively smaller compared to typical leading-edge morphing [3, 45, 85, 87].

The remainder of the results section in this chapter will provide a detailed examination of the flow physics about how the trailing-edge morphing affects the onset of the DSV.

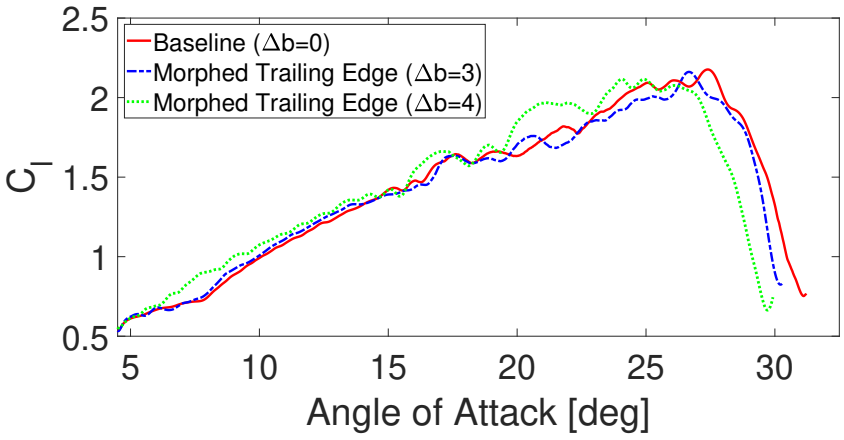

(a)

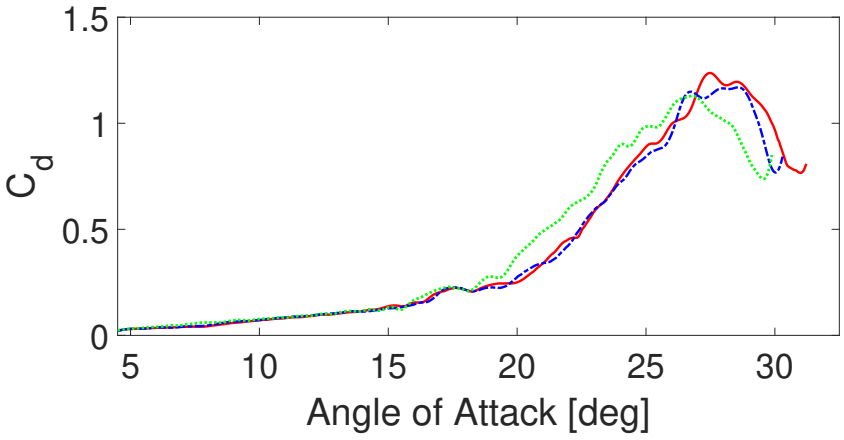

(b)

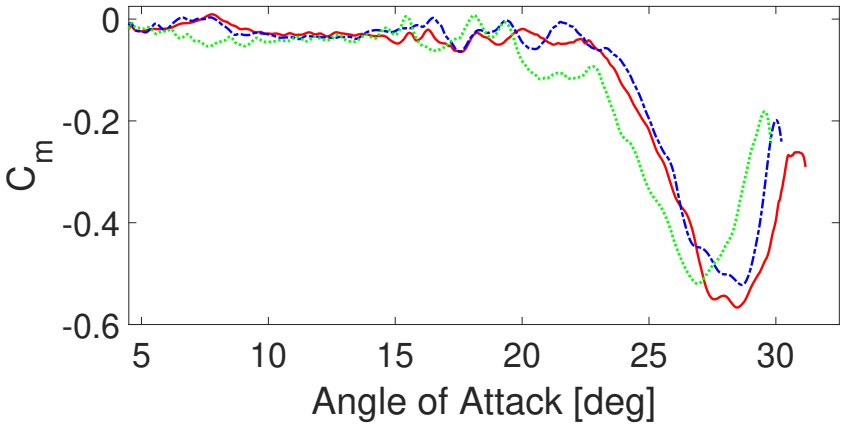

(c)

FIGURE 3.4. Comparison of the aerodynamic loading for the baseline ($\Delta b = 0$), $\Delta b = 3$, and $\Delta b = 4$ cases: (a) C_l, (b) C_d, and (c) C_m.

3.3.3. Dynamic Stall Stages and Development. The dynamic stall process can be characterized by various stages, which signify crucial events in its development, including initial and secondary shear layer separation, loss of suction at the leading edge, bursting of the LSB, and formation and propagation of the DSV [14, 84, 102]. It is essential to note that many parameters of interest in this subsection and the following subsection for the results are spanwise averaged and/or low-pass filtered due to the highly transient nature of dynamic stall behavior. This transient nature is particularly more pronounced at higher AoAs. Although analyzing a single plane may be sufficient for attached flow, Batther and Lee [4, 5] demonstrated that averaging is more suitable for representing the aggregated patterns and trends of highly fluctuating flows. Figures 3.5 and 3.6 present the spanwise-averaged surface pressure and skin friction coefficients for the baseline NACA 0018 airfoil case and the trailing-edge morphed cases (with Δb being equal to 3 and 4), from an initial stage ($\alpha = 13.7°$) where the LSB forms at the leading edge, to a stage ($\alpha = 25.4°$) where the DSV is fully formed and starts to propagate downstream and detach from the surface. For the baseline case, the suction collapses at $\alpha = 21.9°$ where the LSB size increases with a noticeable peak at around $x/c = 0.2$ as seen in Fig. 3.5(a). For the $\Delta b = 3$ trailing-edge morphed case, the suction collapse occurs at the same AoA ($\alpha = 21.9°$). However, a large peak at around $x/c = 0.2$ is not visible in Fig. 3.5(b). Furthermore, it is shown that, for the $\Delta b = 4$ morphed trailing-edge case, the suction collapse starts to occur at $\alpha = 20.3°$, which also shows an initial development of the DSV. This behavior is evidently shown in Figure 3.5(c), where the plateau starts to drop at $\alpha = 20.3°$, signaling that the LSB is already bursting. Interestingly, both the pressure and skin friction plots show that the gap in x/c distance between the peak magnitude C_p and C_f values for $\alpha = 23.8°$ and $\alpha = 24.2°$ is smaller for the $\Delta b = 3$ trailing-edge morphed case but larger for the $\Delta b = 4$ case compared to the baseline case. This indicates that, for the $\Delta b = 3$ trailing-edge morphed case, the initial development of the DSV is slower than in the baseline case. However, it eventually catches up with the speed of the baseline case, as demonstrated by the slope of C_m in Fig. 3.4. Conversely, the $\Delta b = 4$ trailing-edge morphed case exhibits a faster movement of the DSV in the downstream direction.

Figure 3.7 and 3.8 show the surface pressure and skin friction contours, illustrating the complete formation of the dynamic stall flow topology. These contour plots depict the development of the entire dynamic stall process on the airfoil surface across the full range of AoA. Moreover, these

pressure and skin friction contour plots provide further support for the spanwise-averaged C_p and C_f plots for the selected distinct angles shown in Figs. 3.5, and 3.6. The overall trends for the baseline and morphed airfoils are similar. At lower AoAs, the instability waves are visible in the C_f contours, indicating the flow transition. The transition location moves upstream toward the leading edge as AoA increases. It is seen that the trailing edge separation rapidly advances toward the leading edge, encountering the LSB near the leading edge at around $\alpha = 16.1°$. Following this encounter, the LSB eventually bursts at $\alpha = 21.9°$ for the baseline and $\Delta b = 3$ case, and at $\alpha = 20.3°$ for the $\Delta b = 4$ case. After the bursting of the LSB, the DSV forms and moves toward the trailing edge. It is important to note that the morphed airfoils exhibit different C_f contours at their midsection x/c locations compared to the baseline case, particularly around the event of the LSB bursting. The negative C_f value at the middle and aft sections near $\alpha = 21.9°$ indicates secondary shear layer separation in this region, which is not present for the baseline case. The behavior of the secondary shear layer (as shown in the higher x/c range values in Fig. 3.8) changes as the trailing edge boat-tail angle scaling factor (Δb) increases. The shear layer separation intensifies as the boat-tail angle scaling factor (Δb) increases.

Figure 3.9 shows the time histories of the instantaneous (C_p), spanwise-averaged ($< C_p >$), and the low-pass-filtered ($< C_p >_{lbf}$) surface pressures at the chordwise locations $x/c = 0.15$ and $x/c = 0.25$. The instantaneous data across the airfoil surface is sampled every 125 timesteps, corresponding to about every 0.1° of rotation. This data is first spanwise-averaged and then run through a low-pass filter to attenuate the high-frequency oscillations. It can be observed that the oscillations start to occur around $\alpha = 16°$ when the upstream migration of trailing-edge separation meets with LSB near the leading edge. This behavior occurs at a similar location for the baseline case and the morphed cases. The instantaneous pressure exhibits large oscillations between $\alpha = 16°$ and $\alpha = 21°$ when the LSB experiences instability before bursting. After the bursting of the LSB at $\alpha = 21.9°$ for the baseline and $\Delta b = 3$ and at $\alpha = 20.3°$ for $\Delta b = 4$ at $x/c = 0.15$, the instantaneous pressure shows a smoother variation. Overall, the morphed airfoils exhibit less fluctuations for the instantaneous pressure.

The overall aspects of dynamic stall behavior have been discussed, and the remainder of the results section will delve into the detailed flow physics described in these various stages.

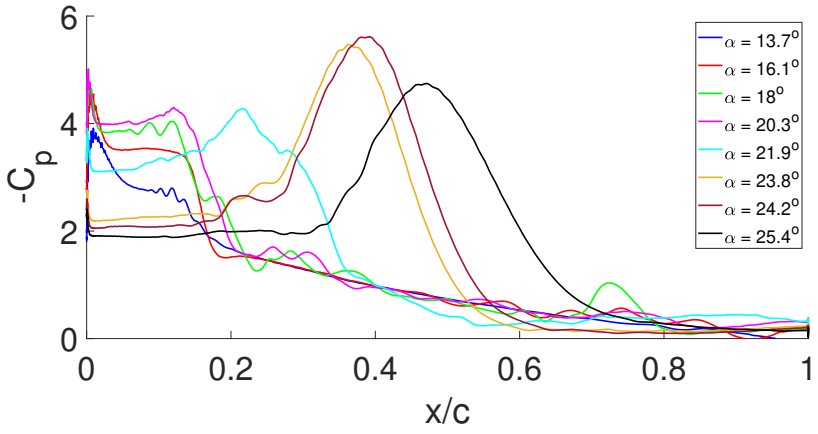

(a)

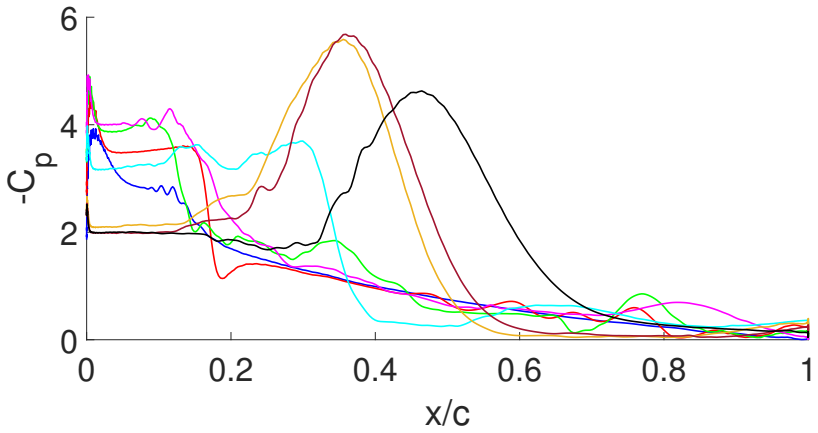

(b)

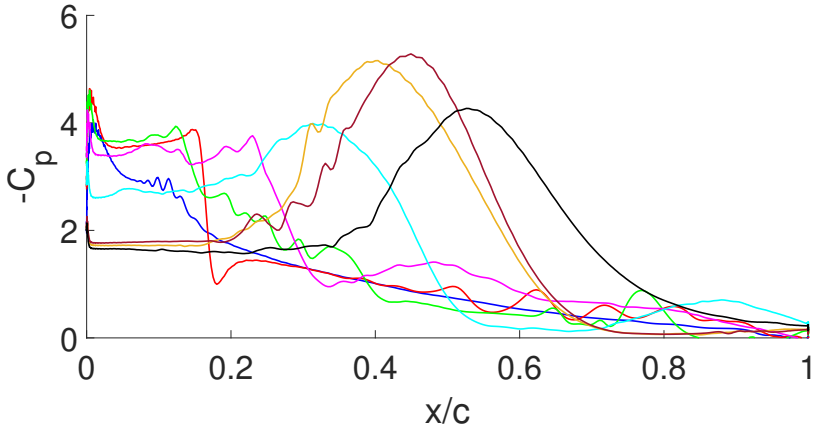

(c)

FIGURE 3.5. Spanwise-averaged C_p for the: (a) baseline ($\Delta b = 0$), (b) $\Delta b = 3$, and (c) $\Delta b = 4$ during different stages in the dynamic stall process.

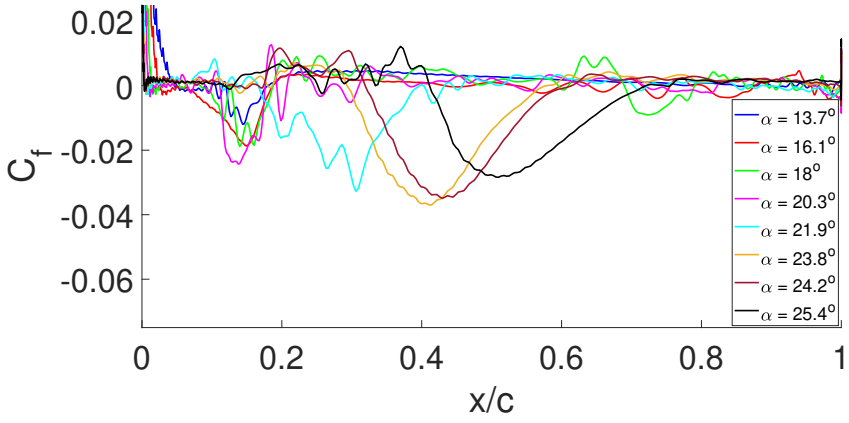

(a)

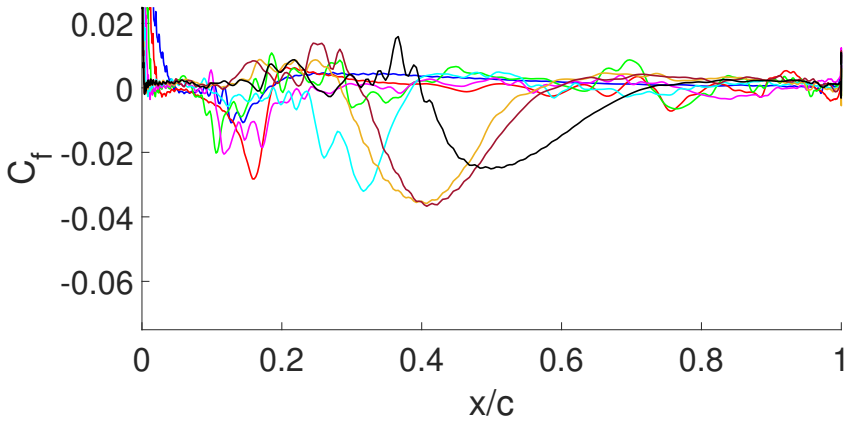

(b)

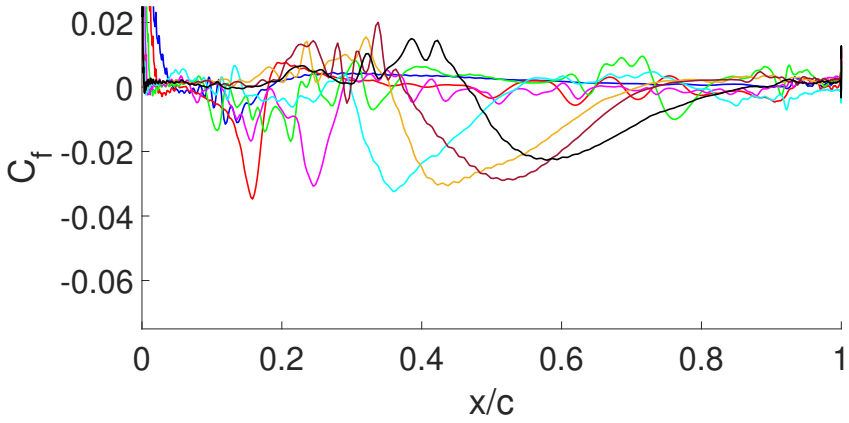

(c)

FIGURE 3.6. Spanwise-averaged C_f for the: (a) baseline ($\Delta b = 0$), (b) $\Delta b = 3$, and (c) $\Delta b = 4$ during different stages in the dynamic stall process.

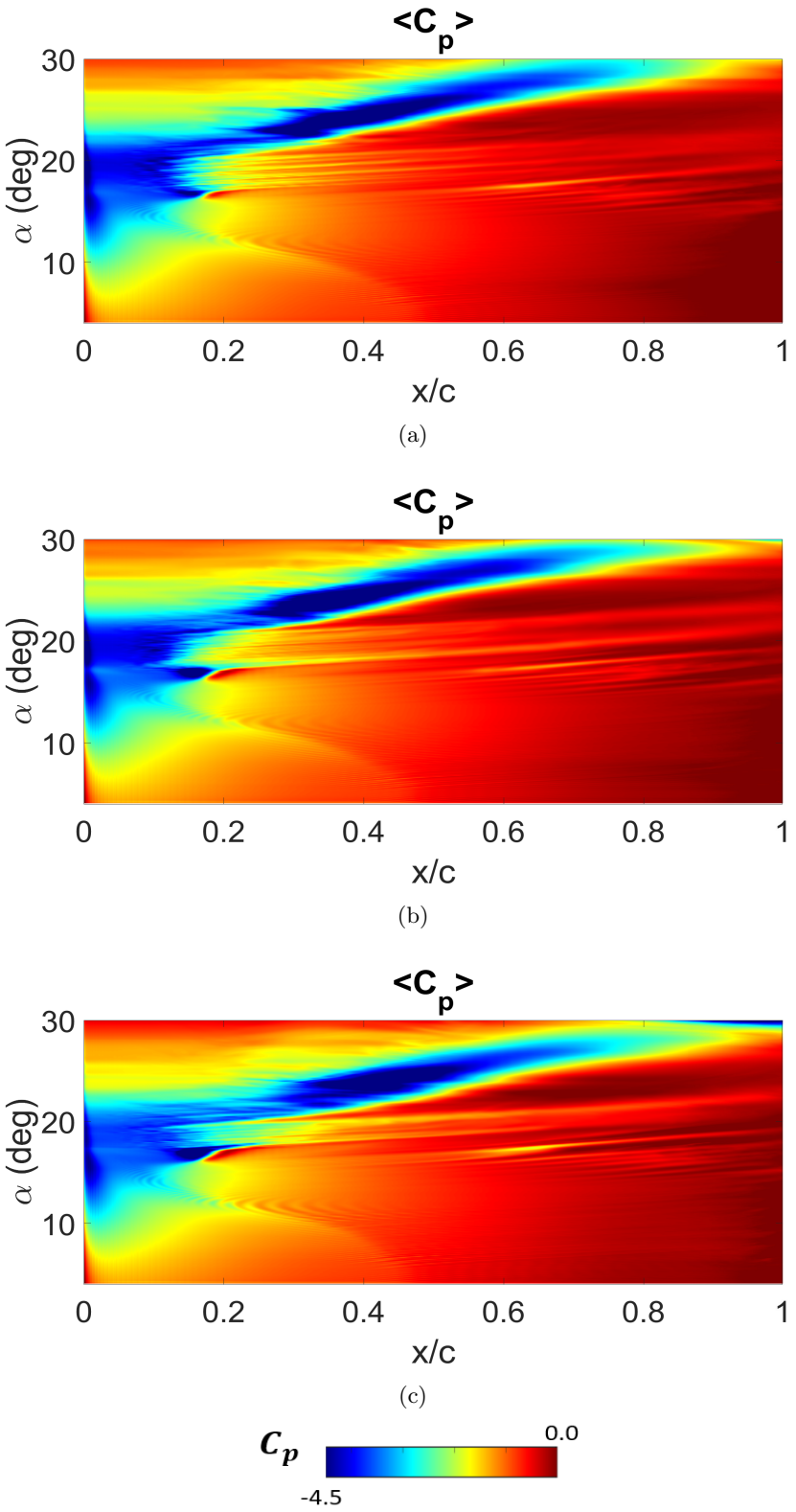

FIGURE 3.7. Spanwise-averaged C_p contours: (a) baseline ($\Delta b = 0$), (b) $\Delta b = 3$, and (c) $\Delta b = 4$ during different stages in the dynamic stall process.

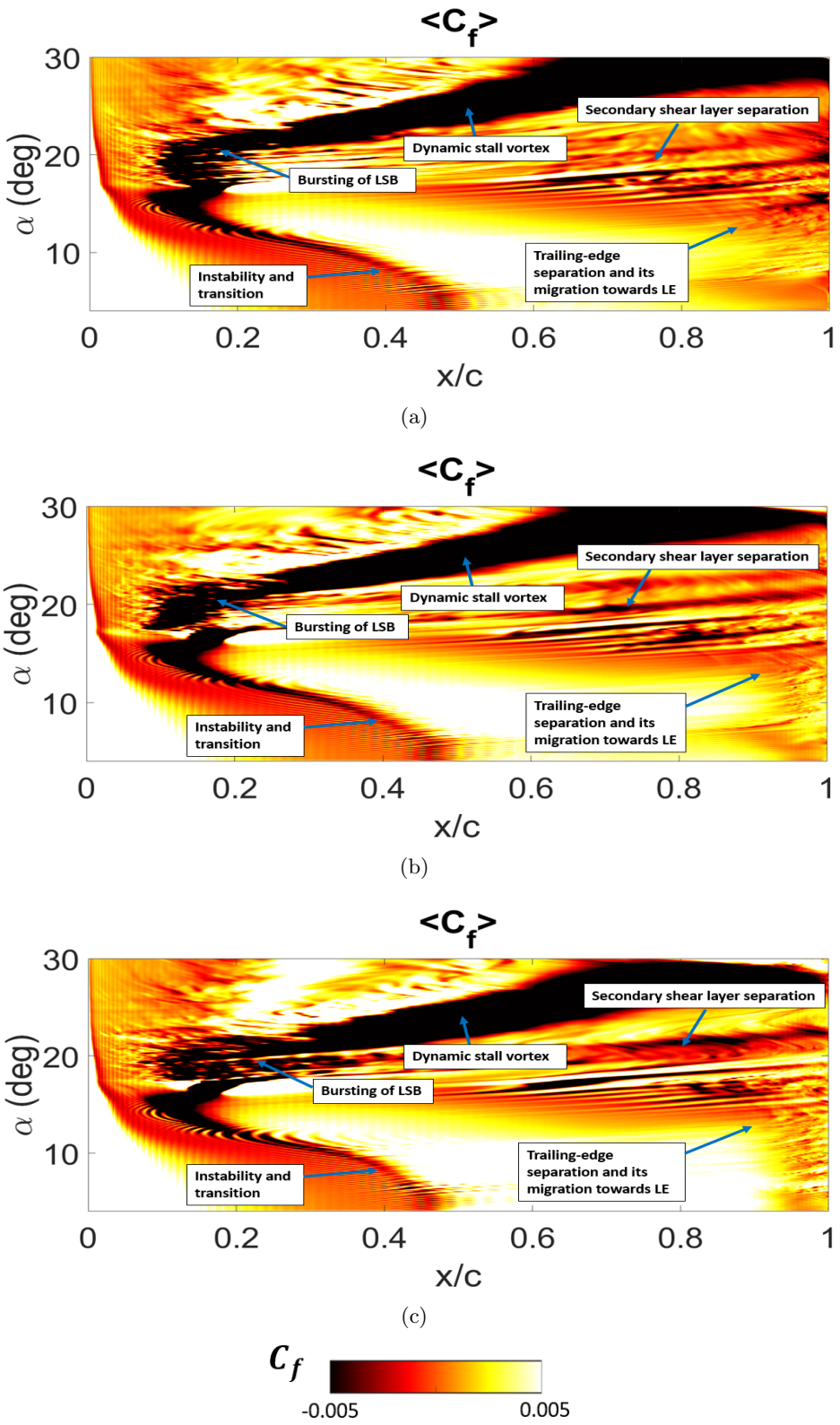

FIGURE 3.8. Spanwise-averaged C_f contours: (a) baseline ($\Delta b = 0$), (b) $\Delta b = 3$, and (c) $\Delta b = 4$ during different stages in the dynamic stall process.

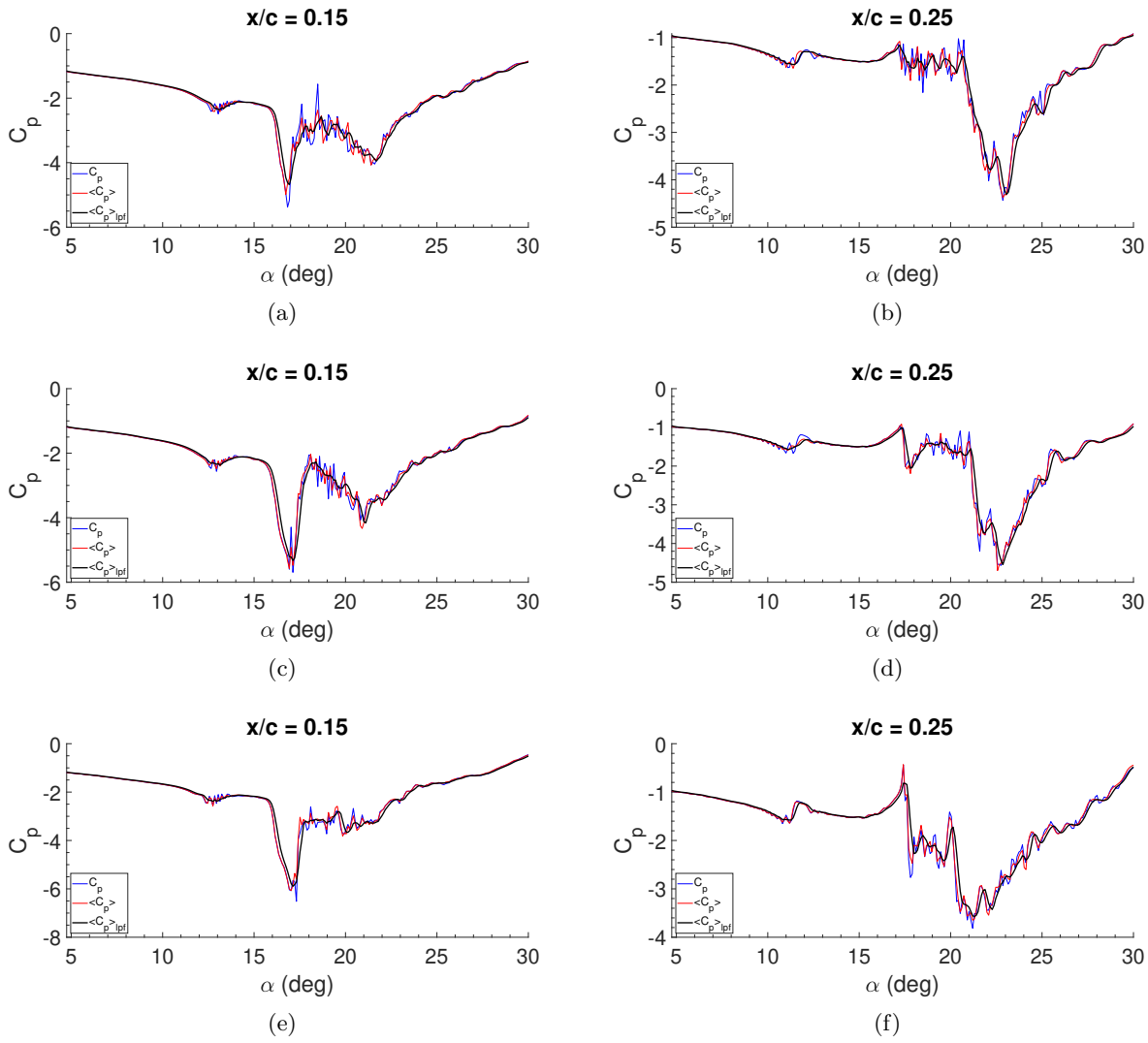

FIGURE 3.9. Representations of instantaneous, spanwise-averaged, and low-pass-filtered C_p at: (a) x/c=0.15 for baseline ($\Delta b = 0$), (b) x/c=0.25 for baseline ($\Delta b = 0$), (c) x/c=0.15 for $\Delta b = 3$, (d) x/c=0.25 for $\Delta b = 3$, (e) x/c=0.15 for $\Delta b = 4$, and (f) x/c=0.25 for $\Delta b = 4$.

3.3.4. General Flow Physics. The reasoning behind the behavior of dynamic stall development can be further supported by analyzing the flow physics during the critical stages. Figures 3.10 and 3.11 show the vorticity magnitude during various stages for the ramp-up pitching motion. In the earlier stages (at lower AoAs), the formation of the LSB can be seen through the vorticity magnitude production at the leading edge for both the baseline and morphed cases. Additionally, as the AoA increases, there is a gradual increase in boundary layer thickness. The flow separation

near the trailing edge develops and the trailing edge vortex grows during the increase in vorticity production. At $\alpha = 18°$, the leading-edge vortices are generated for all the three cases. At $\alpha = 20.3°$, $\Delta b = 4$ shows the development of the large vortex near the leading edge, indicating the bursting of the LSB. The same phenomenon occurs at $\alpha = 21.9°$ for the baseline and $\Delta b = 3$ cases. A secondary shear layer detachment is shown for $\Delta b = 3$ and $\Delta b = 4$ cases at $\alpha = 21.9°$ and $\alpha = 23.8°$. At $\alpha = 23.8°$, the DSV appears distinct for the baseline and $\Delta b = 3$ cases.

The overall behavior of the unsteady flow for the baseline case and the morphed cases is shown in Figs. 3.12 and 3.13 by the instantaneous contours of eddy viscosity. Figure 3.12 shows the gradual thickening of the turbulent boundary layer. At $\alpha = 13.7°$, the turbulent boundary layer remains relatively the same for all the airfoils. At $\alpha = 16.1°$, the trailing-edge separation moves toward the leading edge and meets the LSB, as demonstrated by a small bulge near the leading edge. At $\alpha = 18°$, small vortices are emitted, and these vortices eventually merge and become the DSV. Moreover, it can be seen that the middle section is calmer for the morphed cases, with more motion occurring at the leading edge and trailing edge. At $\alpha = 20.3°$, the coalition of smaller vortices begins to occur for the morphed case of $\Delta b = 4$, and the similar event occurs for the baseline and morphed case of $\Delta b = 3$ at $\alpha = 21.9°$. Furthermore, at $\alpha = 21.9°$, there is a greater indication of secondary shear layer vortex on the middle and aft airfoil sections in the $\Delta b = 3$ and $\Delta b = 4$ cases compared to the baseline case. When $\alpha = 23.8°$ is reached, there is evidence of the main DSV event occurring, with the $\Delta b = 4$ case developing into a larger DSV.

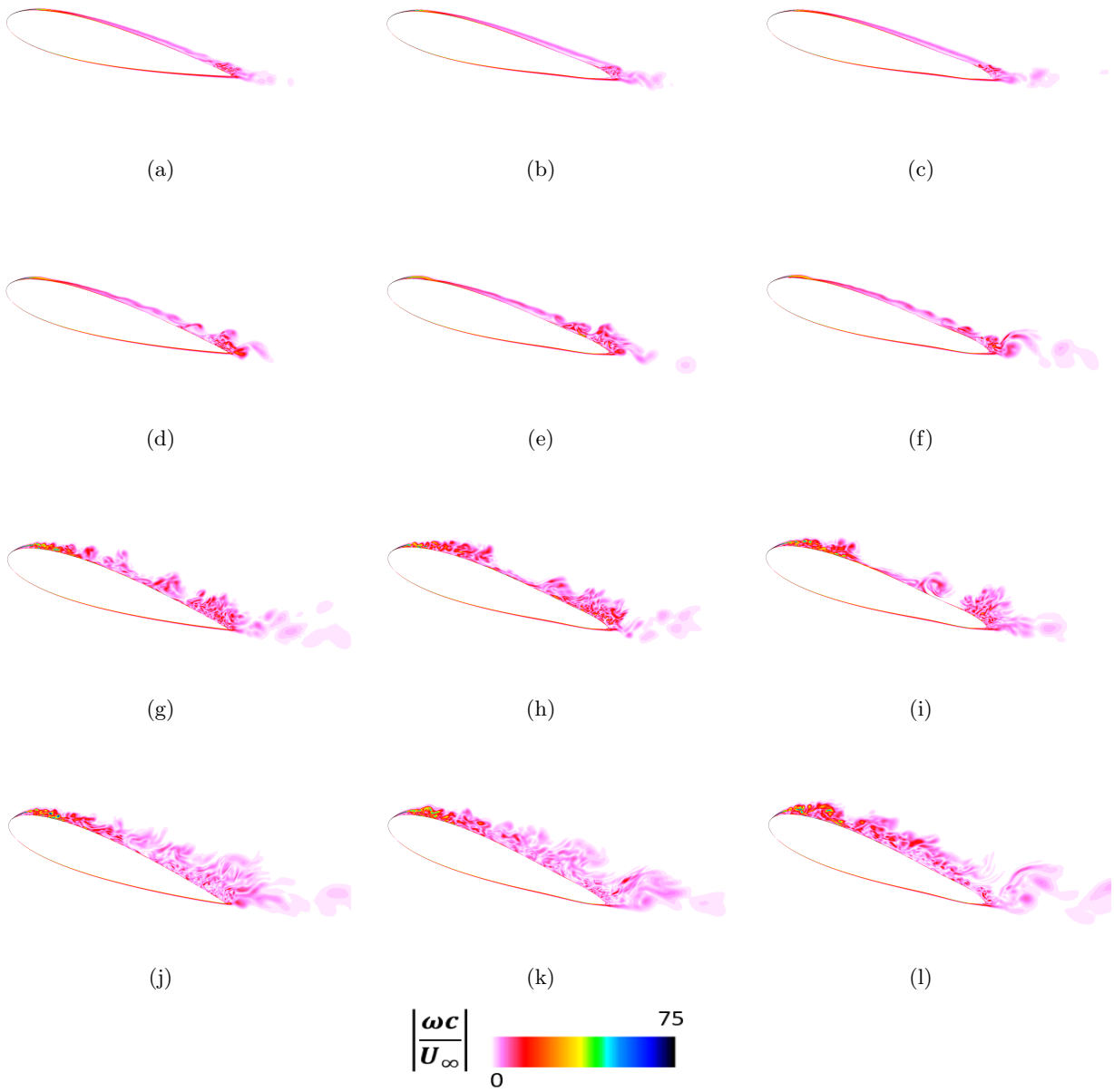

FIGURE 3.10. Instantaneous (midplane) contours of vorticity magnitude at α: (a) 13.7° (baseline $\Delta b = 0$), (b) 13.7° ($\Delta b = 3$), (c) 13.7° ($\Delta b = 4$), (d) 16.1° (baseline $\Delta b = 0$), (e) 16.1° ($\Delta b = 3$), (f) 16.1° ($\Delta b = 4$), (g) 18° (baseline $\Delta b = 0$), (h) 18° ($\Delta b = 3$), (i) 18° ($\Delta b = 4$), (j) 20.3° (baseline $\Delta b = 0$), (k) 20.3° ($\Delta b = 3$), and (l) 20.3° ($\Delta b = 4$).

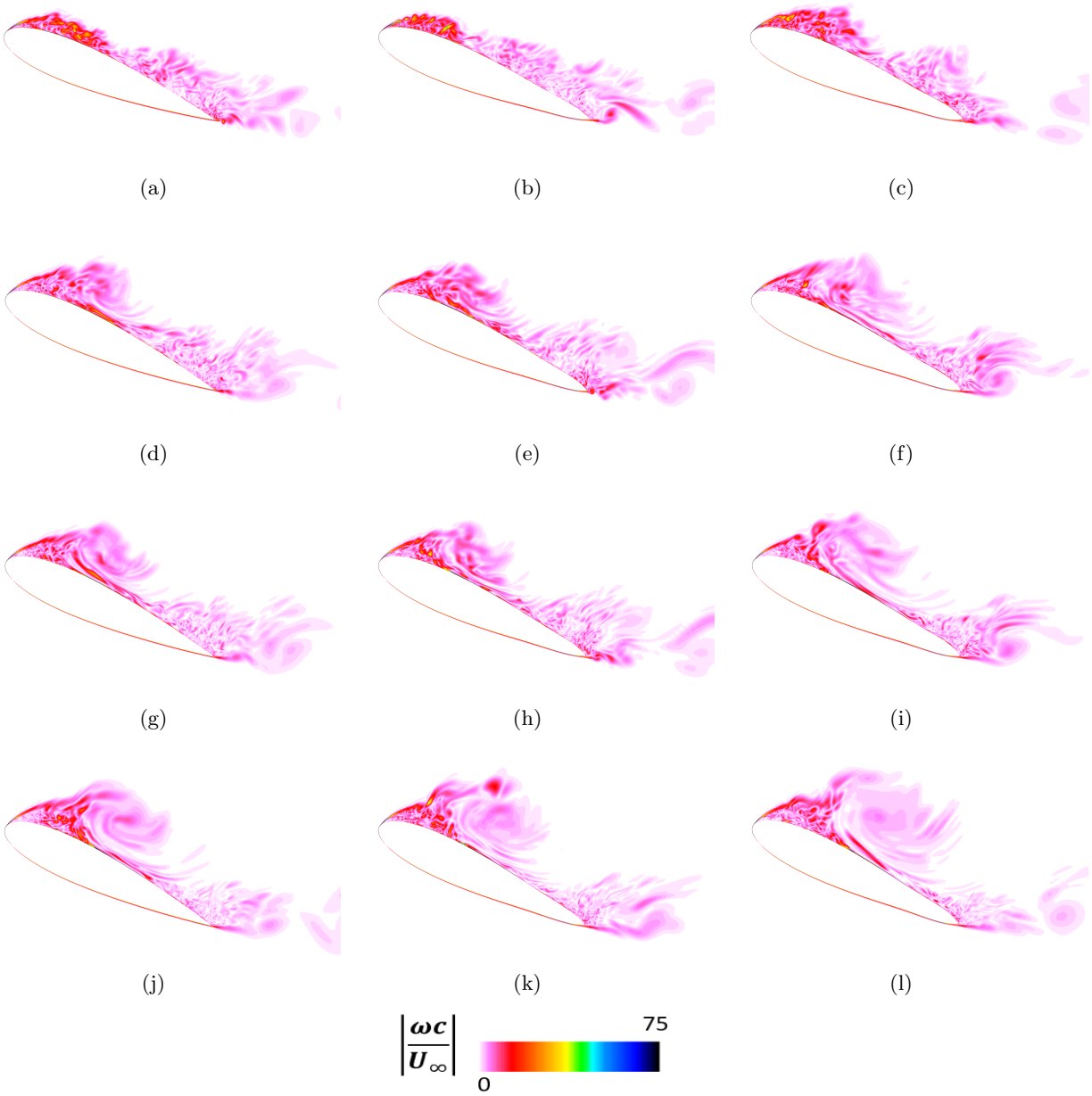

FIGURE 3.11. Instantaneous (midplane) contours of vorticity magnitude at α: (a) 21.9° (baseline $\Delta b = 0$), (b) 21.9° ($\Delta b = 3$), (c) 21.9° ($\Delta b = 4$), (d) 23.8° (baseline $\Delta b = 0$), (e) 23.8° ($\Delta b = 3$), (f) 23.8° ($\Delta b = 4$), (g) 24.2° (baseline $\Delta b = 0$), (h) 24.2° ($\Delta b = 3$), (i) 24.2° ($\Delta b = 4$), (j) 25.4° (baseline $\Delta b = 0$), (k) 25.4° ($\Delta b = 3$), and (l) 25.4° ($\Delta b = 4$).

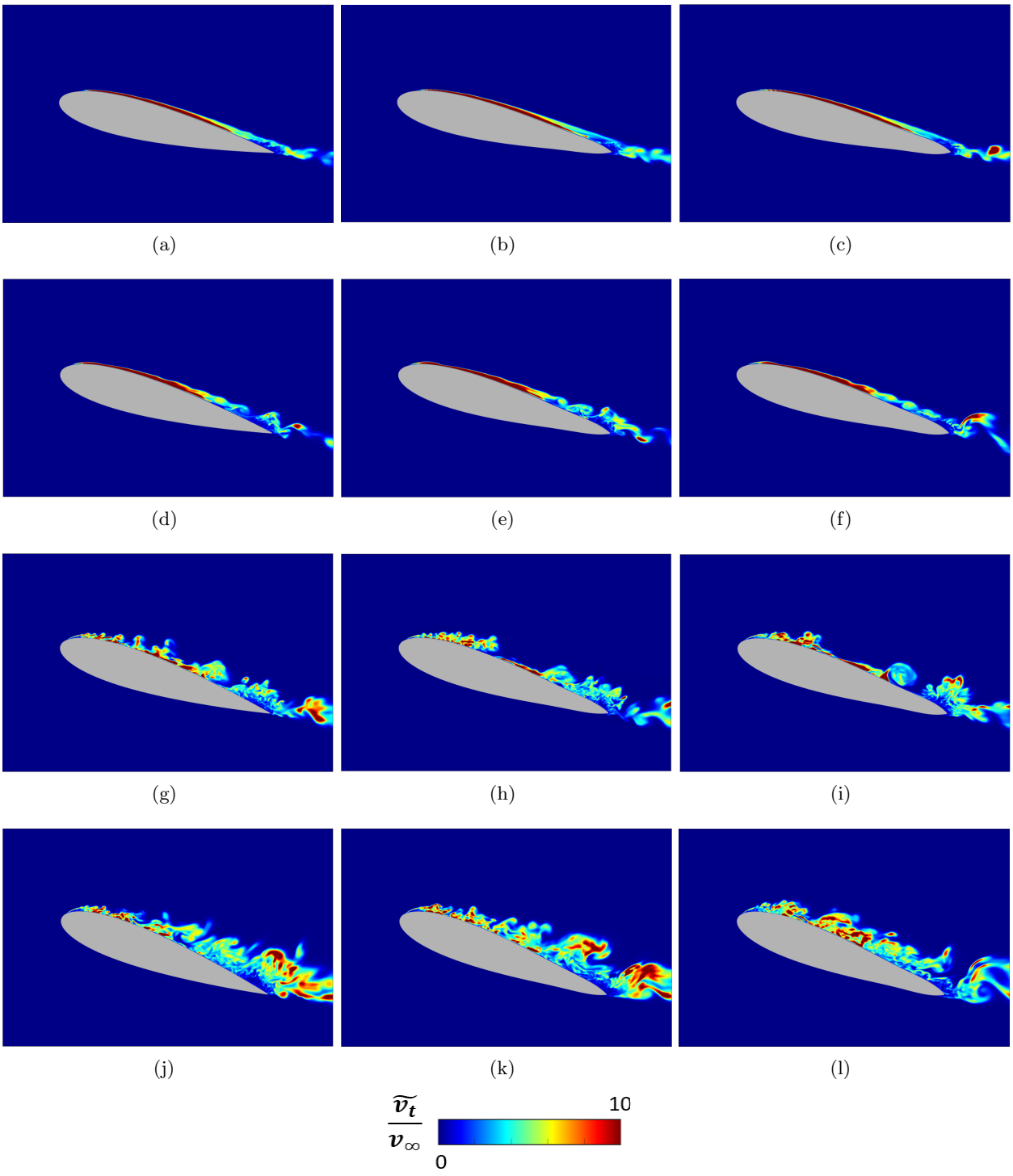

FIGURE 3.12. Instantaneous (midplane) contours of normalized eddy viscosity at α: (a) 13.7° (baseline $\Delta b = 0$), (b) 13.7° ($\Delta b = 3$), (c) 13.7° ($\Delta b = 4$), (d) 16.1° (baseline $\Delta b = 0$), (e) 16.1° ($\Delta b = 3$), (f) 16.1° ($\Delta b = 4$), (g) 18° (baseline $\Delta b = 0$), (h) 18° ($\Delta b = 3$), (i) 18° ($\Delta b = 4$), (j) 20.3° (baseline $\Delta b = 0$), (k) 20.3° ($\Delta b = 3$), and (l) 20.3° ($\Delta b = 4$).

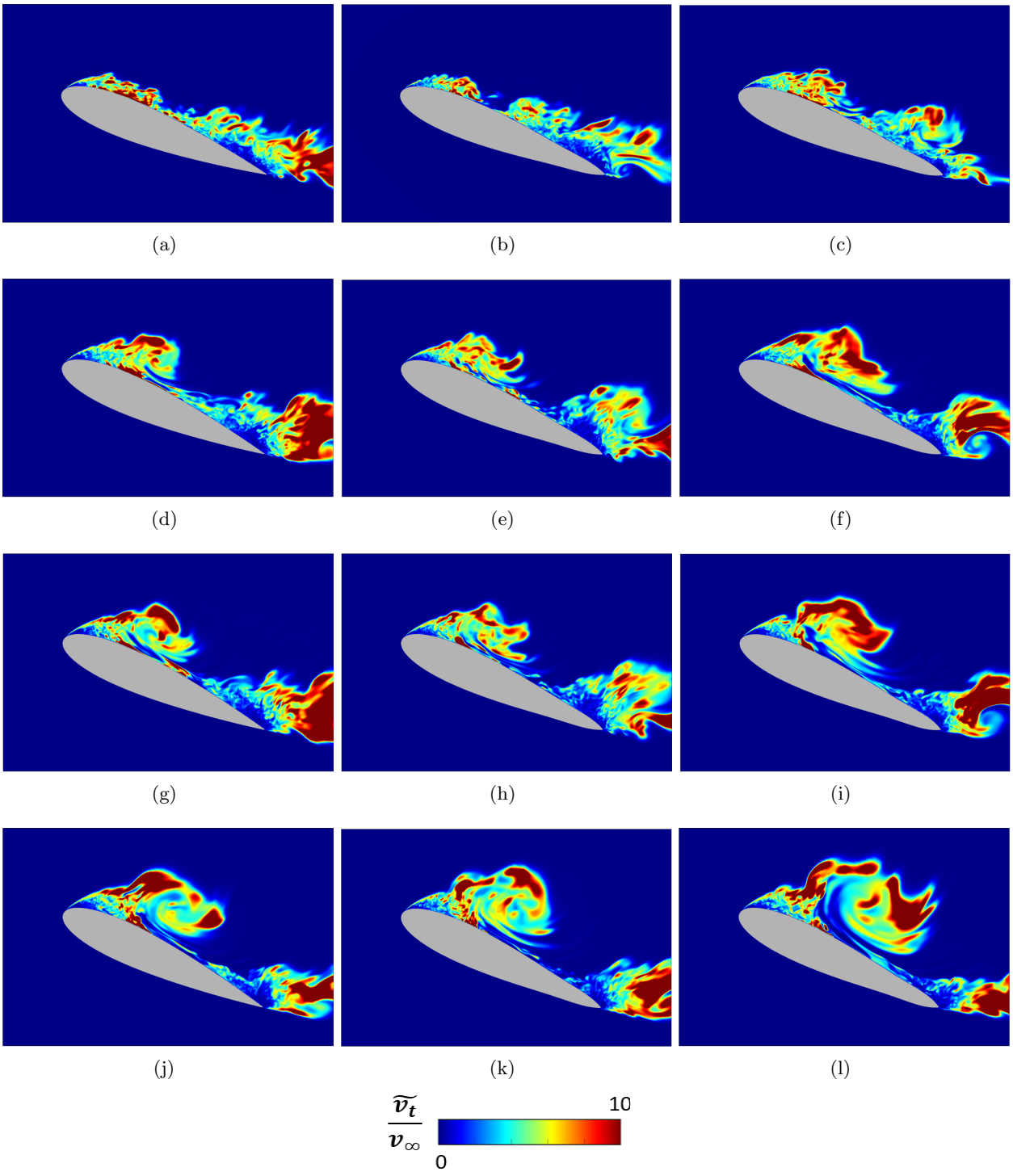

FIGURE 3.13. Instantaneous (midplane) contours of normalized eddy viscosity at α: (a) 21.9° (baseline $\Delta b = 0$), (b) 21.9° ($\Delta b = 3$), (c) 21.9° ($\Delta b = 4$), (d) 23.8° (baseline $\Delta b = 0$), (e) 23.8° ($\Delta b = 3$), (f) 23.8° ($\Delta b = 4$), (g) 24.2° (baseline $\Delta b = 0$), (h) 24.2° ($\Delta b = 3$), (i) 24.2° ($\Delta b = 4$), (j) 25.4° (baseline $\Delta b = 0$), (k) 25.4° ($\Delta b = 3$), and (l) 25.4° ($\Delta b = 4$).

Figures 3.14 and 3.15 show the normalized velocity with the maximum magnitude of zero, representing the reversed flow around the baseline and morphed airfoils. At $\alpha = 13.7°$, there is already an indication of separated flow forming at the trailing edge and the formation of the LSB at the leading edge. At $\alpha = 16.1°$, the trailing-edge separation moves toward the leading edge and meets LSB near the leading edge. The bubble size continues to increase at $\alpha = 18°$. At $\alpha = 20.3°$, the LSB of the $\Delta b = 4$ case is already bursting. This finding is consistent with the results in the C_p plots shown in Fig. 3.5 in Section 3.3.3, where there is a suction collapse at $\alpha = 20.3°$ for the $\Delta b = 4$ case. At $\alpha = 21.9°$, the suction collapses and the LSB bursts for the baseline and $\Delta b = 3$ cases. The $\Delta b = 3$ case also shows a secondary shear layer in the middle section. At higher AoAs, DSV is growing and moving toward downstream.

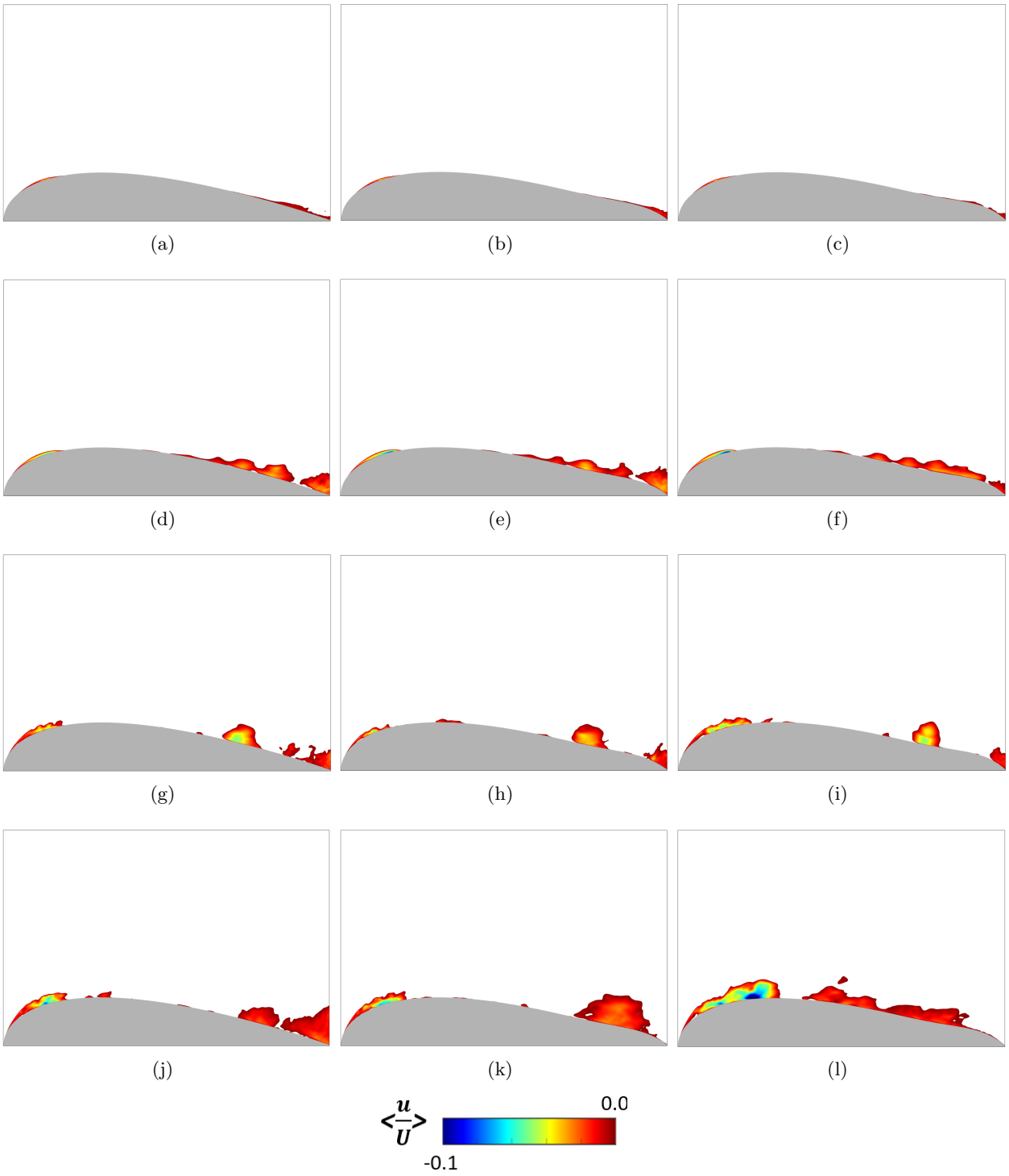

FIGURE 3.14. Instantaneous (midplane) contours of normalized velocity at α: (a) 13.7° (baseline $\Delta b = 0$), (b) 13.7° ($\Delta b = 3$), (c) 13.7° $\Delta b = 4$), (d) 16.1° (baseline $\Delta b = 0$), (e) 16.1° ($\Delta b = 3$), (f) 16.1° (baseline $\Delta b = 4$), (g) 18° (baseline $\Delta b = 0$), (h) 18° ($\Delta b = 3$), (i) 18° ($\Delta b = 4$), (j) 20.3° (baseline $\Delta b = 0$), (k) 20.3° ($\Delta b = 3$), and (l) 20.3° ($\Delta b = 4$).

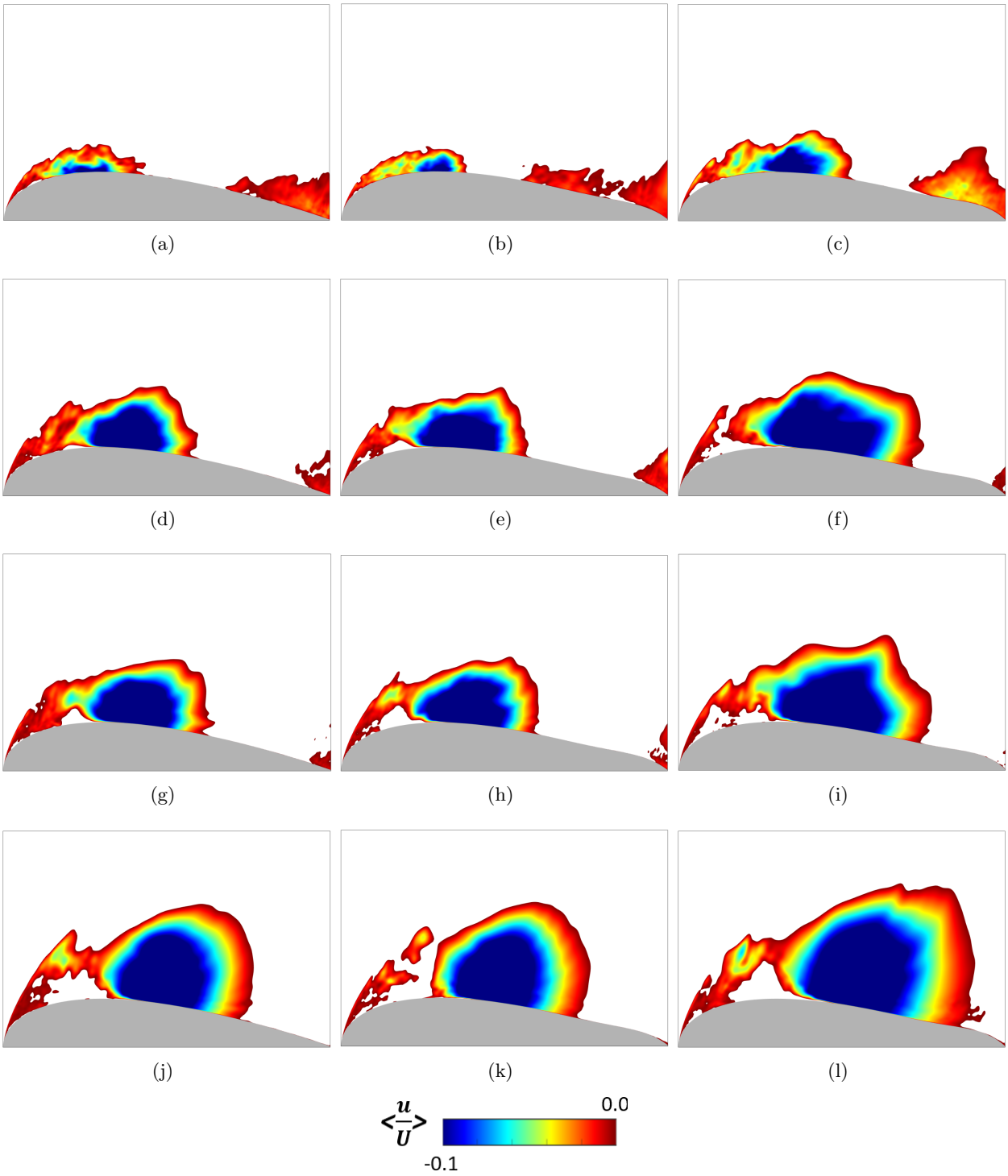

FIGURE 3.15. Instantaneous (midplane) contours of normalized velocity at α: (a) 21.9° (baseline $\Delta b = 0$), (b) 21.9° ($\Delta b = 3$), (c) 21.9° ($\Delta b = 4$), (d) 23.8° (baseline $\Delta b = 0$), (e) 23.8° ($\Delta b = 3$), (f) 23.8° ($\Delta b = 4$), (g) 24.2° (baseline $\Delta b = 0$), (h) 24.2° ($\Delta b = 3$), (i) 24.2° ($\Delta b = 4$), (j) 25.4° (baseline $\Delta b = 0$), (k) 25.4° ($\Delta b = 3$), and (l) 25.4° ($\Delta b = 4$).

3.3.5. Further Investigation of the Trailing-Edge Morphing Design Parameter. This section will focus on a comparison between $\Delta b = -3$ and $\Delta b = 3$. This is an equal and opposite design parameter value investigation to further highlight the trend behavior for positive and negative design parameter values of the trailing-edge morphing boat-tail angle parameter on dynamic stall.

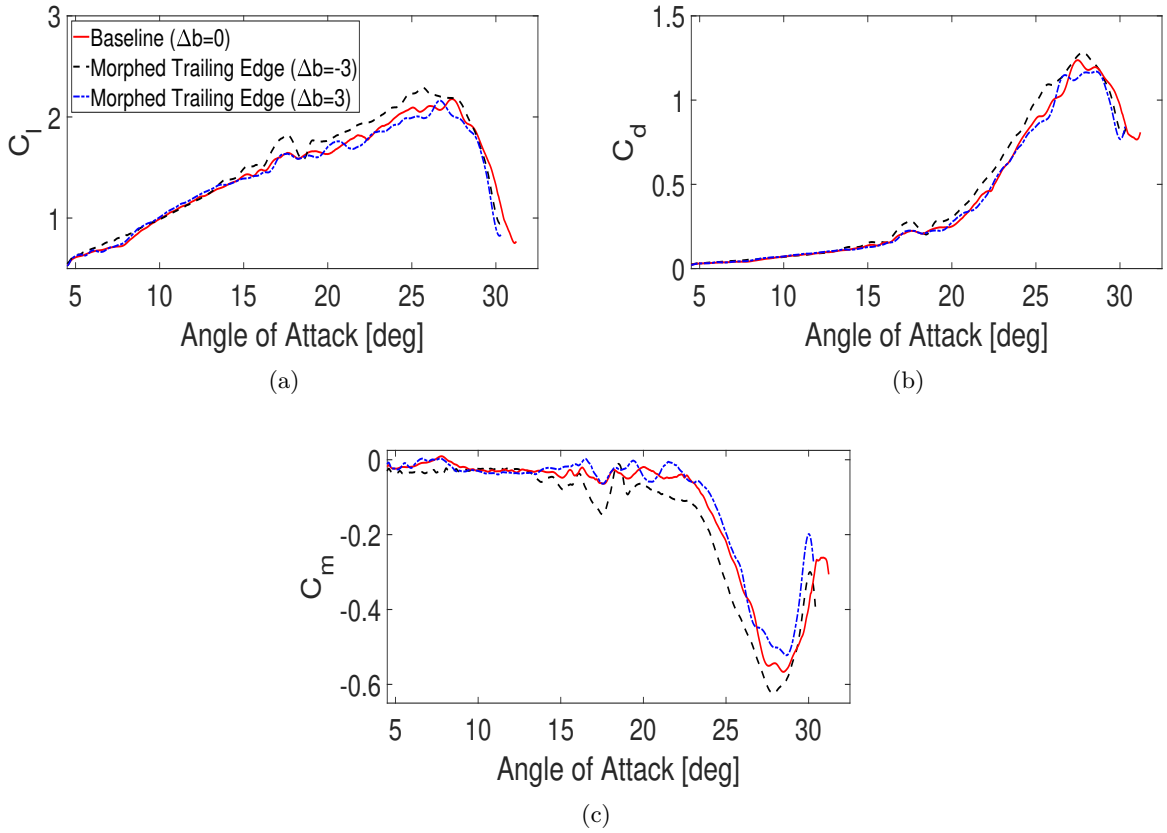

FIGURE 3.16. Comparison of the aerodynamic loading for the baseline ($\Delta b = 0$), $\Delta b = -3$, and $\Delta b = 3$ cases: (a) C_l, (b) C_d, and (c) C_m.

Figure 3.16 shows a comparison of the results for the coefficient of lift (C_l), coefficient of drag (C_d), and coefficient of moment (C_m) for the baseline NACA 0018 airfoil case and the trailing-edge morphed cases (with Δb being equal to -3 and 3). As the boat-tail angle scaling factor increases, the peak magnitudes of C_l, C_d, and C_m all decrease. Moreover, the corresponding stall AoAs for the $\Delta b = -3$ occur earlier compared to baseline and $\Delta b = 3$. There is also an oscillation of a substantial amplitude occurring between AoAs of approximately 16° to 18° for the $\Delta b = -3$ case. As explained previously, the reduction trends of C_l and C_m are not exactly linear as the Δb scaling factor increases. In both of these morphed cases shown here, the peak magnitudes for C_m decrease

more significantly compared to C_l. Overall, C_l is reduced by 4.9% and C_m by 9.1% between the Δb=-3 case and the baseline case (Δb=0), and C_l is reduced by 0.7% and C_m by 7.8% between the baseline case (Δb=0) and the Δb=3 case. In summary, trailing-edge morphing influences the aerodynamic loading and reduces the magnitude of C_m, though the effect is relatively smaller compared to typical leading-edge morphing [3, 45, 87].

The dynamic stall process is characterized by various stages in its development, and these crucial events and behaviors were explained in the beginning of Section 3.3.3. Figure 3.17 presents the spanwise-averaged surface pressure for the baseline NACA 0018 airfoil case and the trailing-edge morphed cases (with Δb being equal to -3 and 3), from an initial stage ($\alpha = 13.7°$) where the LSB forms at the leading edge, to a stage ($\alpha = 25.4°$) where the DSV is fully formed and starts to propagate downstream and detach from the surface. To sum up again, for the baseline case, the suction collapses at $\alpha = 21.9°$ where the LSB size increases with a noticeable peak at around $x/c = 0.2$. For the $\Delta b = 3$ trailing-edge morphed case, the suction collapse occurs at the same AoA. However, a large peak at around $x/c = 0.2$ is not visible. In comparison, it is shown that, for the $\Delta b = -3$ morphed trailing-edge case, the suction collapse starts to occur before $\alpha = 21.9°$, which also shows an initial development of the DSV. This behavior is evident in Fig. 3.17(b), where the plateau starts to drop at around $\alpha = 20.3°$, signaling that the LSB is beginning to burst. Of all three cases, the $\Delta b = -3$ morphed trailing-edge case displays the furthest shift of DSV at $\alpha = 23.8°$ through $\alpha = 25.4°$ in the chordwise direction. The widths of the C_p bell curves demonstrate the influence of the aerodynamic loading characteristics. A longer width corresponds a stronger influence and a shorter width corresponds to a weaker influence. It can be seen that the $\Delta b = -3$ exhibits the widest width, and the $\Delta b = 3$ exhibits the narrowest width for the C_p bell curves near the DSV region. The results match the aerodynamic loading characteristics shown in the previous Fig. 3.16.

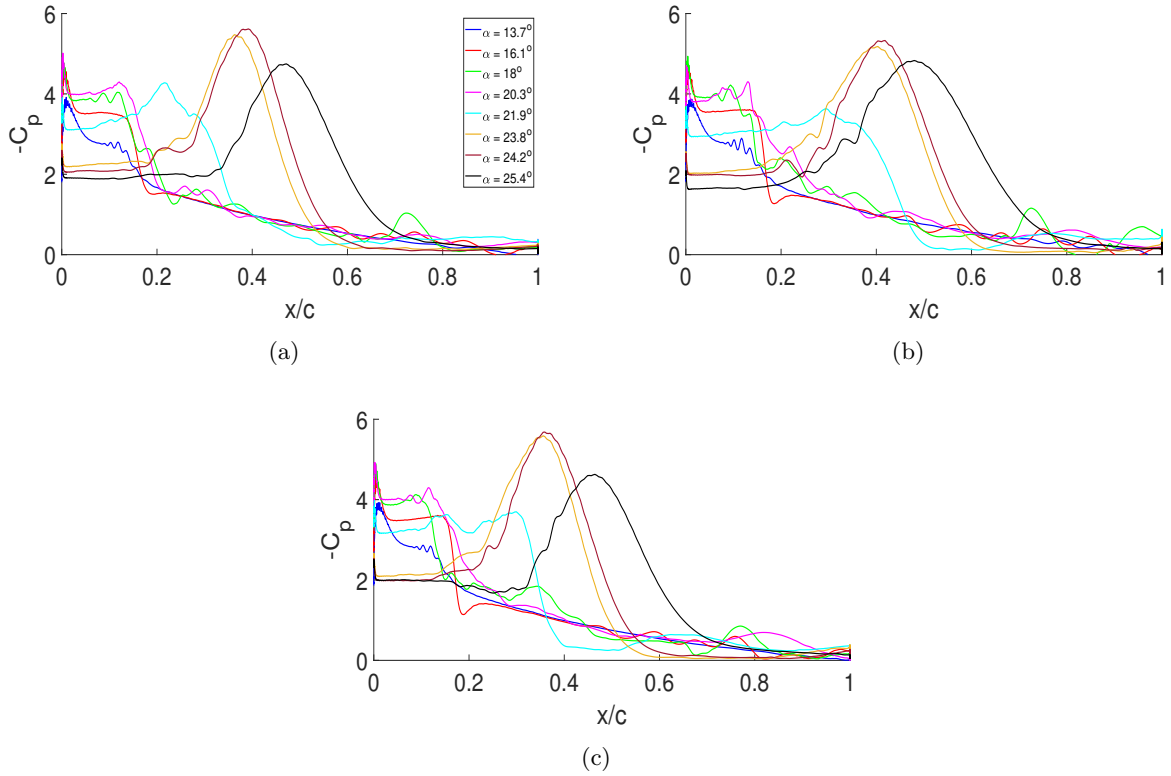

FIGURE 3.17. Spanwise-averaged C_p for the: (a) baseline ($\Delta b = 0$), (b) $\Delta b = -3$, and (c) $\Delta b = 3$.

Figure 3.18 show the skin friction contours, illustrating the complete formation of the dynamic stall flow topology. These contour plots depict the development of the entire dynamic stall process on the airfoil surface across the full range of AoA for the baseline, $\Delta b = -3$, and $\Delta b = 3$. To outline the comparison, it is seen that the trailing edge separation rapidly advances toward the leading edge, encountering the LSB near the leading edge at around $\alpha = 16.1°$. Following this encounter, the LSB eventually bursts at $\alpha = 21.9°$ for the baseline and $\Delta b = 3$ case, and slightly before $\alpha = 21.9°$ for the $\Delta b = -3$ case. After the bursting of the LSB, the DSV forms and moves toward the trailing edge. It is important to note that the results indicate that the morphed airfoils exhibit different C_f contours at their midsection x/c locations compared to the baseline case, particularly around the event of the LSB bursting. The negative C_f values at the middle and aft sections near $\alpha = 21.9°$ indicate secondary shear layer separation in this region. The shear layer separation is more intense for the morphed trailing-edge cases ($\Delta b = -3$ and $\Delta b = 3$). Moreover, the $\Delta b = -3$ morphed trailing-edge case exhibits the strongest trailing-edge separation at the trailing edge.

Another aspect of this DSV process is the formation of long and slender streamwise vortices, which are depicted through the iso-surfaces of Q-criterion, or measure of the swirling strength, as shown in Fig. 3.19. Batther and Lee [4] have previously investigated these vortices and concluded that these vortices provide information on the unsteadiness, the onset of dynamic stall, detachment of the DSV, and the impact on the overall dynamic stall process. In this case, it can be observed and concluded that the longer vortices indicate a stronger influence of the aerodynamic loading characteristics. For all AoAs near the DSV shown in Fig. 3.19, the vortices are the longest for the $\Delta b = -3$ case. Likewise, this indicates that $\Delta b = -3$ has the strongest aerodynamic loading effect.

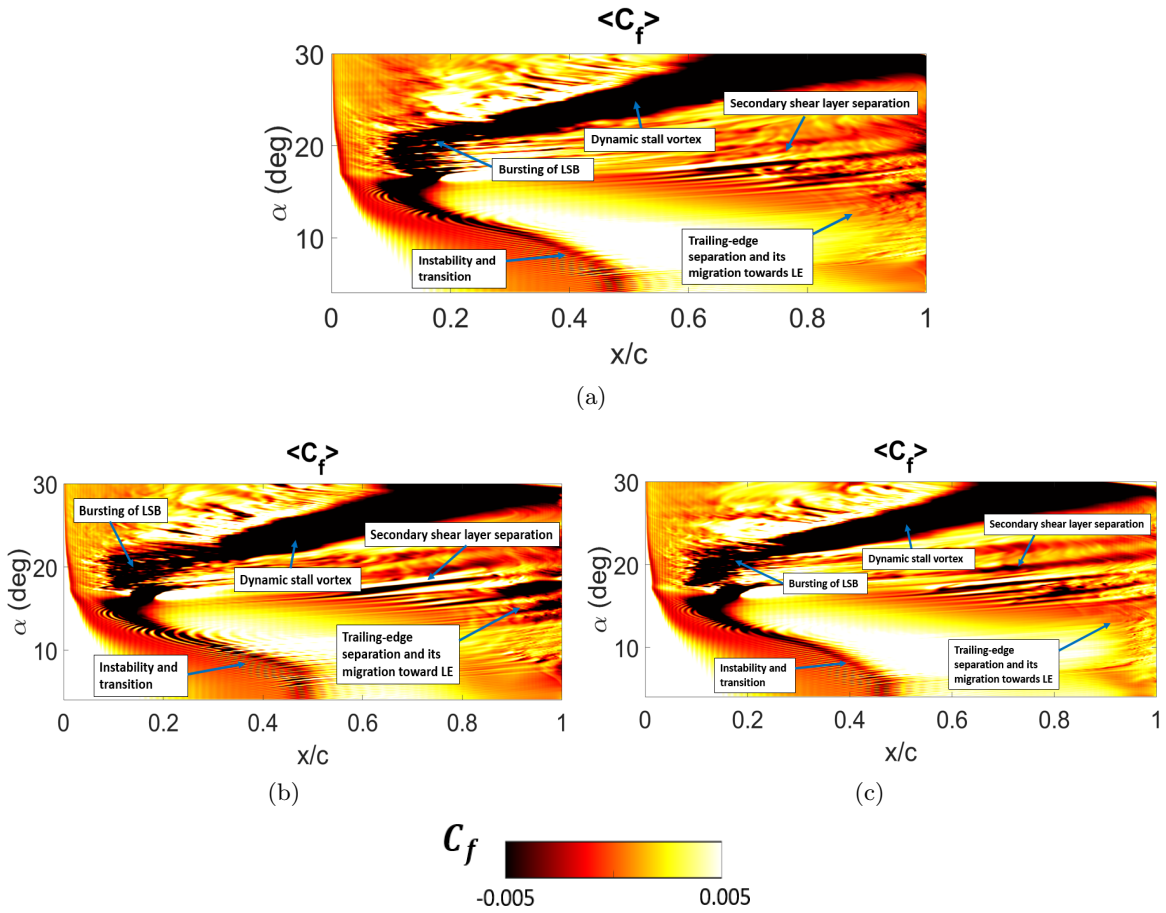

FIGURE 3.18. Spanwise-averaged C_f contours: (a) baseline ($\Delta b = 0$), (b) $\Delta b = -3$, and (c) $\Delta b = 3$ during different stages in the dynamic stall process.

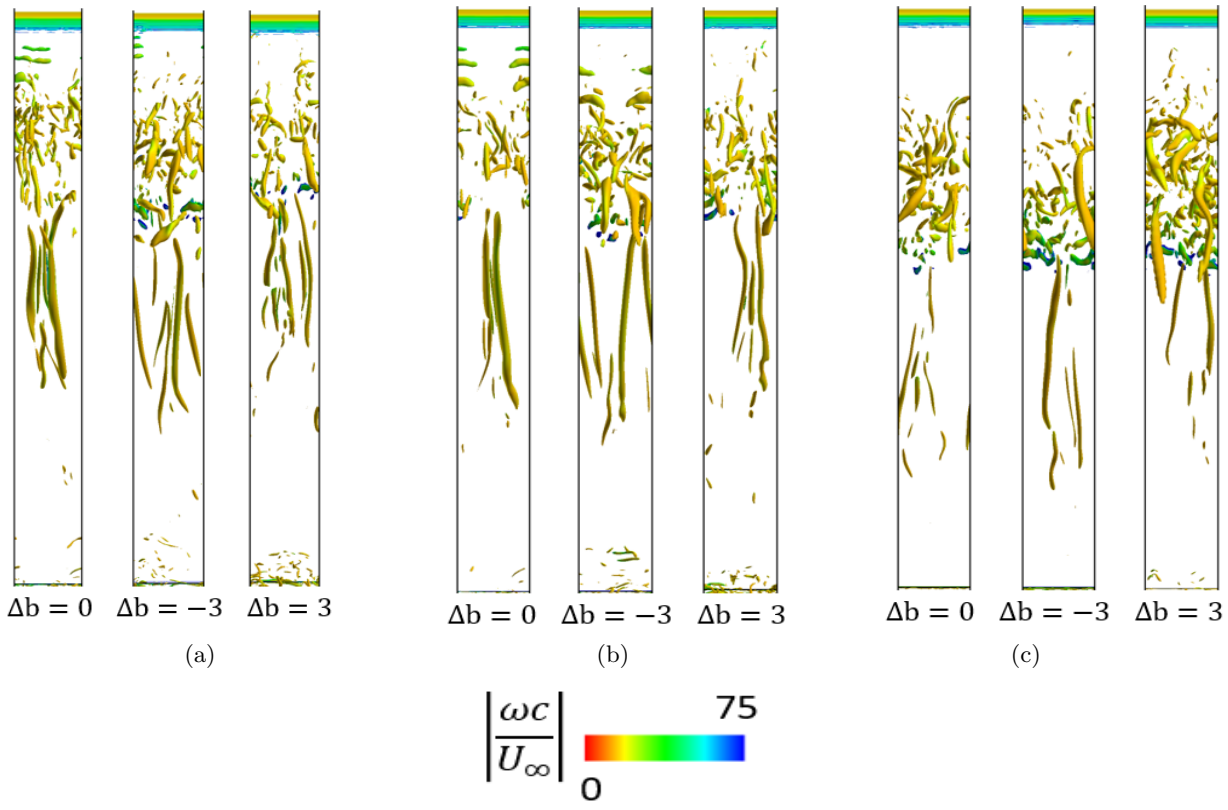

FIGURE 3.19. Iso-surfaces of Q-criterion = 100 colored by vorticity magnitude for the baseline ($\Delta b = 0$), and trailing-edge morphing geometries $\Delta b = -3$ and $\Delta b = 3$: (a) α=23.8°, (b) α=24.2°, and (c) α=25.4°.

The reasoning behind the behavior of dynamic stall development can be further supported by analyzing the flow physics during the critical stages of development for the $\Delta b = -3$ morphed airfoil case. The overall behavior of the unsteady flow for the $\Delta b = -3$ case is shown in Fig. 3.20 by the instantaneous contours of eddy viscosity. At $\alpha = 20.3°$, the coalition of smaller vortices begins to occur for the morphed case of $\Delta b = -3$, (whereas this similar event occurs for the baseline and morphed case of $\Delta b = 3$ at $\alpha = 21.9°$ as seen in Fig. 3.13). Furthermore, at $\alpha = 21.9°$, there is a greater indication of secondary shear layer vortex on the middle and aft airfoil sections in the $\Delta b = -3$ compared to the baseline and $\Delta b = 3$ cases. When $\alpha = 23.8°$ is reached, there is evidence of the main DSV event occurring, with the $\Delta b = -3$ case developing into a larger and stronger DSV that persists until $\alpha = 25.4°$. Overall, the baseline and $\Delta b = -3$ cases demonstrate a larger and stronger trailing-edge separation starting at $\alpha = 23.8°$ but the $\Delta b = 3$ does not reach a similar intensity until at $\alpha = 25.4°$.

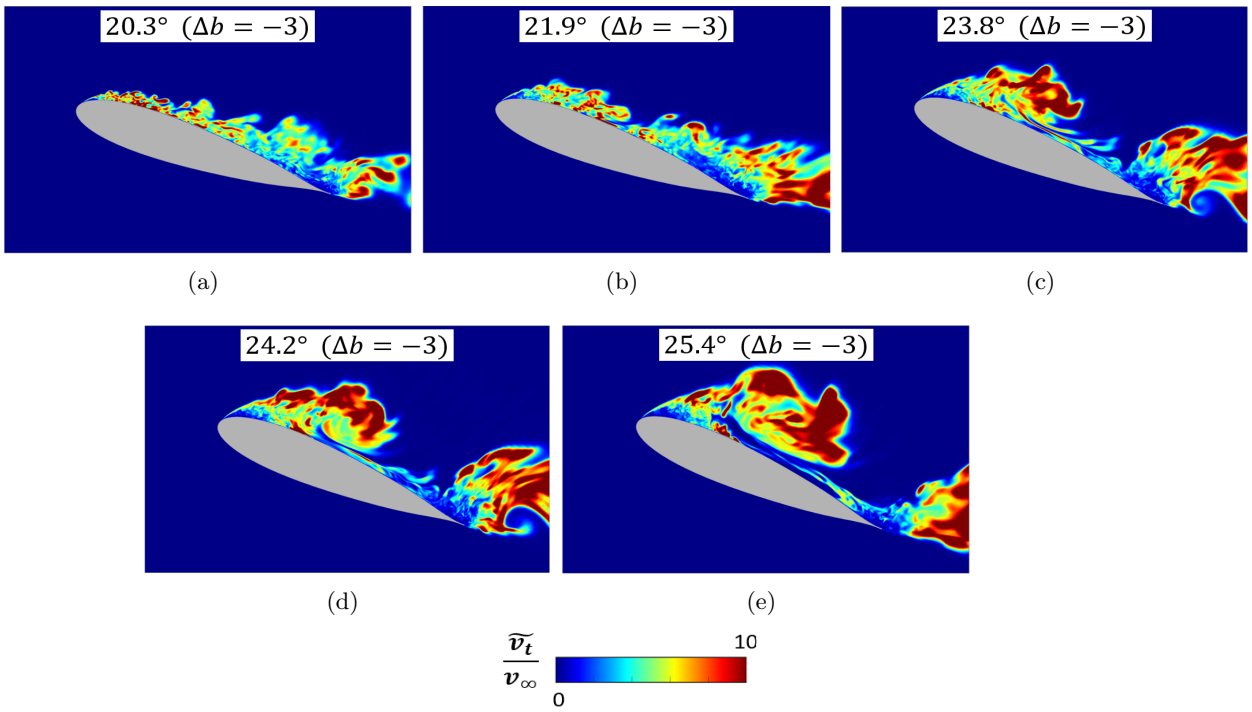

FIGURE 3.20. Instantaneous (midplane) contours of normalized eddy viscosity for $\Delta b = -3$.

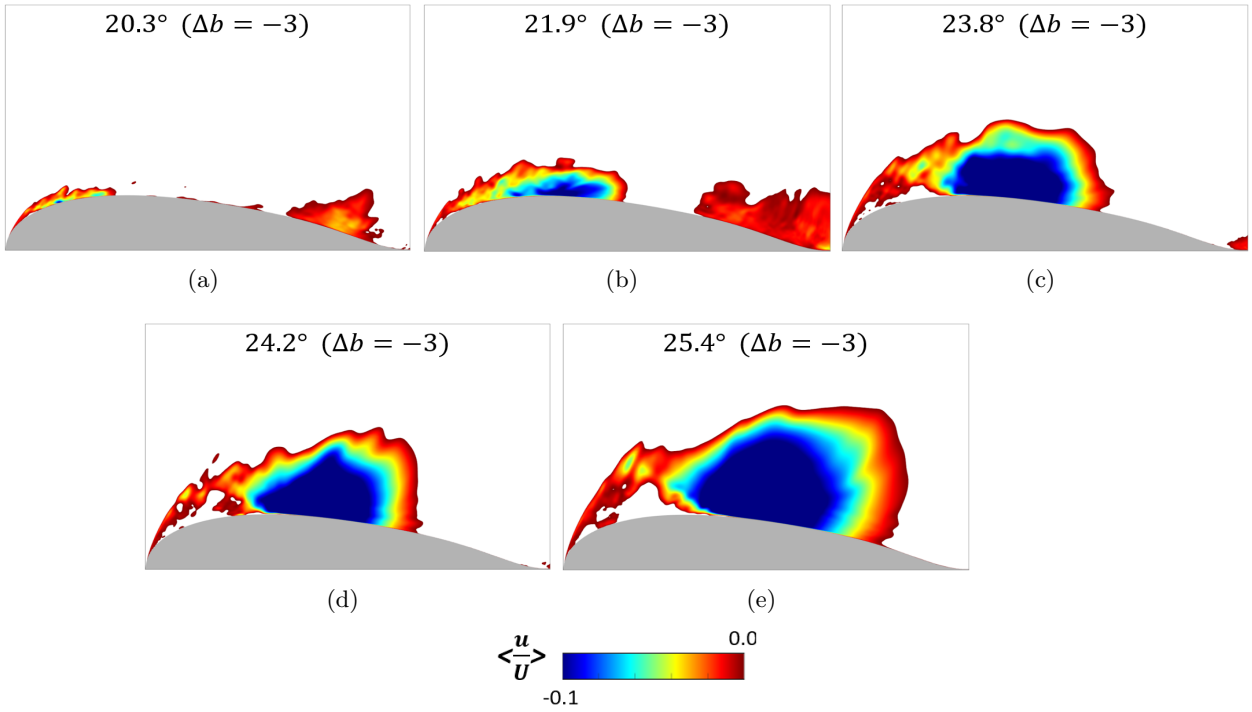

FIGURE 3.21. Instantaneous (midplane) contours of normalized velocity for $\Delta b = -3$.

Figure 3.21 shows the normalized velocity with the maximum magnitude of zero, representing the reversed flow for the $\Delta b = -3$ morphed airfoil case. At $\alpha = 20.3°$, the LSB of the $\Delta b = -3$ case is beginning to burst. This finding is consistent with the results in the C_p plots shown in Fig. 3.17, where there is a suction collapse that begins to initiate between $\alpha = 20.3°$ and $\alpha = 21.9°$ for the $\Delta b = -3$ case. This is more clearly revealed here in Fig. 3.21. At $\alpha = 21.9°$, the suction collapses and the LSB bursts sooner for $\Delta b = -3$ (compared to the baseline and $\Delta b = 3$ cases as seen in Fig. 3.15). It is also shown that trailing-edge separation becomes pronounced and progresses toward the leading edge, culminating in the bursting of the LSB. When the dynamic stall onset is reached, the DSV continues to grow and move downstream at higher AoAs. At $\alpha = 25.4°$, the reversed separated flow becomes the largest for the $\Delta b = -3$ case and occupies a greater region of the airfoil suction surface compared to the baseline and $\Delta b = 3$ cases.

3.4. Summary

This chapter investigated and analyzed the effect of trailing-edge morphing on dynamic stall using DDES with a transitional turbulence model. DDES was used to predict the aerodynamic loads for a baseline NACA 0018 airfoil and trailing-edge morphed airfoils with Δb equal to 3 and 4. In the morphed cases, the C_m magnitude decreased more significantly compared to C_l. Overall, C_l was reduced by 0.7% and C_m by 7.8% for the Δb=3 case compared to the baseline airfoil. C_l was reduced by 2.7% and C_m by 8.3% for the Δb=4 case. Additionally, C_l was reduced by 4.9% and C_m by 9.1% for the baseline case compared to the Δb=-3 case.

The dynamic stall development stages were discussed in detail through analyzing the spanwise-averaged C_p and C_f plots at certain angles and regions. An in-depth study of the flow physics was used to explain the complex features during the dynamic stall stages. This included understanding the formation and collapse of the LSB, the unstable shear layers, and the propagation of the DSV over the airfoil. The results indicated that the behavior of the secondary shear layer (in the high x/c range) intensified as the trailing edge boat-tail angle scaling factor (Δb) was implemented. Additionally, the Δb=4 case exhibited the earliest bursting of the LSB, resulting in the faster movement and earlier onset of the DSV compared to the Δb=3 and baseline cases. Also, the Δb=-3 case exhibited the earlier onset and a larger DSV compared to the Δb=3 and baseline cases. The vorticity magnitude and the eddy viscosity diagrams for the baseline and morphed

cases were compared and examined. As the AoA increased, there was a gradual increase in the boundary layer thickness. The flow separation near the trailing edge and the trailing-edge vortex also grew during the increase in vorticity production. Furthermore, the spanwise-averaged reverse flow contours were analyzed to further support the conclusions on the exact behavior of how the trailing-edge separation encountered the LSB and influenced the bursting of the LSB. Overall, it was demonstrated that a small change in the trailing edge could have a global effect on the dynamic stall process.

CHAPTER 4

Effect of Particle Impact Induced Surface Roughness

4.1. Introduction

The impact of surface roughness on dynamic stall represents a pivotal area of research, particularly taking into account environmental factors such as rain, sand, dirt, and ice. Surface roughness, especially at the leading edge of airfoils, can significantly alter unsteady flow separation patterns and the characteristics of DSV, thus affecting the aerodynamic performance and behavior of the turbulent boundary layer during stall conditions [15, 17, 30, 36, 94, 106]. Notably, issues such as erosion and roughness are prevalent in operational wind turbines, leading to reduced lift and overall performance degradation [28]. Airborne devices and fluid-dynamic machinery operating in rainy, sandy, or other harsh weather conditions may experience dynamic stall, imposing penalties on aerodynamic efficiency and performance [32, 43, 83]. Furthermore, studies have demonstrated that aerodynamic efficiency in these systems declines over time due to environmental factors that induce blade surface roughness, presenting a significant challenge in both understanding and quantification [24]. In response, advanced modeling efforts, such as those by Knopp et al. [48], have refined turbulence models to more accurately account for surface roughness, thereby enhancing predictions in turbulent boundary layer flows and skin friction. Lin et al. [61] have proposed a finite particle approach for high-fidelity simulation of helicopter brownouts, offering particle number concentration distributions that enable quantitative risk evaluation of dust clouds. Additionally, Zhu et al. [107] explored the impact of passive vortex generators and leading-edge roughness on dynamic stall. Their findings indicated that leading-edge roughness significantly increases the turbulence kinetic energy (TKE) and suction loss at the leading edge, leading to an earlier onset of separated flow and dynamic stall. The increase in roughness height also corresponds to a general reduction in the linear lift-curve slope. Despite extensive research, a comprehensive understanding of dynamic stall under the influence of particle-impact-induced surface roughness remains elusive.

This underscores the need for continued investigation to deepen our current knowledge and improve the predictive capabilities.

Prediction of DSV is challenging due to several complex factors that affect the formation and behavior of the vortex during dynamic stall conditions, such as unsteady aerodynamics, three-dimensional effects, turbulence and flow separation, transient flow features, computational costs, material and surface effects, etc. Addressing these challenges requires advanced computational techniques, detailed experimental data, and sophisticated modeling approaches to enhance the accuracy and reliability of DSV predictions in dynamic stall scenarios. Batther and Lee [4] employed delayed detached eddy simulations (DDES) and achieved results that were comparable to those obtained from large-eddy simulations (LES) in understanding the flow physics associated with the onset of dynamic stall. A key advantage of their approach was the significantly reduced computational cost of DDES compared to LES. This efficiency positions DDES as a valuable tool for studying complex aerodynamic phenomena while effectively managing computational resources. In a separate study, Khalifa et al. [46] examined the three-dimensional aspects of dynamic stall on a NACA 0012 airfoil using DES solvers. Their research emphasized that dynamic stall is inherently a three-dimensional phenomenon. The findings demonstrated the superiority of three-dimensional simulations over two-dimensional approaches, particularly in accurately capturing the various stages of dynamic stall and more precisely predicting the lift coefficient values. Furthermore, the DES solvers showed exceptional performance when compared to unsteady Reynolds-averaged Navier-Stokes (URANS) solvers, marking a significant advancement in the field of aerodynamic simulations. For the current chapter study, DDES is utilized to investigate the dynamic stall characteristics of an airfoil.

This chapter study aims to bridge the existing knowledge gap by investigating the effects of surface roughness caused by particle impacts on dynamic stall. As previously discussed, surface roughness significantly affects an airfoil's aerodynamic performance. To address this, Lawrence Livermore National Laboratory (LLNL) code ParticleTSim [80] is employed to obtain strike maps of particle impacts and to identify the impact regions on the airfoil. The objective is to analyze the aerodynamic characteristics and the flow physics associated with particle impact-induced surface roughness and its effect on dynamic stall. The details of the dynamic stall characteristics and developmental stages associated with varying surface roughness heights across different impacted regions of the airfoil are included and discussed. Additionally, an analysis of the flow physics related

to these phenomena is conducted. Through this investigation, valuable insights leading to enhanced design strategies for aircraft and fluid-dynamic machinery are provided. The intent is that these results will help optimize their performance and structural integrity under diverse and challenging operational conditions. The primary objectives of the research in this chapter are to evaluate the significance and consequences of particle impact-induced surface roughness on dynamic stall using DDES. Ultimately, these results contribute to a more robust understanding of dynamic stall, aiding in the development of systems better equipped to withstand the rigors of harsh environmental conditions. This chapter research offers a comprehensive perspective on how microscale alterations to surface texture can macroscopically influence aerodynamic behaviors, particularly under dynamic stall conditions.

4.2. Methodology

This section provides an overview of the methodology and solution approach employed in this chapter. In the subsequent subsections, the details of the mesh generation, boundary conditions and numerical scheme, and the methodology for incorporating surface impact-induced roughness are presented.

4.2.1. Mesh Generation. The mesh construction in our study utilizes NASA's mesh software, OVERGRID [18], which is compatible with Chimera grid tools [19]. The 3-D airfoil geometry mesh is visualized in Fig. 4.1. An O-type grid configuration with a blunt trailing edge is used. The airfoil surface is discretized into 800 grid points in the chordwise direction, allocating 600 points to the upper surface and 200 points to the lower surface. The far-field boundary is situated 100 chord lengths from the airfoil surface. In the wall-normal direction, there are 200 points distributed, with 150 points concentrated within the first chord length and the remaining 50 points spanning the subsequent ninety-nine chord lengths. This configuration facilitates significant grid stretching, which aids in the effective dissipation of flow variables at the far-field boundary. Despite the extensive grid stretching, a stretching ratio below 1.3 is maintained, in accordance with best practices as outlined in OVERGRID [18, 86]. The grid resolution at both the leading and trailing edges is set to 0.02% of the chord length, chosen to ensure adequate fidelity in capturing the flow physics, based on established methodologies from previous studies [4, 37, 58, 86]. The spanwise extent of the mesh covers 10% of the chord length, with 100 points uniformly spaced in this direction. Research

by Visbal and Garmann [102] indicated that a 10% spanwise extent is sufficient to capture detailed flow features associated with the onset of DSV. They also recommended grid stretching towards the far-field boundary to enhance the accuracy of the results. The first wall-normal grid height is calibrated to achieve a y^+ value of approximately 0.488, determined iteratively through flat plate approximations and cross-referencing with solution data from relevant test cases.

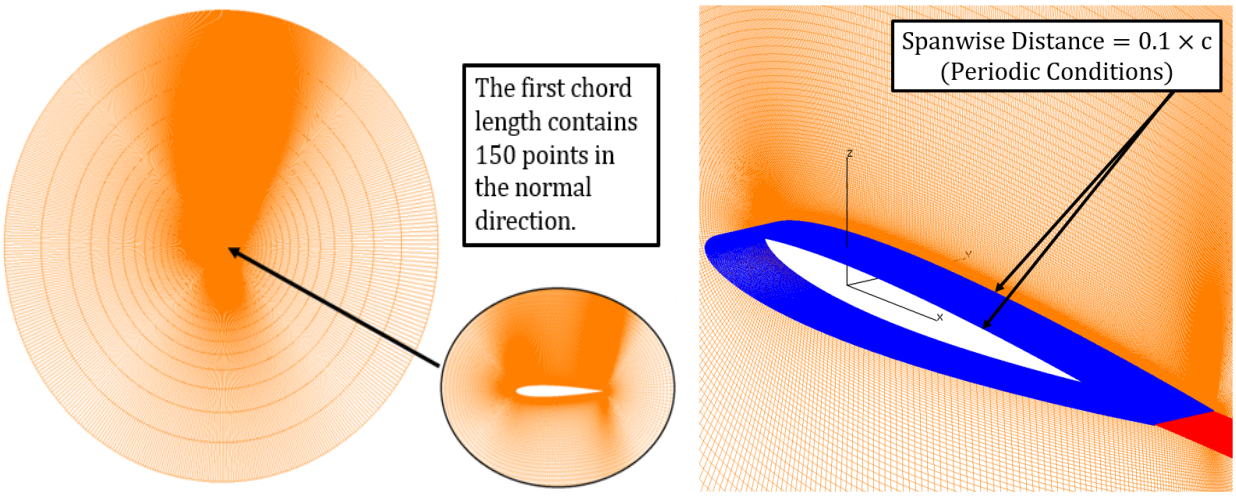

FIGURE 4.1. Overview of the 3-D airfoil section mesh (NACA 0012): (a) O-type mesh (the normal distance of the mesh in the far-field direction is 100 times the chord length); (b) mesh near the airfoil surface and boundary condition (the spanwise distance of the mesh is 10% of the chord length).

4.2.2. Boundary Conditions and Numerical Scheme. The following boundary conditions are prescribed and imposed: no-slip adiabatic condition on the airfoil surface, spanwise periodic conditions, and periodicity in the chordwise direction at the trailing edge. The last boundary condition means that the solution remains the same across the line originating from the midpoint of the trailing edge and extending towards the far field, as visually depicted in Fig. 4.1(b) in red color. These boundary conditions are visually represented in Fig. 4.1. Implementing spanwise periodic conditions is essential for eliminating finite three-dimensional effects, such as tip vortices, while still capturing spanwise flow dynamics and turbulence characteristics.

The OVERFLOW CFD solver was based on delayed detached eddy simulations (DDES). Before initiating the pitch-up motion, a well-resolved static solution is established. The pitch rate for the ramp-up motion is meticulously set, corresponding to a temporal resolution of 35,000 time

steps. This temporal resolution, denoted as a non-dimensional time step $\Delta t^* = 0.000271$, is validated by Batther and Lee [4] for ensuring numerical accuracy and effectively capturing complex flow features associated with dynamic stall. Additionally, 30 sub-iterations are incorporated within each time step to ensure robust numerical convergence. To enhance the precision of the simulations, the TLNS3D dissipation scheme is used, applying second and fourth-order dissipation to the right-hand and left-hand side terms, respectively, complemented by smoothing techniques. This configuration of setup variables and temporal resolutions has been proven effective in capturing detailed aerodynamic behaviors in prior studies [58, 85, 86, 88]. Acknowledging the limitations in fully turbulent flow computations, especially near the stagnation point where transitional flow phenomena are critical, the recommendation by Rumsey [77] are adopted to include transitional modeling. This method has shown to yield more accurate predictions of dynamic stall characteristics, as demonstrated by Jain et al. [37]. In the simulations, the correlation-based two-equation Langtry-Menter transition model [50], which builds on the 2003 version of Menter's shear stress transport (SST) model is employed. This model provides enhanced capabilities and corrections essential for accurately capturing the transition from laminar to turbulent flow, crucial for detailed analysis of dynamic stall phenomena.

4.2.3. Surface Impact-Induced Roughness Method. Particle impact interactions can be precisely modeled using ParticleTSim, a physics-based simulation tool developed by Lawrence Livermore National Laboratory (LLNL). This code is specially crafted for simulating particle transport in complex hydrodynamic environments, focusing on interactions with surfaces. ParticleTSim excels in providing detailed statistics on particle trajectories, temperature changes, impact locations, and angles of incidence. It is capable of handling extensive particle transport scenarios, utilizing a prescribed background flowfield as input. In this study, particle sizes typical of desert and arid regions globally are referenced [2, 73]. Additionally, the code generates strike maps that offer vital insights into particle behavior and distribution upon contact with objects and surfaces. ParticleTSim is notably flexible and can be integrated with other high-fidelity simulation tools. In my research, ParticleTSim is coupled with OVERFLOW 2.3 [72] to assess the effects of surface impacts. The methodology employs one-way coupling, whereby the flow results from OVERFLOW are used to inform ParticleTSim, but the particle trajectories or statistics generated by ParticleTSim do not

influence the flow fields modeled in OVERFLOW. Another fundamental approximation in this approach is the use of quasi-steady flow fields to inform ParticleTSim during dynamic airfoil motions. This involves extracting flow field data at a specific angle of attack (AoA) and applying it within ParticleTSim simulations. Despite the dynamic motion of the airfoil, it is assumed that the airfoil remains stationary throughout the particle trajectories and their impacts on the surface. While this assumption simplifies the interaction, it is essential for enabling effective integration between OVERFLOW and ParticleTSim. This simplification is critical in allowing for efficient exploration of how particles influence surface roughness development and, consequently, how this roughness impacts dynamic stall. Ultimately, this approach facilitates a more streamlined examination of these crucial factors in the study.

The roughness elements arising from particle impact-induced surface roughness are characterized, as simulated by ParticleTSim. Specifically, an equivalent sand grain roughness parameter, represented as k_r, is calculated. This roughness parameter is expressed in terms of the chord length, denoted as k_r/c, where c is the chord length. The roughness height parameter is then incorporated as a boundary condition along the chordwise direction in the OVERFLOW solver, enabling the simulation of the aerodynamic impact of surface roughness with precision. The detailed methodology for calculating this roughness height parameter, including its theoretical basis and implementation specifics, will be discussed in Section 4.4.1.

4.3. Numerical Results and Discussion

This section first shows the details and setup for the airfoil geometry and baseline test case. The description of the roughness height calculation and strike maps are provided. The analysis of the aerodynamic loading for the baseline case, full surface roughness cases, and partial surface roughness cases are presented and analyzed. Then the reasoning behind the dynamic stall development stages and behaviors, and flow physics are discussed. This includes contours of the vorticity magnitude and kinetic energy during the critical stages of the dynamic stall development.

4.4. Airfoil Geometry and Test Case

A NACA 0012 airfoil is used for the baseline airfoil, which undergoes a pitching motion at a freestream Mach number of 0.1 and a Reynolds number of 200,000. This airfoil has a 1m chord

length and a blunt trailing edge. The ramp-up motion, represented by the pitch rate, $\dot{\alpha}$, is provided in Eq. (4.1):

$$\dot{\alpha}(t^*) = \psi_o^+(1 - e^{-4.6t^*/t_o}) \tag{4.1}$$

where $t^* = tU_\infty/c$ denotes the non-dimensional time, t_o=0.5, and ψ_o^+ is 0.05. This allows the pitch rate to reach 99% of its asymptotic value, ψ_o^*, fairly quickly ($t_o = 0.5$). Figure 4.2 shows the AoA or α, and non-dimensional pitch rate, $\dot{\alpha}$, as a function of the non-dimensional time.

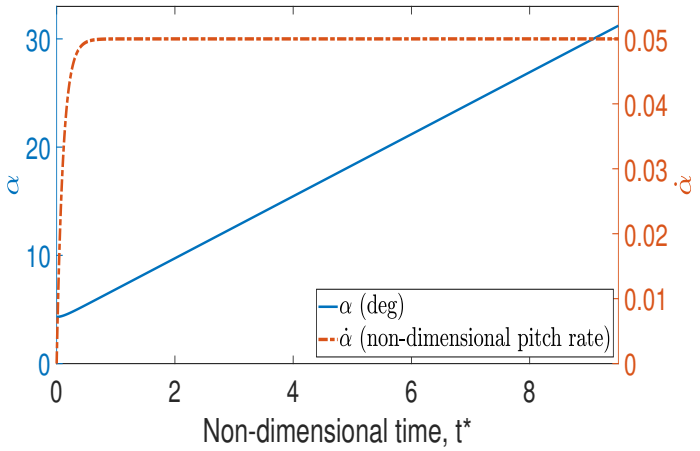

FIGURE 4.2. Prescribed pitching motion

4.4.1. Roughness Height. In this study, the maximum non-dimensional roughness height $\epsilon^+ = \epsilon u^*/\nu$ is chosen to be 70 at the location of $x/c = 0.11$ where the dynamic stall initiates. The variable ϵ is the roughness height, u^* is the friction velocity, and ν is the kinematic viscosity. Regarding the flow characteristics associated with surface roughness, there are three distinct regions: the hydraulically smooth region, the transitional roughness region, and the fully rough region. The chosen height corresponds to the upper bound of the transitional roughness region. It is found that the roughness height is determined to be $\epsilon = 7.9 \times 10^{-3}$ m, which is implemented as the k_r in this study. Additionally, the effects of other roughness height values, shown in Table 4.1, are also investigated. These other values, which are approximately 50% and 20% of the maximum calculated height value, are used to observe the roughness trends for this study.

TABLE 4.1. The equivalent sand grain roughness heights used in the study

ϵ^+	$\epsilon(m)$
70	7.9×10^{-3}
32	3.6×10^{-3}
14	1.5×10^{-3}

4.4.2. Strike Maps. Figure 4.3 displays strike maps generated by ParticleTSim [80], which illustrate particle interactions at both the initial and final AoAs during the simulated dynamic stall event. The lowest AoA is set at 4.48°, while the highest AoA reaches 26.94°. These AoAs are specifically chosen to cover the full range of particle strikes observed during the ramp-up motion of the dynamic stall. The strike maps detail the impact regions, highlighting areas affected by particle impacts. It is crucial to note that the particles are released into the upstream velocity flowfield and are distributed randomly across the airfoil's projected surface area. This strike map is only for one body length (chord length) travel distance. At AoA of 26.94°, the lower surface of the NACA 0012 airfoil registers a more significant impact from incoming particles compared to AoA of 4.48°. The ParticleTSim strike map results indicate that particle impacts reach the location of x/c=0.19 on the upper surface (suction side), as shown in Figure 4.3(a). In contrast, particle impacts cover the entire lower surface (pressure side) of the airfoil, as shown in Figure 4.3(b). These observations allow us to define the particle strike region to be from x/c=0.19 on the upper surface (suction side) to x/c=1.0 on the lower surface (pressure side) during the ramp-up phase of dynamic stall motion. Subsequent sections will provide a comprehensive analysis comparing the aerodynamic loading characteristics and flow physics arising from complete surface roughness versus partial surface roughness, specifically impacted by particles. This will also include a detailed examination of the effects of such roughness on dynamic stall performance and behavior.

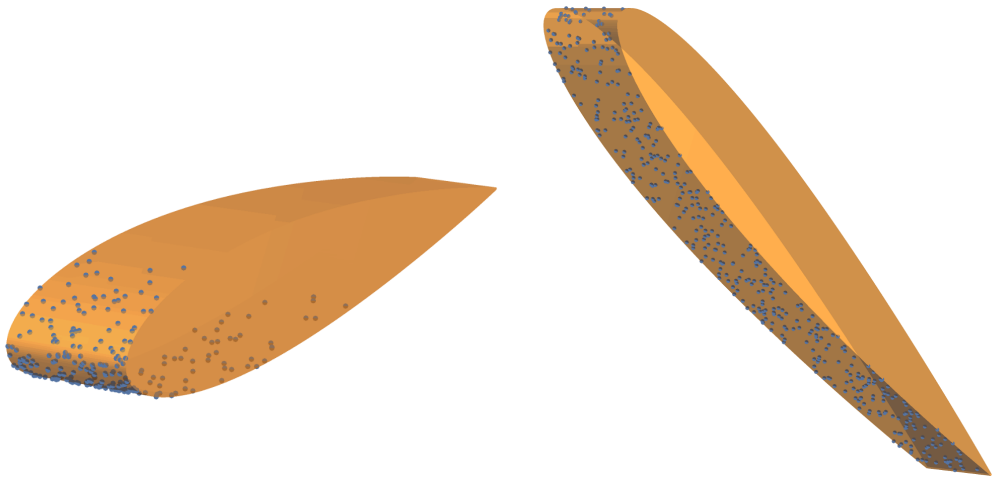

(a) (b)

FIGURE 4.3. ParticleTSim [80] strike maps of the particle interactions on the airfoil occurring at (a) 4.48°, and (b) 26.94°. NACA 0012, M = 0.1, Re = 2×10^5, and $\dot{\alpha}(t^*) = \psi_o^+(1 - e^{-4.6t^*/t_o})$.

4.4.3. Analysis of the Aerodynamic Loading.

4.4.3.1. *Full and Partial Surface Roughness.* Figure 4.4 provides a comparative analysis of the coefficients of lift (C_l), drag (C_d), and moment (C_m) obtained from simulations of the baseline smooth airfoil versus airfoils with varying roughness factors, specifically with k_r/c values of 1.5×10^{-3}, 3.6×10^{-3}, and 7.9×10^{-3}. These roughness factors are applied across the entire surface of the airfoil, from the trailing edge to the leading edge on the both surfaces. The selected upper and lower bounds for the roughness scaling factors enable a detailed examination of the impact of increasing roughness height factors. The results for airfoils with full surface roughness demonstrate a consistent decrease in lift as the roughness values increase, corroborating findings from prior research [48, 106, 107]. Furthermore, there is a notable reduction in the magnitudes of C_l, C_d, and C_m, accompanied by a shift in the stall AoAs to earlier values as the roughness factor increases. This trend indicates that the application of full surface roughness significantly alters the dynamic stall development process.

The aerodynamic loading results for both full and partial surface roughness are examined and compared. The term 'partial' specifically refers to the particle strike region ranging from a location of x/c=0.19 on the upper surface to x/c=1.0 on the lower surface, as detailed in subsection 4.4.2. The effects of full and partial surface roughness on the aerodynamic coefficients are depicted in

Figs. 4.5, 4.6, and 4.7. In Fig. 4.5, it is observed that the behaviors of the coefficients of lift (C_l), drag (C_d), and moment (C_m) for a roughness value of $k_r/c = 1.5 \times 10^{-3}$ are very similar to those for the same value applied over the full surface. This is the lowest roughness height examined in this study, indicating that at lower roughness levels, the distinction between full and partial surface roughness is minimal. However, as the roughness value increases to $k_r/c = 3.6 \times 10^{-3}$ and $k_r/c = 7.9 \times 10^{-3}$, noticeable differences emerge between the full and partial roughness scenarios. With these higher roughness values, the discrepancies in peak magnitudes of C_l, C_d, and C_m between the full and partial surface roughness cases become more pronounced. Additionally, the difference in stall AoAs between the partial and full roughness cases widens as the roughness value increases. Overall, the analysis reveals that the peak magnitudes of C_l, C_d, and C_m decrease more substantially in full surface roughness cases compared to partial surface roughness scenarios. Moreover, the stall AoAs occur earlier in the full surface roughness cases as the roughness height increases, whereas the stall AoAs for the partial surface roughness cases remain relatively consistent with the baseline scenario. These results suggest that stall AoAs and the reduction in aerodynamic performance are sensitive to the surface roughness impact region.

4.4.3.2. *Viscous and Pressure Drag.* Figure 4.8 provides a detailed comparison between pressure and viscous drags for the full and partial surface roughness cases. Pressure drag is detailed in Fig 4.8(a), while viscous drag is explored in Fig 4.8(b). As shown in Fig. 4.8(a), pressure drag, primarily due to flow separation, contributes significantly more to the overall drag, often by three orders of magnitude, and closely mirrors the total drag trends discussed in the previous subsection. Similarly, the full roughness cases consistently show slightly lower values of drag occuring at earlier AoAs compared to their partial counterparts. Figure 4.8(b) demonstrates that viscous drag (C_d) also increases with roughness. Notably, the $k_r/c = 7.9 \times 10^{-3}$ (full) scenario exhibits the highest viscous drag among all the cases studied. This is followed, in descending order of drag magnitude, by $k_r/c = 7.9 \times 10^{-3}$ (partial), $k_r/c = 3.6 \times 10^{-3}$ (full), $k_r/c = 3.6 \times 10^{-3}$ (partial), $k_r/c = 1.5 \times 10^{-3}$ (full), $k_r/c = 1.5 \times 10^{-3}$ (partial), and finally the baseline case. This pattern underscores the direct relationship between increased surface roughness and heightened viscous drag, particularly evident at higher roughness scales. These results indicate that while both types of drag are affected by surface roughness, the increase in roughness height amplifies their impact.

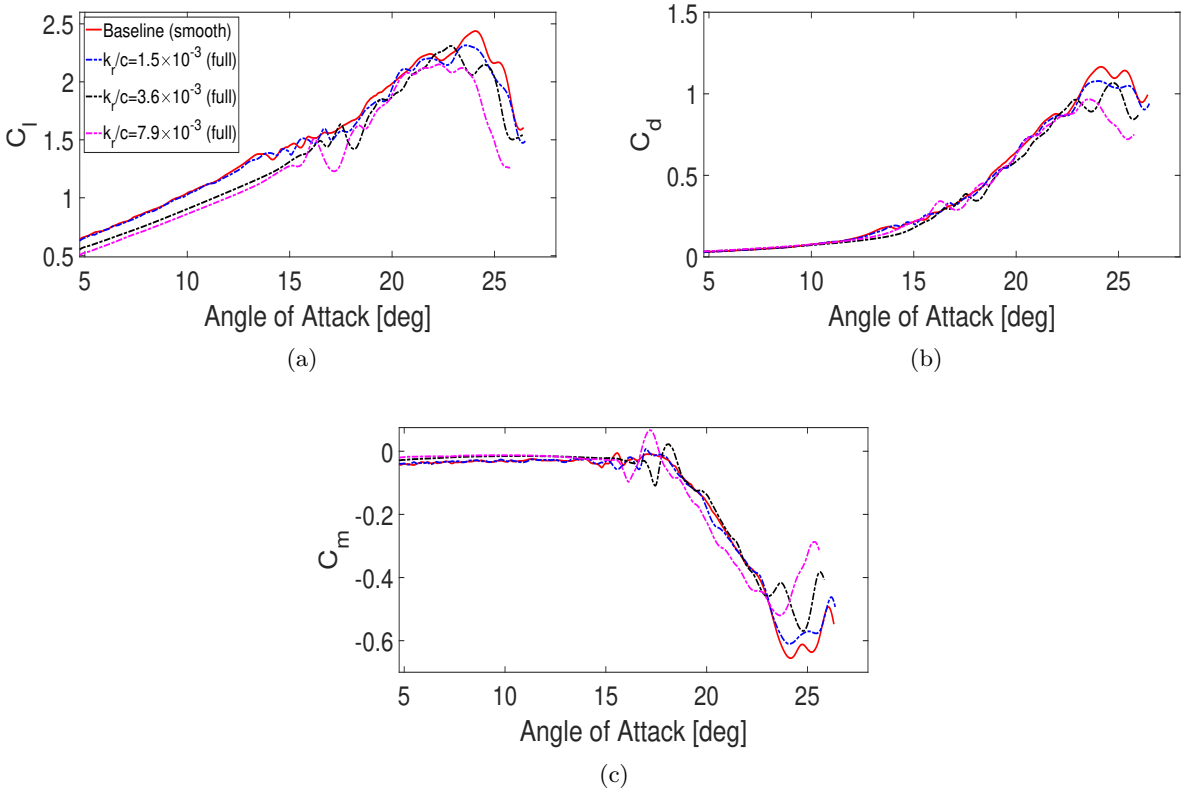

FIGURE 4.4. Comparison of the C_l, C_d, and C_m behaviors for baseline case and the full surface roughness cases.

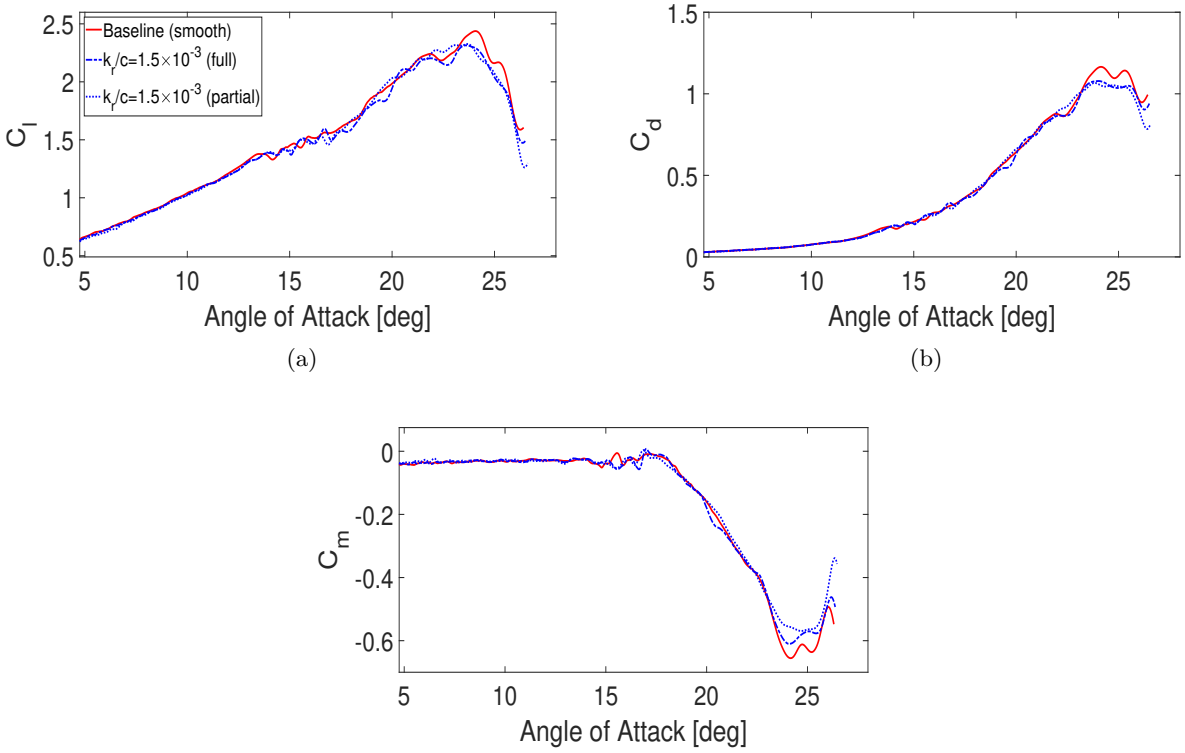

FIGURE 4.5. Comparison of the C_l, C_d, and C_m behaviors for baseline case and the $k_r/c = 1.5 \times 10^{-3}$ full and partial surface roughness cases.

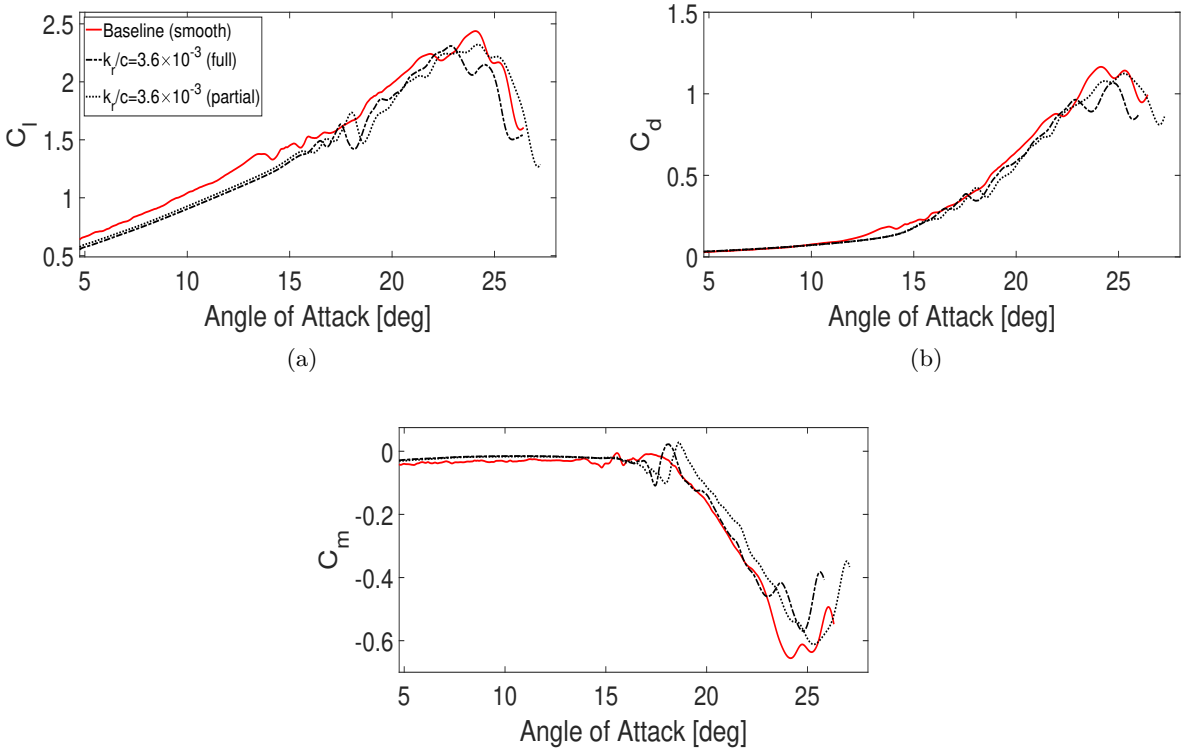

FIGURE 4.6. Comparison of the C_l, C_d, and C_m behaviors for baseline case and the $k_r/c = 3.6 \times 10^{-3}$ full and partial surface roughness cases.

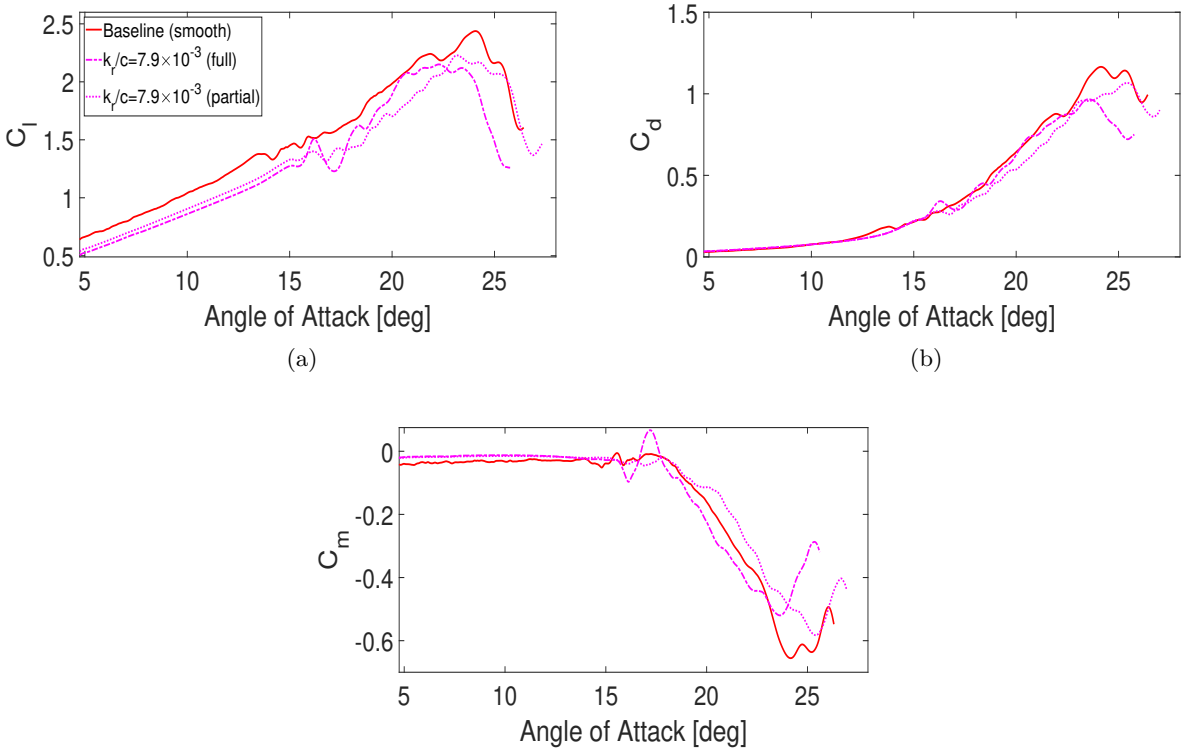

FIGURE 4.7. Comparison of the C_l, C_d, and C_m behaviors for baseline case and the $k_r/c = 7.9 \times 10^{-3}$ full and partial surface roughness cases.

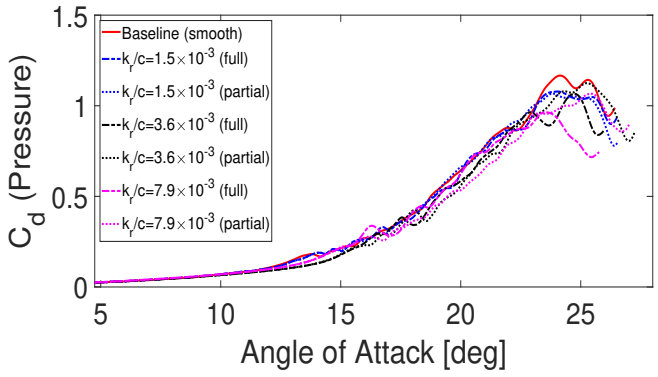

(a)

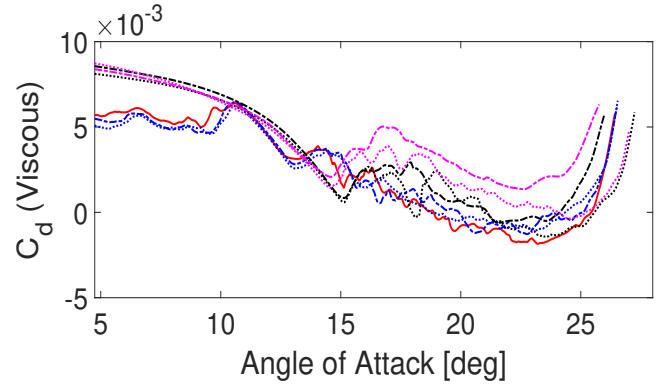

(b)

FIGURE 4.8. Comparison of the pressure and viscous C_d for baseline case as well as full and partial surface roughness cases.

4.4.4. Dynamic Stall Development Stages. As stated and explained in Sec. 3.3.3, dynamic stall process is characterized by several distinct stages, each marking critical events in its progression, which will be studied in this subsection. It is important to emphasize again that, due to the highly transient nature of dynamic stall, particularly at elevated AoAs, the parameters of interest discussed in this subsection are spanwise averaged. This approach is necessitated by the significant fluctuations inherent in dynamic stall behavior, which can obscure underlying patterns if only analyzed at a single spanwise location. Spanwise averaging would yield a more accurate representation of the complex and highly variable flow patterns associated with dynamic stall.

Figures 4.9 and 4.10 present the spanwise-averaged surface pressure and skin friction coefficients for the baseline NACA 0012 airfoil case (smooth) and the full and partial surface roughness cases, from an initial stage ($\alpha = 16.1°$) where the LSB is developing at the leading edge, to a stage ($\alpha = 24.2°$) where the DSV starts to detach from the surface. For the baseline case, the suction collapses at $\alpha = 18.0°$ where the LSB size increases with a noticeable peak at around $x/c = 0.25$ as seen in Fig. 4.9(a). In the $k_r/c = 1.5 \times 10^{-3}$ full and partial surface roughness cases, the suction also collapses near $\alpha = 18.0°$ with a noticeable peak at around $x/c = 0.3$ as seen in Fig. 4.9(b) and (c). For the $k_r/c = 3.6 \times 10^{-3}$ and $k_r/c = 7.9 \times 10^{-3}$ full surface roughness cases, the suction collapse associated with laminar separation bubble (LSB) is not clearly visible. Furthermore, it can be observed that the progression of the dynamic stall development stages for $k_r/c = 3.6 \times 10^{-3}$ and $k_r/c = 7.9 \times 10^{-3}$ full surface roughness cases occur much quicker, with $k_r/c = 7.9 \times 10^{-3}$ case being the quickest. At the same $\alpha = 18.0°$, the $k_r/c = 3.6 \times 10^{-3}$ case reaches its C_p peak at a around $x/c = 0.35$ when the $k_r/c = 7.9 \times 10^{-3}$ case reaches its C_p peak at a around $x/c = 0.4$. The dynamic stall development behavior for the $k_r/c = 3.6 \times 10^{-3}$ and $k_r/c = 7.9 \times 10^{-3}$ partial roughness cases are relatively similar with peak magnitudes lower for the $k_r/c = 7.9 \times 10^{-3}$ case. Overall, the magnitudes and span widths of the C_p curves are larger for the baseline and the partial surface roughness cases compared to the full surface roughness cases. The trend behavior indicates that the C_p curve magnitudes are greatly weakened when the full surface roughness is applied for the high roughness height values. For the C_f plots in Fig. 4.10(c), (e), and (g), the partial surface roughness cases exhibit a greater fluctuation for their C_f values due to flow reattachment and secondary LSB before bursting. The amplitude of this fluctuation increases as the roughness height

increases. The full surface roughness cases also exhibit flow reattachment and secondary LSB, but with much milder strength.

Figure 4.11 and 4.12 show the surface pressure and skin friction contours, illustrating the complete formation of the dynamic stall flow topology. These contour plots depict the development of the entire dynamic stall process on the airfoil surface across the full range of AoA. Moreover, these pressure and skin friction contour plots provide further support for the spanwise-averaged C_p and C_f plots for the selected distinct angles shown in Figs. 4.9, and 4.10. The overall trends for the smooth baseline case and the low roughness height of $k_r/c = 1.5 \times 10^{-3}$ for full and partial surface roughness cases are similar. For the baseline case and the $k_r/c = 1.5 \times 10^{-3}$ full and partial surface roughness cases, at lower AoAs, the instability waves are visible in the C_f contours starting in the middle x/c locations, indicating the flow transition. The transition location moves upstream toward the leading edge as AoA increases. It is seen that the trailing-edge separation advances towards the leading edge, encountering the LSB near the leading edge at around $\alpha = 13°$. Following this encounter, the LSB eventually bursts around $\alpha = 18°$ for the baseline and the $k_r/c = 1.5 \times 10^{-3}$ full and partial surface roughness cases. After the bursting of the LSB, the DSV begins to form and moves toward the trailing edge. However for the $k_r/c = 3.6 \times 10^{-3}$ and $k_r/c = 7.9 \times 10^{-3}$ full and partial surface roughness cases, there is no indication of instability and transition behavior in the low AoA and x/c regions. Instead, the strong flow separation behavior starts directly near $\alpha = 13°$ and $\alpha = 14°$ for these cases. Before DSV develops, the higher skin friction is observed with higher roughness height. There is a greater region of near zero C_f on the surface for the $k_r/c = 3.6 \times 10^{-3}$ and $k_r/c = 7.9 \times 10^{-3}$ cases at low AoAs in comparison to the baseline and $k_r/c = 1.5 \times 10^{-3}$ cases. For higher roughness cases, a compact LSB region is not clearly seen. Instead, an elongated flow separation region with mild strength is observed. The $k_r/c = 3.6 \times 10^{-3}$ and $k_r/c = 7.9 \times 10^{-3}$ partial surface roughness cases display a larger flow separation region corresponding to the DSV development than the full surface roughness cases. Additionally, there are small gaps of positive C_f values mixed in between the DSV flow separation and development in the partial surface roughness cases, indicating flow reattachment. The secondary shear layer separation also slightly intensifies for the partial surface roughness cases in comparison to the full surface roughness cases.

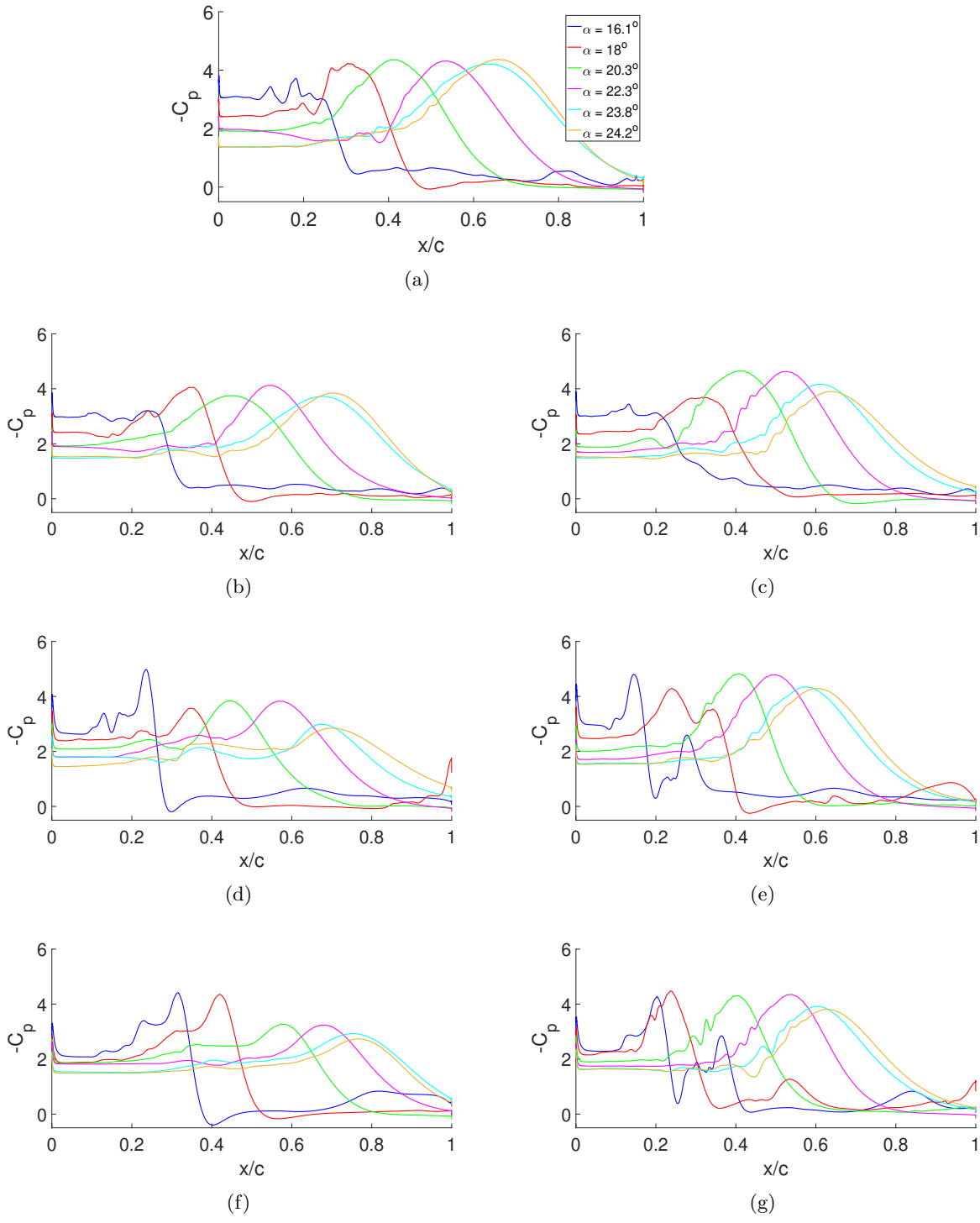

FIGURE 4.9. Spanwise-averaged C_p for (a) baseline, and $k_r/c =$: (b) 1.5×10^{-3} (full), (c) 1.5×10^{-3} (partial), (d) 3.6×10^{-3} (full), (e) 3.6×10^{-3} (partial), (f) 7.9×10^{-3} (full), and (g) 7.9×10^{-3} (partial).

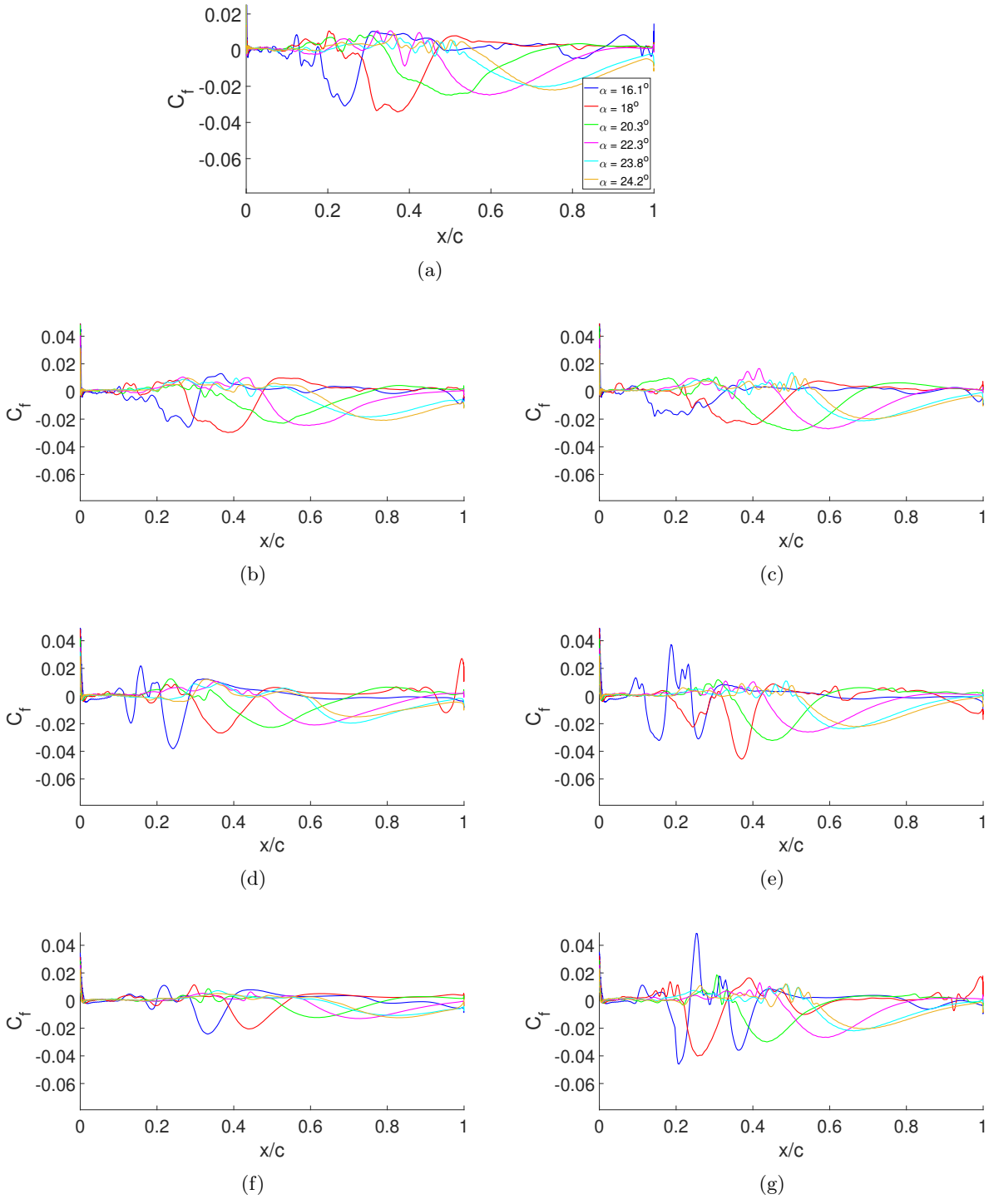

FIGURE 4.10. Spanwise-averaged C_f for (a) baseline, and $k_r/c =$: (b) 1.5×10^{-3} (full), (c) 1.5×10^{-3} (partial), (d) 3.6×10^{-3} (full), (e) 3.6×10^{-3} (partial), (f) 7.9×10^{-3} (full), and (g) 7.9×10^{-3} (partial).

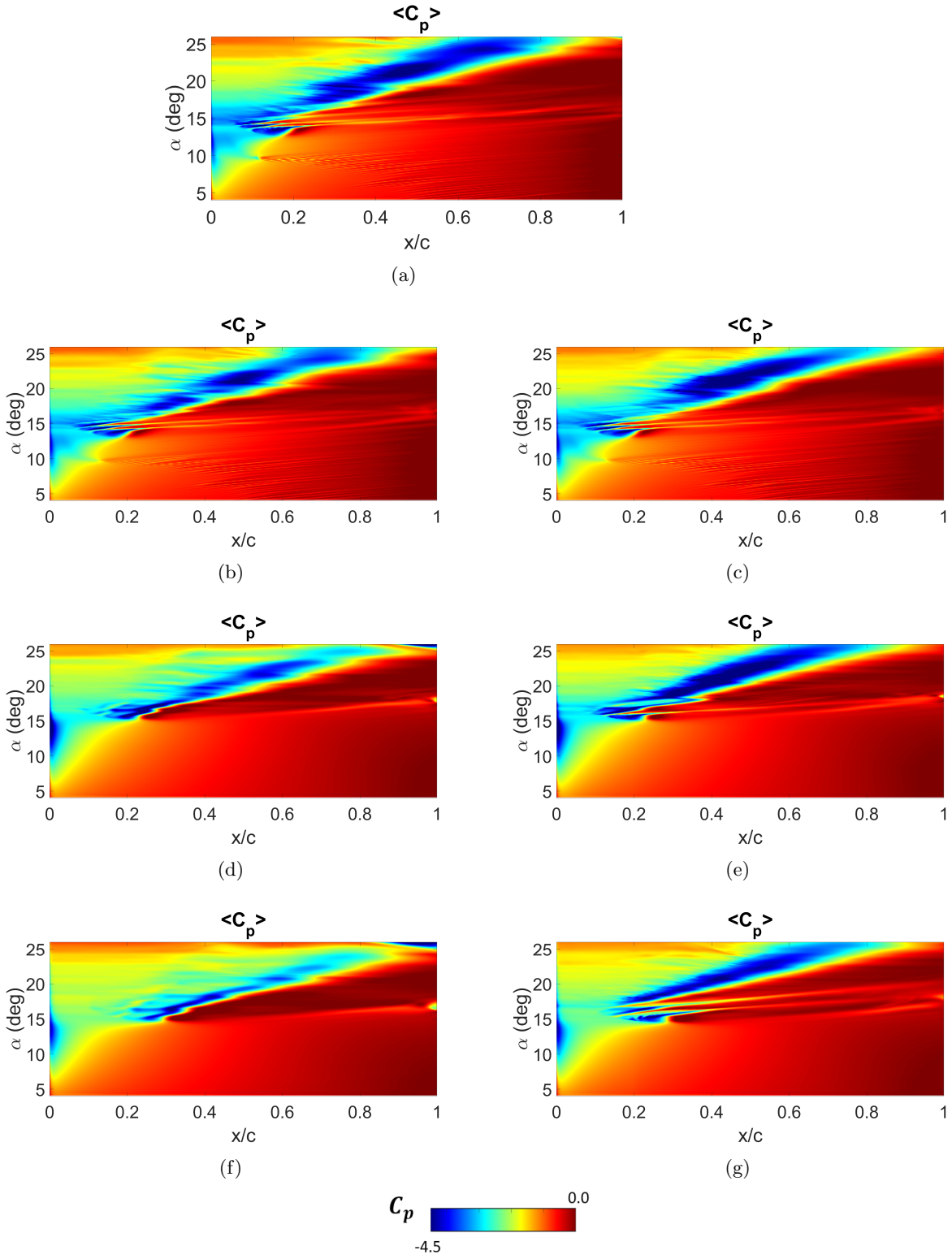

FIGURE 4.11. Spanwise-averaged C_p contours: (a) baseline, and $k_r/c =$: (b) 1.5×10^{-3} (full), (c) 1.5×10^{-3} (partial), (d) 3.6×10^{-3} (full), (e) 3.6×10^{-3} (partial), (f) 7.9×10^{-3} (full), and (g) 7.9×10^{-3} (partial).

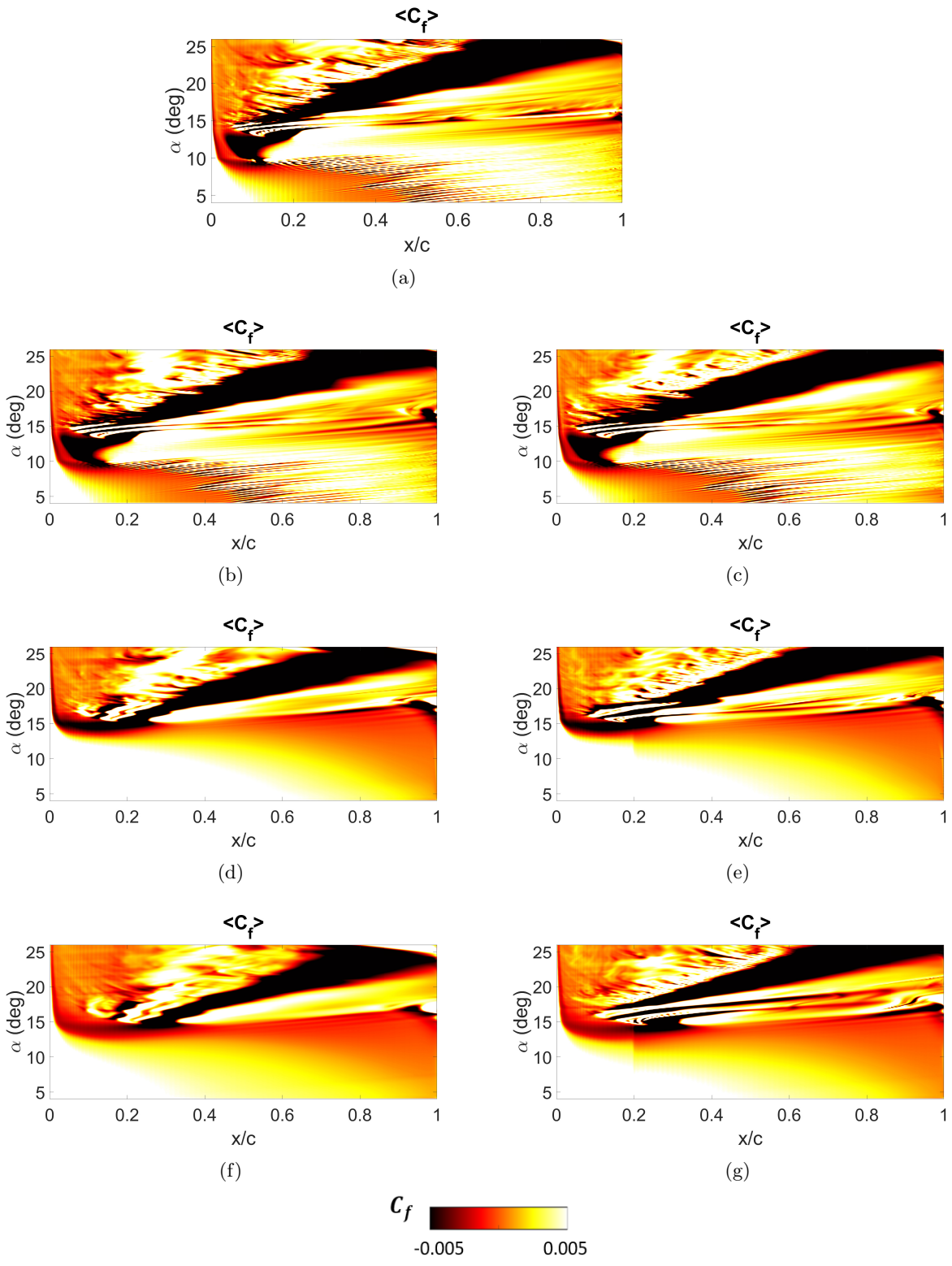

FIGURE 4.12. Spanwise-averaged C_f contours: (a) baseline, and $k_r/c =$: (b) 1.5×10^{-3} (full), (c) 1.5×10^{-3} (partial), (d) 3.6×10^{-3} (full), (e) 3.6×10^{-3} (partial), (f) 7.9×10^{-3} (full), and (g) 7.9×10^{-3} (partial).

4.4.5. Flow Physics and Energy. The behavior observed during the dynamic stall development process can be further elucidated by delving into the underlying flow physics and kinetic energy dynamics at critical stages of the stall cycle.

4.4.5.1. *Vorticity Magnitude.* Figure 4.13 illustrates the vorticity magnitude at various AoAs during the ramp-up phase of dynamic stall for a smooth baseline airfoil. These stages include $\alpha = 16.1°$, $18.0°$, $20.3°$, $22.3°$, $23.8°$, and $24.2°$. At the initial stage ($\alpha = 16.1°$), there is already observable instability within the boundary layer, with leading-edge vortices beginning to develop. This early phase marks the start of significant vorticity generation at the leading edge, indicative of the formation and subsequent bursting of the leading-edge LSB. As the AoA increases, the boundary layer thickness grows, and flow separation near the trailing edge begins to form, leading to the development of a trailing-edge vortex. This process results in increased vorticity production across the airfoil. By $\alpha = 18.0°$, the LSB has burst due to an adverse pressure gradient, intensifying the reverse flow under DSV. This transition is accompanied by a marked increase in vorticity magnitude, signaling profound changes in the flow structure around the airfoil. At $\alpha = 20.3°$, a large DSV forms near the leading edge, heralding the airfoil's approach to the stall condition. This DSV continues to propagate downstream as the AoA increases, impacting the aerodynamic forces experienced by the airfoil. At $\alpha = 22.3°$ and subsequent higher AoAs, the shear layer vortices become more pronounced and visible. The process culminates in the onset of stall around $\alpha = 23.8°$, with the DSV being shed from the airfoil surface by $\alpha = 24.2°$. This shedding marks a critical transition into full stall and complete flow separation, with the DSV moving downstream. Throughout all stages, especially at the higher AoAs, the baseline smooth airfoil does not exhibit behavior associated with flow detachment in the near leading-edge region. The progression and characterization of these dynamic stall phenomena align well with findings reported in references such as Refs. [4, 88], providing a detailed understanding of the vorticity dynamics and their implications on stall development and aerodynamic performance.

Figures 4.14, 4.15, 4.16, 4.17, 4.18, and 4.19 show the vorticity magnitude during various stages ($\alpha = 16.1°$, $18.0°$, $20.3°$, $22.3°$, $23.8°$, and $24.2°$) for the full and partial surface roughness cases during the ramp-up pitching motion. These roughness height values include $k_r/c = 1.5 \times 10^{-3}$ (full) and (partial), $k_r/c = 3.6 \times 10^{-3}$ (full) and (partial), and $k_r/c = 7.9 \times 10^{-3}$ (full) and (partial). The vorticity magnitudes across all AoAs are very similar for $k_r/c = 1.5 \times 10^{-3}$ (full) and

(partial). This is because, as explained previously in Fig. 4.5 in Sec. 4.4.3, this lowest roughness height value has very similar aerodynamic loading characteristics throughout the whole dynamic stall process. However, noticeable differences are beginning to show between the full and partial surface roughness case results for $k_r/c = 3.6 \times 10^{-3}$ and $k_r/c = 7.9 \times 10^{-3}$. At lower AoAs, the vorticity magnitudes are still quite similar between the full and partial surface roughness cases. But at the higher AoAs, the vorticity magnitudes occupy a greater space and detach from the surface for the full surface roughness cases. The results also show that in comparison, the dynamic stall motion for full surface roughness is progressing much faster than partial surface roughness. Notably, at $\alpha = 22.3°$, $23.8°$, and $24.2°$, for $k_r/c = 7.9 \times 10^{-3}$, there are fewer of the smaller vortices observed at the leading edge at the higher AoAs for the full surface roughness case compared to the partial surface roughness cases. At $\alpha = 23.8°$ and $24.2°$, note the great differences in the vorticity magnitude size and development between the full and partial surface roughness cases. The lack of smaller vortices at the leading edge is also the most pronounced between the full and partial surface roughness cases of all the AoA cases shown. Another important observation is to recognize that the higher roughness values for full surface roughness cause more vortical disturbances and demonstrate an inclination to experience the stall behavior at an earlier AoA. The results presented in these vorticity magnitude contour plots further justify the behavior presented in the aerodynamic loading plots in subsection 4.4.3.

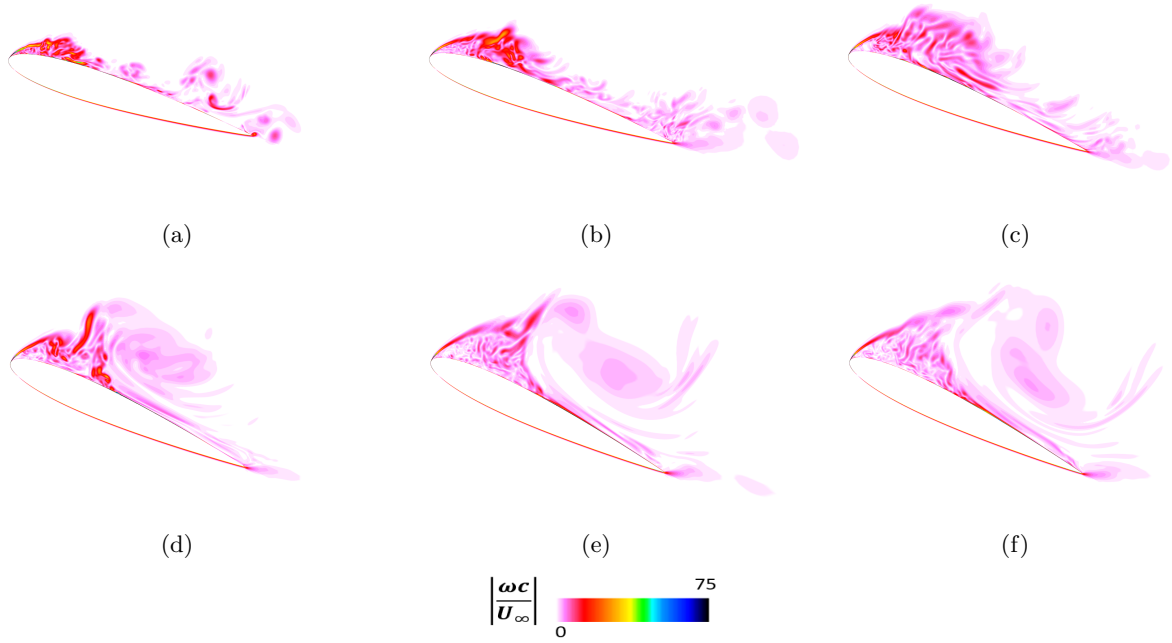

FIGURE 4.13. Instantaneous (midplane) contours of vorticity magnitude for the baseline (smooth) case at α: (a) 16.1°, (b) 18.0°, (c) 20.3°, (d) 22.3°, (e) 23.8°, and (f) 24.2°.

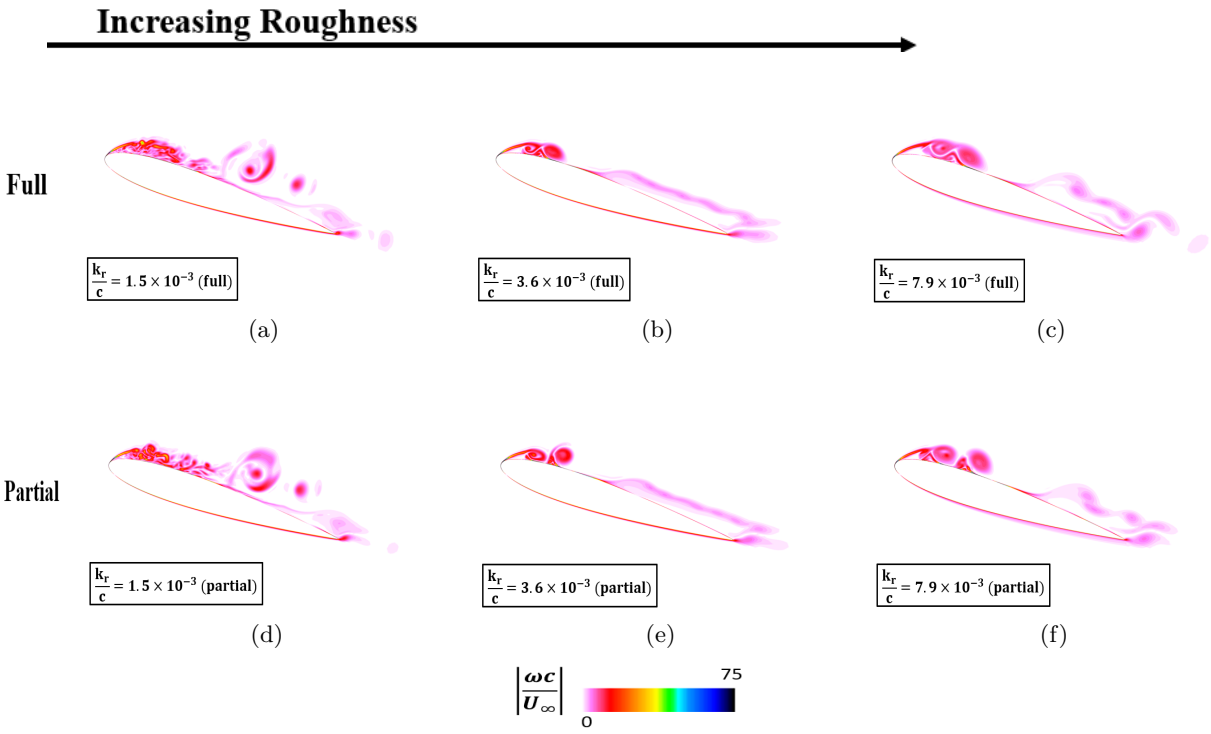

FIGURE 4.14. Instantaneous (midplane) contours of vorticity magnitude at α=16.1°.

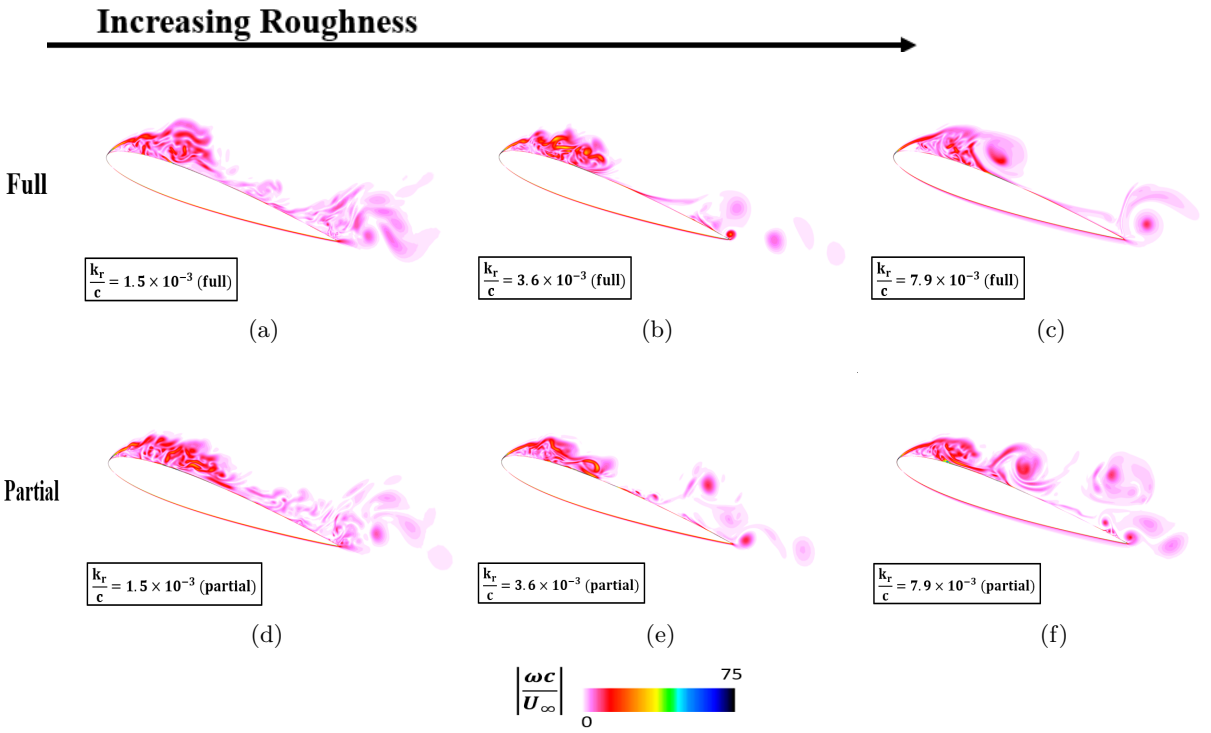

FIGURE 4.15. Instantaneous (midplane) contours of vorticity magnitude at α=18.0°.

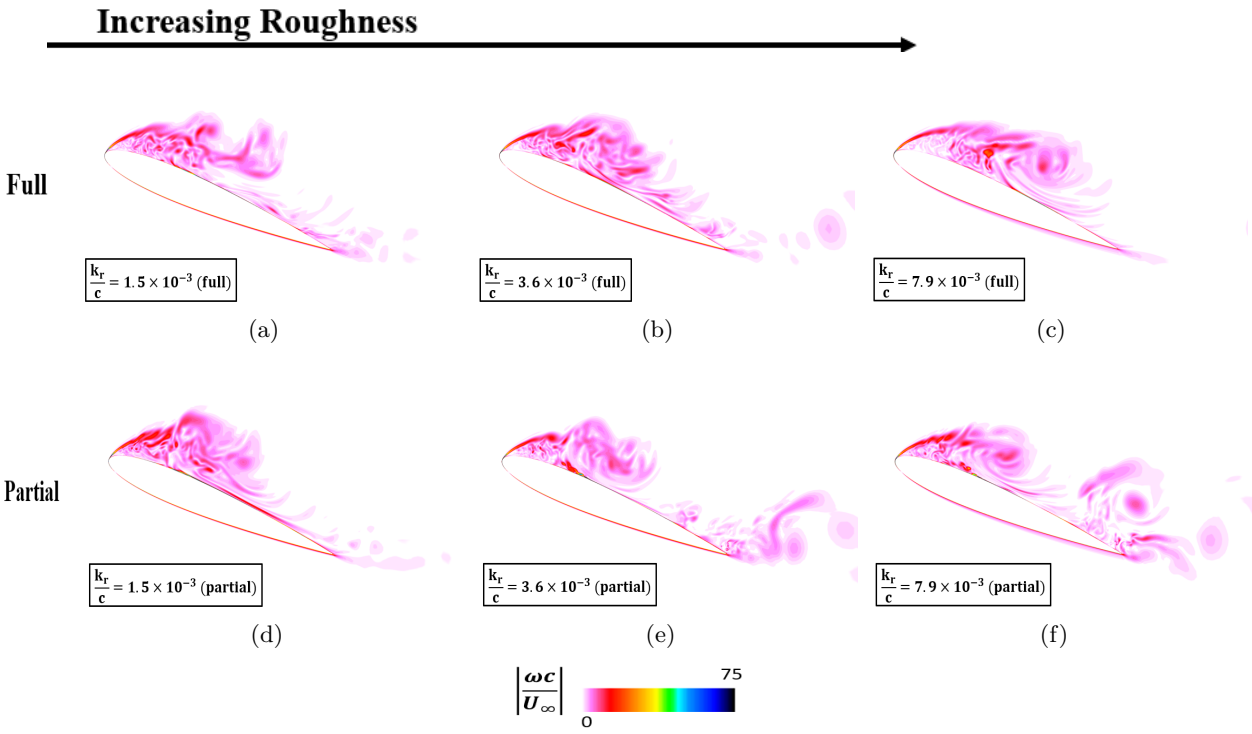

FIGURE 4.16. Instantaneous (midplane) contours of vorticity magnitude at α=20.3°.

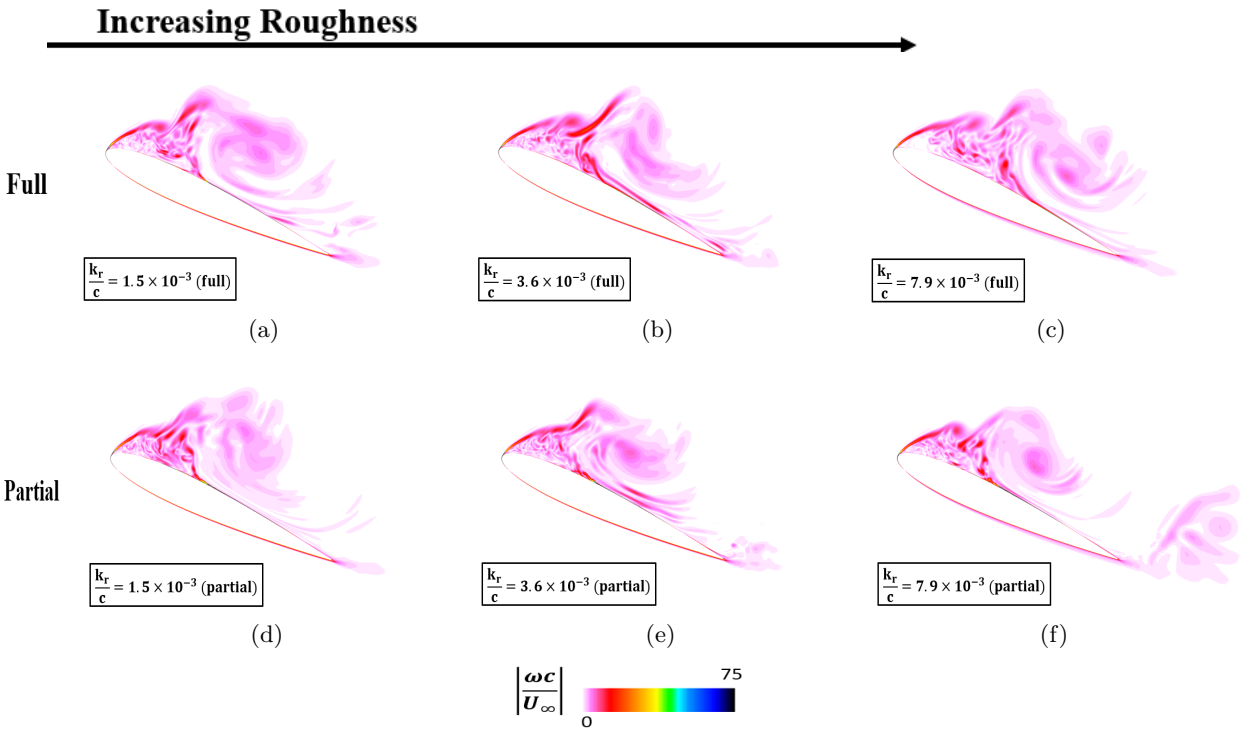

FIGURE 4.17. Instantaneous (midplane) contours of vorticity magnitude at α=22.3°.

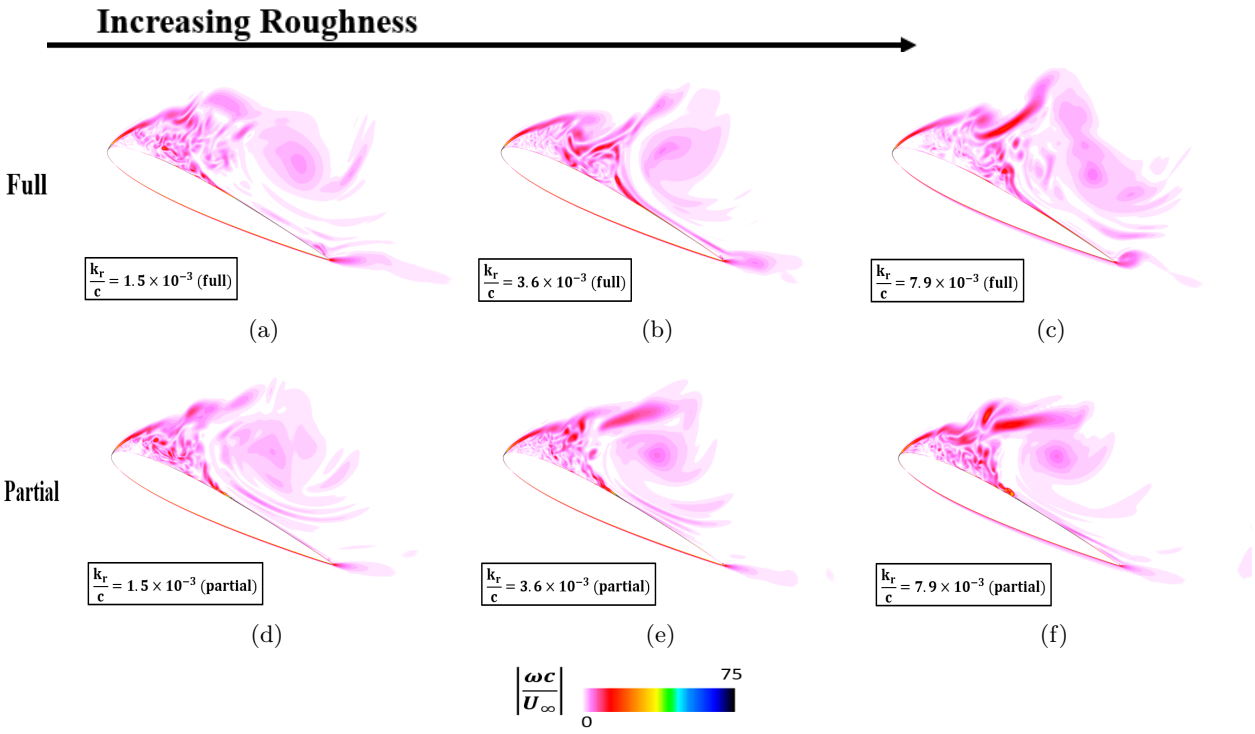

FIGURE 4.18. Instantaneous (midplane) contours of vorticity magnitude at α=23.8°.

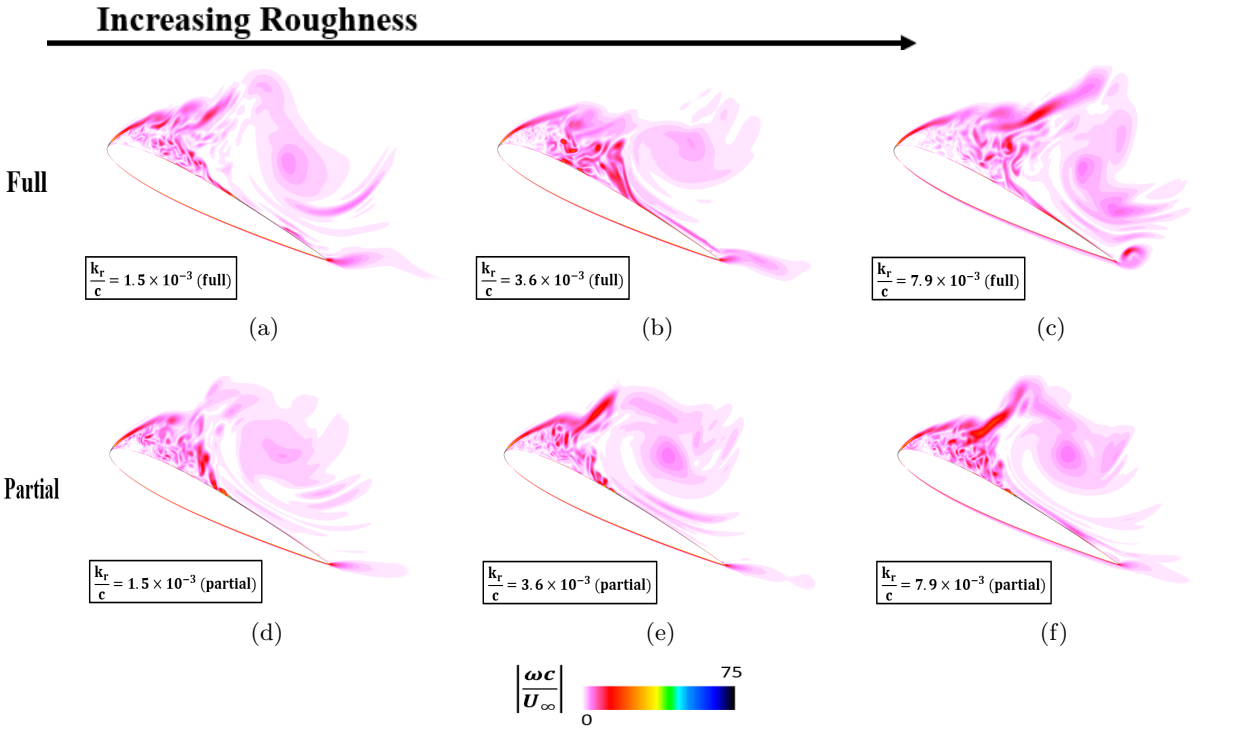

FIGURE 4.19. Instantaneous (midplane) contours of vorticity magnitude at α=24.2°.

4.4.5.2. *Kinetic Energy.* Figure 4.20 illustrates kinetic energy contours for a baseline (smooth) NACA 0012 airfoil at various AoAs during a dynamic stall event. The color bar below represents the non-dimensional energy, where the kinetic energy $KE = \frac{1}{2}(u^2 + v^2 + w^2)$ is nondimensionalized by the speed of sound, a_∞. Each subfigure (a) through (f) in Fig 4.20 represents the airfoil's flow field at specific AoAs, providing a visual progression of the kinetic energy distribution as dynamic stall develops. At $\alpha = 16.1°$, the formation of a leading-edge vortex (LEV) is observed. This vortex is characterized by a concentration of high kinetic energy near the leading edge, indicating the beginning of flow separation and vortex formation. At $\alpha = 18.0°$, the kinetic energy near the leading edge intensifies, and the LEV becomes more pronounced. This stage typically signifies the escalation of flow separation and the imminent bursting of the leading-edge LSB. At $\alpha = 20.3°$, the flow separation continues to advance, and the LEV grows larger and begins to propagate downstream. The increased kinetic energy in the aft region of the airfoil suggests the development of trailing-edge vortices as well. At $\alpha = 22.3°$, the vortex dynamics become more complex with a significant increase in kinetic energy across the airfoil. This stage often marks a critical point in the dynamic stall cycle, where the LEV is fully developed, and flow separation is extensive. At $\alpha = 23.8.1°$ and $\alpha = 24.2°$, these stages show the airfoil as it reaches and surpasses the critical angle for stall. The DSV is shedding from the airfoil surface, leading to a massive redistribution of kinetic energy. This energy is not only concentrated around the leading edge but also in the wake of the airfoil, indicating full stall and the consequent breakdown of flow structures. Each subfigure effectively captures the transient behavior of kinetic energy associated with the dynamic stall phenomenon. The visual progression from (a) to (f) clearly illustrates how the kinetic energy shifts and intensifies, particularly around the leading edge and the surface of the airfoil, as the AoAs increase towards and beyond the stall angle.

Figures 4.21, 4.22, 4.23, 4.24, 4.25, and 4.26 show the kinetic energy during various stages ($\alpha = 16.1°$, $18.0°$, $20.3°$, $22.3°$, $23.8°$, and $24.2°$) of the ramp-up dynamic stall motion for the full and partial surface roughness cases. These roughness height values include $k_r/c = 1.5 \times 10^{-3}$ (full) and (partial), $k_r/c = 3.6 \times 10^{-3}$ (full) and (partial), and $k_r/c = 7.9 \times 10^{-3}$ (full) and (partial). Following the pattern of the previously presented results, the kinetic energy contours are relatively similar for $k_r/c = 1.5 \times 10^{-3}$ (full) and (partial) across most AoAs. It is until the higher AoAs of $\alpha = 23.8°$ and $24.2°$, that a slight discrepancy is observed in the development with the

$k_r/c = 1.5 \times 10^{-3}$ (full) case displaying a slightly faster movement of the DSV. Furthermore, for the $k_r/c = 3.6 \times 10^{-3}$ cases and $k_r/c = 7.9 \times 10^{-3}$ cases, similar behavior in the kinetic energy is observed for the low AoAs. But as the AoAs increase, there is a greater discrepancy between the full and partial surface roughness cases. It is interesting to note that at $\alpha = 16.1°$, $k_r/c = 3.6 \times 10^{-3}$ (full) and (partial) and $k_r/c = 7.9 \times 10^{-3}$ (full) and (partial) exhibit two LSBs in their developments that is associated with local flow reattachment. Figure 4.21(b), (c), (e), and (f) show two small eye-shaped curves near the leading-edge region to illustrate this point. The accumulation of kinetic energy shown above the airfoil, especially in the upper middle to end region of the airfoil and the general trailing-edge region, is greater for the partial surface roughness cases compared to the full surface roughness cases. Starting at $\alpha = 20.3°$, the kinetic energy accumulation above the airfoil surface for $k_r/c = 7.9 \times 10^{-3}$ (full) starts to display a sizable reduction in magnitude of the kinetic energy, indicating a reduced DSV strength, compared to $k_r/c = 7.9 \times 10^{-3}$ (partial). The differences in the results are even more conspicuous at higher AoAs. It can further be concluded that the change in the kinetic energy is quicker for the full surface roughness cases, and even more so at the higher roughness values of $k_r/c = 3.6 \times 10^{-3}$ and $k_r/c = 7.9 \times 10^{-3}$. This behavior corresponds to the quicker progression of the DSV events that are occurring. But at higher AoAs, like at $\alpha = 23.8°$, and $24.2°$, it is clear that $k_r/c = 3.6 \times 10^{-3}$ (full) and and $k_r/c = 7.9 \times 10^{-3}$ (full) exhibit a weaker concentration of kinetic energy near and above the airfoil surface compared to their partial counterparts. This difference is even more pronounced between the $k_r/c = 7.9 \times 10^{-3}$ (full) and (partial) cases.

Overall, the trends indicate that as the roughness height increases, and as the roughness impacted area increases, the kinetic energy weakens. The results presented in these kinetic energy contour plots supplement the dynamic stall development behavior presented in subsection 4.4.4. Previously, the spanwise-averaged C_p plots in Fig. 4.9 for $k_r/c = 3.6 \times 10^{-3}$ (full) and $k_r/c = 7.9 \times 10^{-3}$ (full) indicated that the DSV is developing much quicker in these cases and the results also exhibit a weaker C_p magnitude compared to their partial counterparts. Together, they support the differences in the development of the dynamic stall for smooth and roughened airfoils.

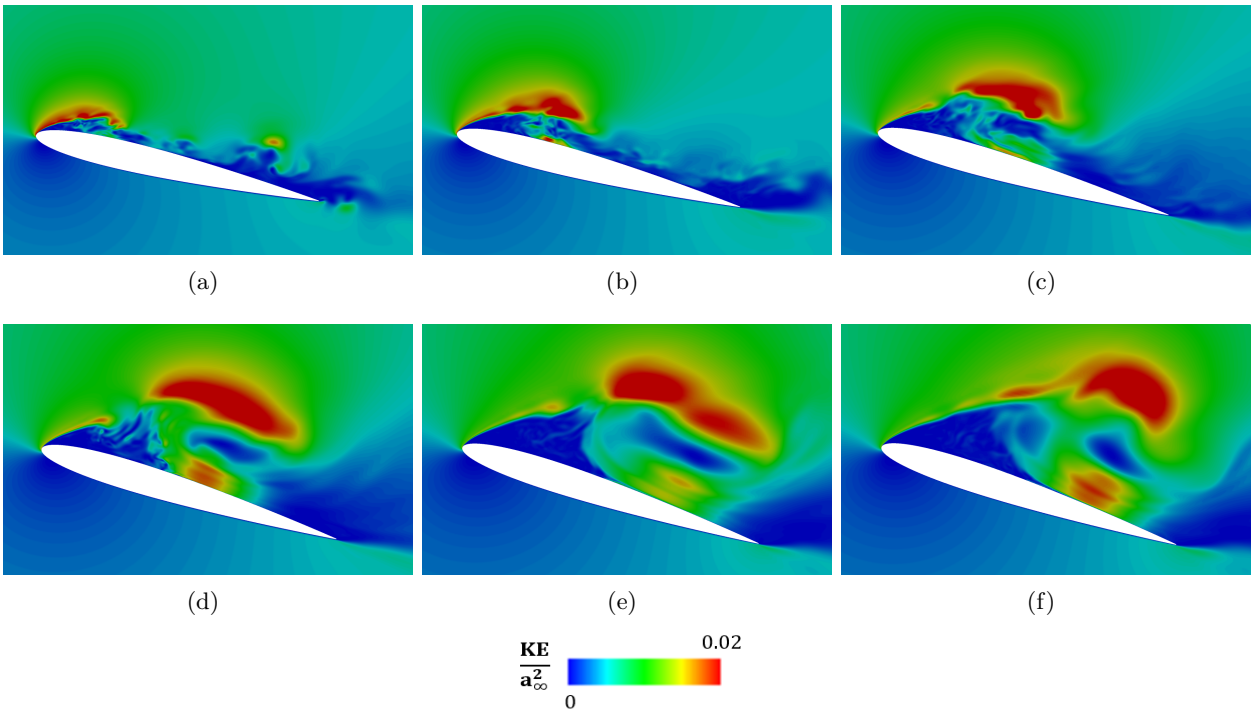

FIGURE 4.20. Kinetic energy contours for the baseline (smooth) case at α: (a) 16.1°, (b) 18.0°, (c) 20.3°, (d) 22.3°, (e) 23.8°, and (f) 24.2°.

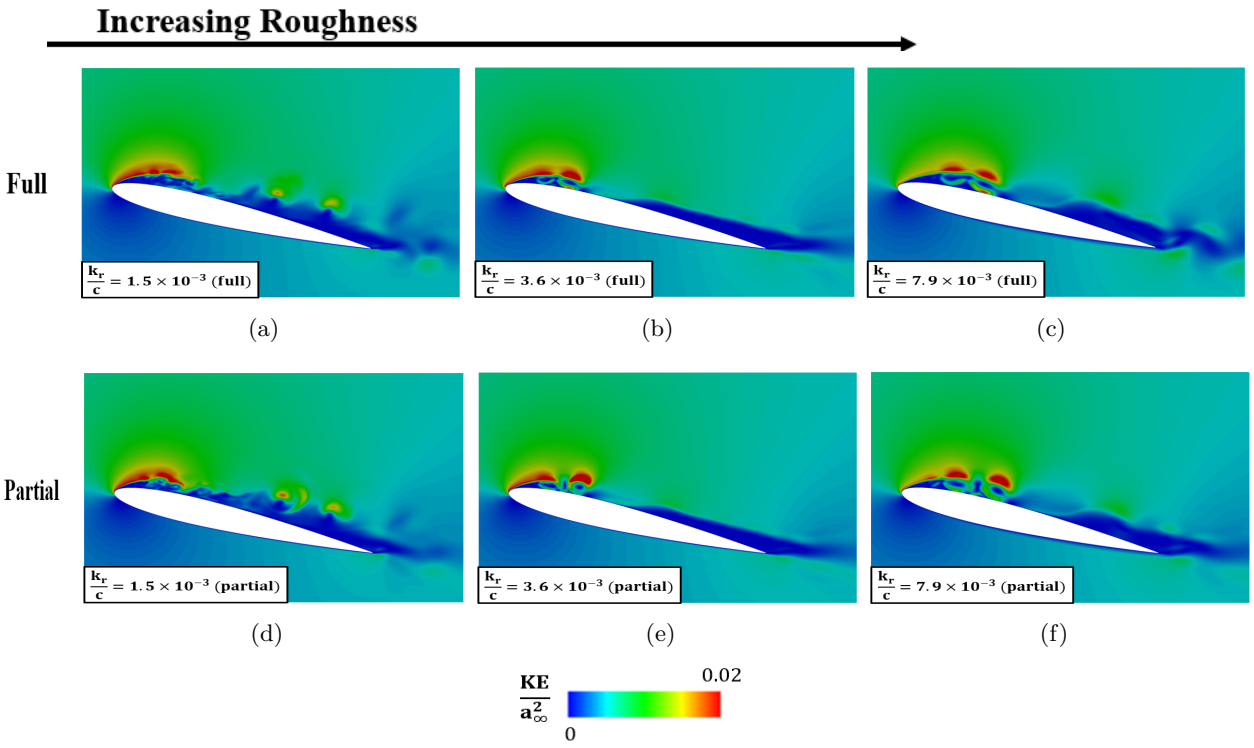

FIGURE 4.21. Kinetic energy contours at $\boldsymbol{\alpha}$ =16.1°.

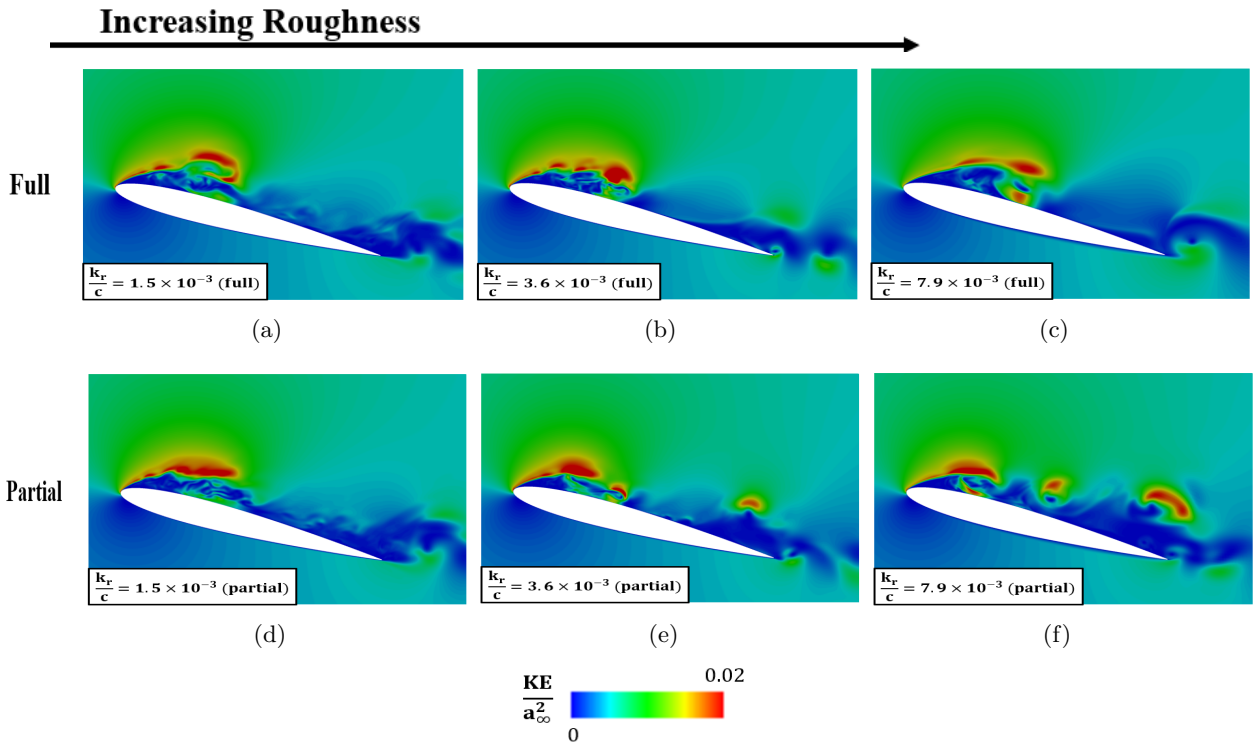

FIGURE 4.22. Kinetic energy contours at α =18.0°.

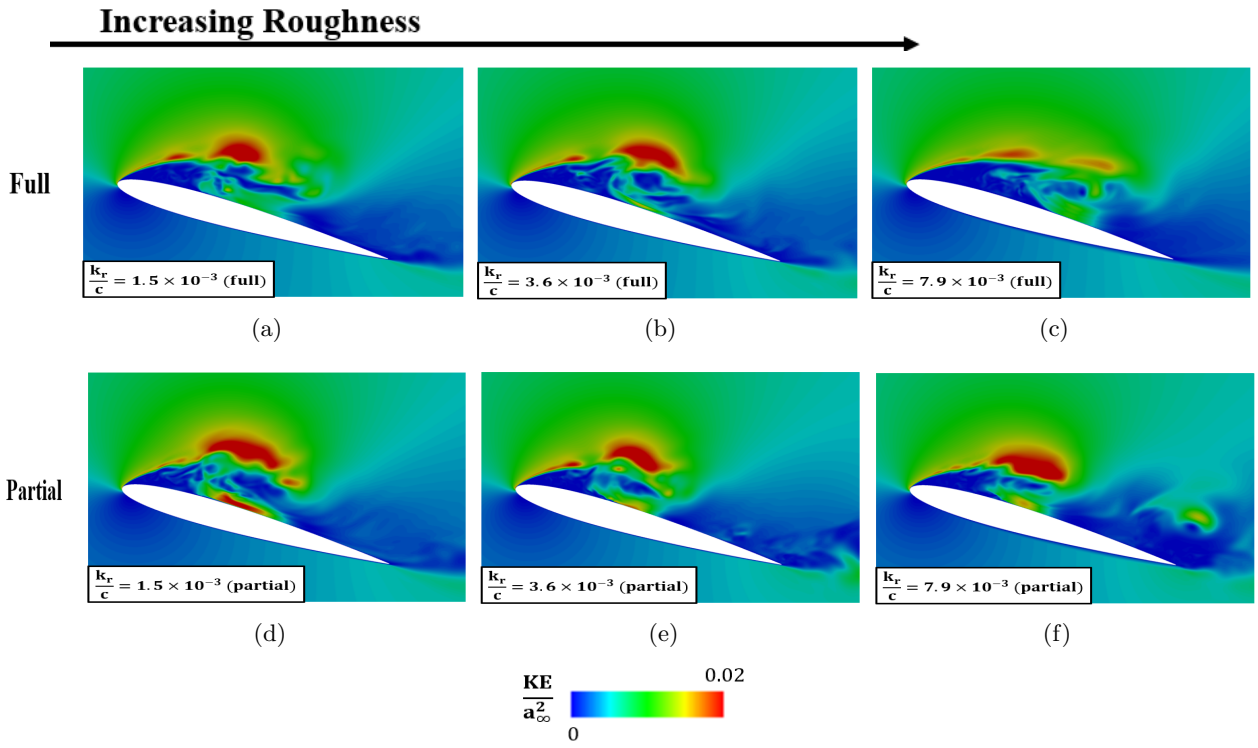

FIGURE 4.23. Kinetic energy contours at α =20.3°.

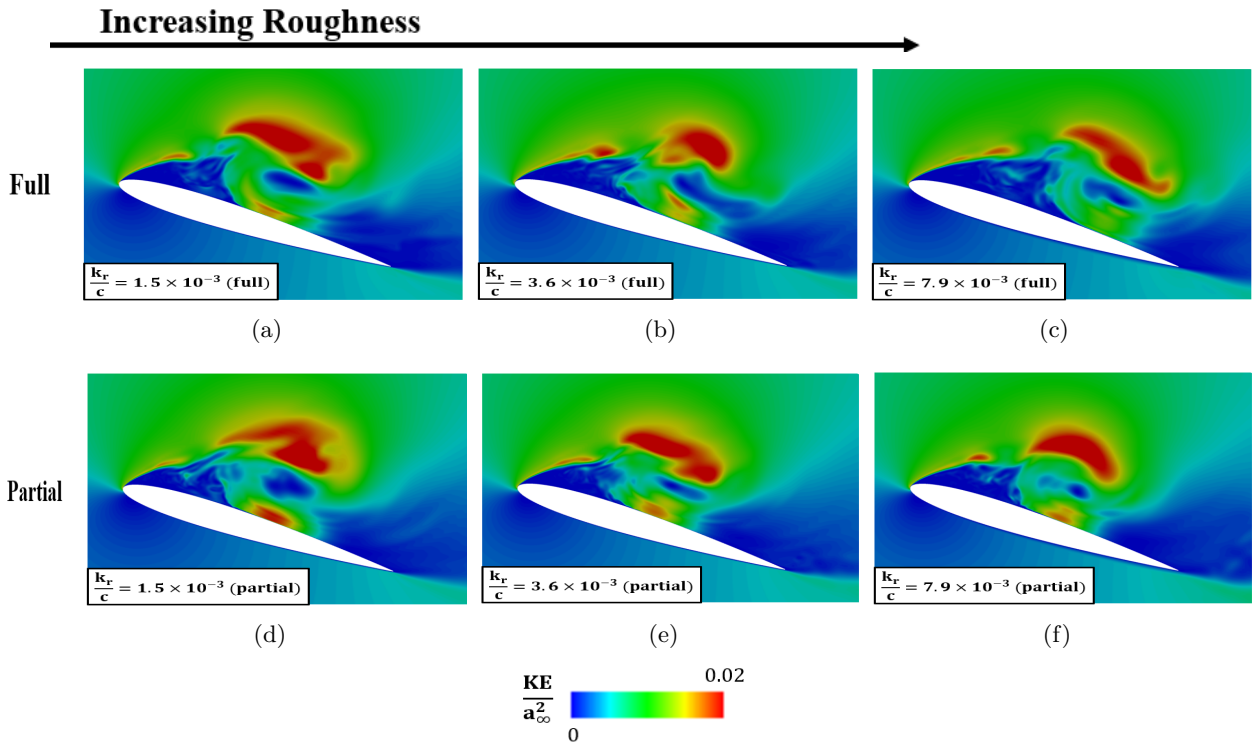

FIGURE 4.24. Kinetic energy contours at α =22.3°.

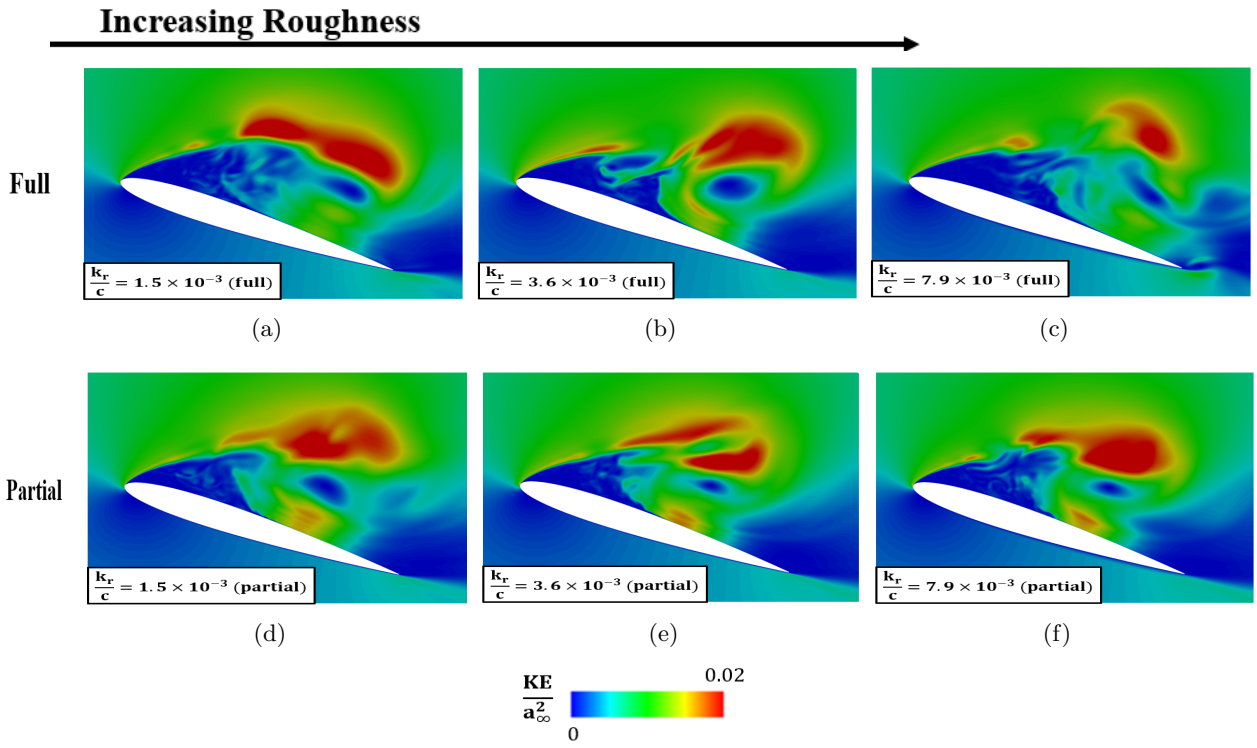

FIGURE 4.25. Kinetic energy contours at α =23.8°.

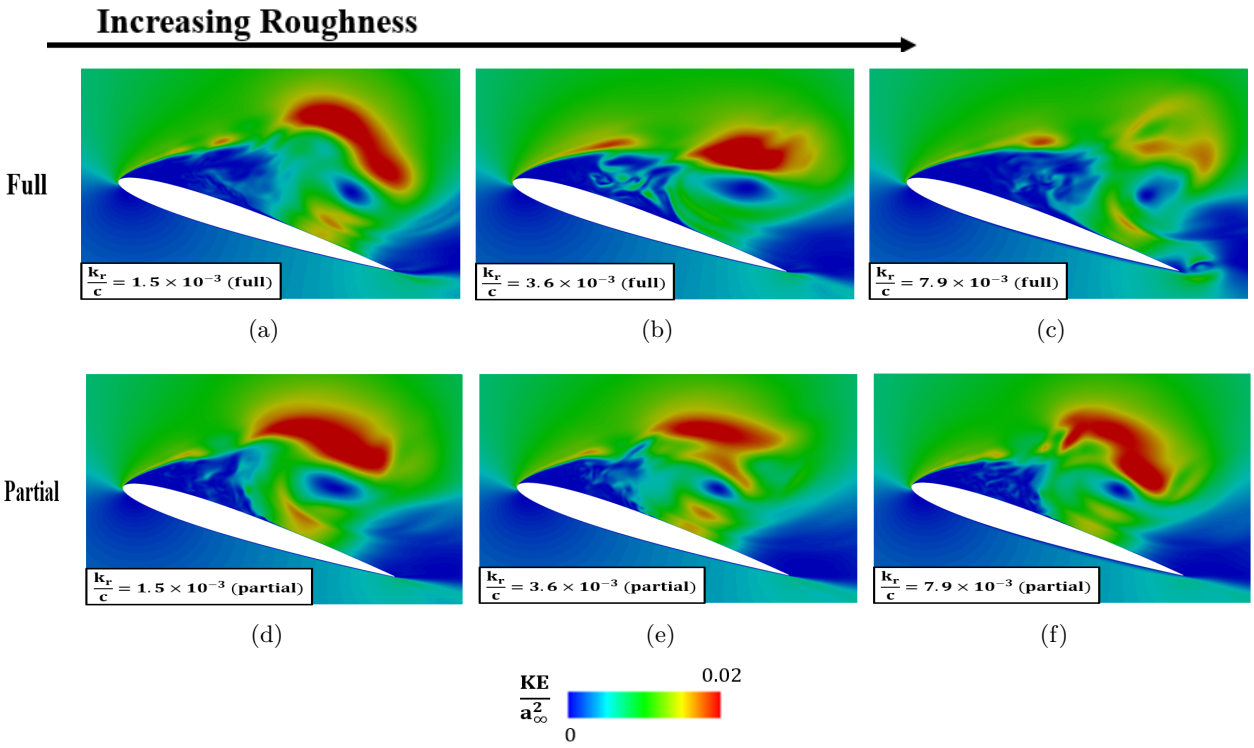

FIGURE 4.26. Kinetic energy contours at $\boldsymbol{\alpha}$ =24.2°.

4.5. Summary

This final chapter investigated and analyzed the effects of particle impact-induced surface roughness on dynamic stall, employing DDES coupled with the SST Langtry-Menter transitional turbulence model. DDES was utilized to predict the aerodynamic loads for a baseline NACA 0012 airfoil (smooth) and for airfoils with varying degrees of full and partial surface roughness. The roughness heights were determined in turbulent wall units. At the lower roughness height value, there is minimal difference in the lift (C_l), drag (C_d), and moment (C_m) coefficients between the full and partial surface roughness cases. However, as the roughness height increases, the differences in the peak magnitudes of C_l, C_d, and C_m between the full and partial surface roughness cases become more pronounced. Similarly, the disparity in the stall AoAs for the partial and full surface roughness cases widens with increasing roughness height. In summary, it can be concluded that the peak magnitudes of C_l, C_d, and C_m decrease more significantly in cases with full surface roughness compared to those with partial surface roughness. Furthermore, the stall AoA occurs earlier as the roughness height increases for the full surface roughness cases, whereas the stall AoA for the partial surface roughness cases remains relatively consistent with the baseline case.

The flow physics and kinetic energy dynamics were meticulously analyzed alongside the stages of dynamic stall development through the examination of vorticity magnitude and kinetic energy plots. The results for the full and partial surface roughness cases at lower roughness height values showed similarities. From the vorticity magnitude analysis, it was observed that as roughness height and its impacted area increase, smaller vortices near the leading edge disappear. This effect is particularly pronounced in the full versus partial surface roughness cases at higher AoAs. A critical observation was that higher roughness values in full surface roughness cases tend to precipitate stall behavior at an earlier AoA. The progression of the dynamic stall development stages are also much quicker for the higher values of full surface roughness. Furthermore, kinetic energy contour plots displayed relative similarities at lower AoAs. However, at higher AoAs, trends indicated that as roughness height and the area impacted by roughness increase, the kinetic energy accumulated above the airfoil diminishes. This reduction in kinetic energy is indicative of the reduced DSV strength due to increased surface roughness. Overall, the study demonstrated that varying levels of surface roughness and different impacted regions significantly alter the behavior, onset, and development of dynamic stall.

CHAPTER 5

Conclusions and Potential Future Work

5.1. Conclusions

This dissertation outlines the findings in my PhD research, which includes the notable results in the three content chapters on the effect of airfoil design parameters, effect of airfoil trailing-edge morphing, and the effect of particle impact induced surface roughness on dynamic stall.

The first content chapter presented a comprehensive numerical analysis of parametric airfoil design. Initially, the validation of the numerical simulations in predicting the C_l, C_d, and C_m against experimental data for a NACA 0012 airfoil was performed. Following the validation, an extensive analysis was undertaken for the six distinct design variables. The analysis revealed that the camber exerted the most significant effect on the peak values of both the C_l, and C_m. The boat-tail angle exhibited a more pronounced effect on the peak values of the C_m than on the C_l. Furthermore, the camber and thickness were found to have the largest effect on the lift and moment stall AoAs. The boat-tail angle and trailing-edge camber demonstrated the smallest effect on these parameters. Most notably, a deeper investigation on the effect of the boat-tail angle has been performed. It was found that a positive alteration in the boat-tail angle scaling factor continues to greatly reduce the pitching moment, while concurrently sustaining a comparable lift coefficient. In conjunction with the design parameter investigation, a sophisticated sensitivity analysis utilizing Morris' method was executed to systematically evaluate the quantitative impacts of these parameters on the dynamic stall characteristics. The findings acknowledged that the thickness crest position is a critical parameter influencing both the C_l and C_m and their stall AoAs. Ultimately, this design parameter study and sensitivity analysis have identified and ranked the key design parameters in relation to their impact on dynamic stall.

The next content chapter investigated and analyzed the effect of trailing-edge morphing on dynamic stall using DDES with a transitional turbulence model. DDES was used to predict the aerodynamic loads for a baseline NACA 0018 airfoil and trailing-edge morphed airfoils with Δb

equal to 3 and 4. In the morphed cases, the C_m magnitude decreased more significantly compared to C_l. Overall, C_l was reduced by 0.7% and C_m by 7.8% for the Δb=3 case compared to the baseline airfoil. C_l was reduced by 2.7% and C_m by 8.3% for the Δb=4 case. Additionally, C_l was reduced by 4.9% and C_m by 9.1% for the baseline case compared to the Δb=-3 case. The dynamic stall development stages were discussed in detail through analyzing the dynamic stall stages and general flow physics. The results indicated that the behavior of the secondary shear layer (in the high x/c range) intensified as the trailing edge boat-tail angle scaling factor (Δb) was implemented. Additionally, the Δb=4 case exhibited the earliest bursting of the LSB, resulting in the faster movement and earlier onset of the DSV compared to the Δb=3 and baseline cases. Also, the Δb=-3 case exhibited the earlier onset and a larger DSV compared to the Δb=3 and baseline cases. As the AoA increased, there was a gradual increase in the boundary layer thickness. The flow separation near the trailing edge and the trailing-edge vortex also grew during the increase in vorticity production. The exact behavior of how the trailing-edge separation encountered the LSB and influenced the bursting of the LSB was examined in the reverse flow contours. Overall, it was demonstrated that a small change in the trailing edge could have a global effect on the dynamic stall process.

The final chapter investigated and analyzed the effects of particle impact-induced surface roughness on dynamic stall, employing DDES coupled with the SST Langtry-Menter transitional turbulence model. DDES was utilized to predict the aerodynamic loads for a baseline NACA 0012 airfoil (smooth) and for airfoils with varying degrees of full and partial surface roughness. The roughness heights were determined in turbulent wall units. At the lower roughness height value, there is minimal difference in the lift (C_l), drag (C_d), and moment (C_m) coefficients between the full and partial surface roughness cases. However, as the roughness height increases, the differences in the peak magnitudes of C_l, C_d, and C_m between the full and partial surface roughness cases become more pronounced. Similarly, the disparity in the stall AoAs for the partial and full surface roughness cases widens with increasing roughness height. In summary, it can be concluded that the peak magnitudes of C_l, C_d, and C_m decrease more significantly in cases with full surface roughness compared to those with partial surface roughness. Furthermore, the stall AoA occurs earlier as the roughness height increases for the full surface roughness cases, whereas the stall AoA for the partial surface roughness cases remains relatively consistent with the baseline case.

The flow physics and kinetic energy dynamics were meticulously analyzed alongside the stages of dynamic stall development through the examination of vorticity magnitude and kinetic energy plots. The results for the full and partial surface roughness cases at lower roughness height values showed similarities. From the vorticity magnitude analysis, it was observed that as roughness height and its impacted area increase, smaller vortices near the leading edge disappear. This effect is particularly pronounced in the full versus partial surface roughness cases at higher AoAs. A critical observation was that higher roughness values in full surface roughness cases tend to precipitate stall behavior at an earlier AoA. The progression of the dynamic stall development stages are also much quicker for the higher values of full surface roughness. Furthermore, kinetic energy contour plots displayed relative similarities at lower AoAs. However, at higher AoAs, trends indicated that as roughness height and the area impacted by roughness increase, the kinetic energy accumulated above the airfoil diminishes. This reduction in kinetic energy is indicative of the reduced DSV strength due to increased surface roughness. Overall, the study demonstrated that varying levels of surface roughness and different impacted regions significantly alter the behavior, onset, and development of dynamic stall.

5.2. Potential Future Work

Regarding the work on the surface roughness in Chapter 4, my future work can involve quantifying the particle impact induced surface roughness on the airfoil. In my current study, I have identified the strike impact regions and implemented a predefined particle induced surface roughness height value using the lowest angle and highest angle. But future work can implement other cases where the roughness zone is time-dependent with dynamic interaction between the particle trajectory and flow through a two-way coupling method. Additionally, it is known that the leading edge and the frontal regions of the airfoil is subjected to higher levels of impact damage compared to the other rear regions of the airfoil. Therefore, future work in this area can also include quantifying the specific damage in each of these critical impacted regions. The goal is to provide more realistic results on the effect of this surface roughness damage during the dynamic stall motion. These surface roughness cases can also be simulated under a different pitching motion or in other flow setup conditions. Additionally, the recent release version of OVERFLOW 2.4c would be able to handle values of greater roughness heights in the fully rough regions. More work can be done in

this subject area to investigate the effect of roughness height values of the turbulent boundary layer in the logarithmic layer. Previously, the Knopp wall roughness model could only be implemented in OVERFLOW 2.3, 2.4a, and 2.4b for the SST-2003 (2-eq) model (DDADI left-hand side), and SST-2003 model (SSOR left-hand side), and SST-2003 model with Langry-Menter transition model (SSOR left-hand side). Now, OVERFLOW 2.4c has enabled the Knopp wall roughness model for the Wilcox $k-\omega$ turbulence model, and has improved force and moment calculation with non-zero turbulent eddy viscosity at the boundaries to accommodate the surface roughness models. Most notably, the Wilcox $k-\omega$ turbulence model has the option to increase the roughness height much further beyond $y^+ = 60$ or 70 extending into the fully rough zone. These new implementation options and new models are worth exploring and validating in future research works.

The theme of my research work is on studying the effect of airfoil design parameters and investigating the impacts of surface roughness on dynamic stall. Other future research topics can focus and continue to build on this theme. I would like to extend on this theme and investigate the effects of surface deformation on flight performance in unsteady fluid dynamics. I have studied unsteady fluid dynamics in single phase flow and clean airflow in my past and current research. For the next phase of my research, I am interested in studying the effects of unsteady fluid dynamics in multiphase flow as well as investigating the unsteady fluid dynamics in other harsh and extreme environments and weather conditions with particles. Today's flight vehicles must be able to maintain controllability and be capable of withstanding the rapid unsteady motion associated with unsteady flows with particles. The presence of sand, rain, ice, and other particles could impose penalties to the aerodynamic efficiency and performance of an aircraft or fluid dynamics machinery. Moving airborne devices and fluid-dynamic machinery may undergo dynamic stall in rainy or sandy conditions, or in other inclement weather conditions. I believe it is important to evaluate and analyze the multiphase flow effects of particles occurring in harsh and extreme environments. The significance of the results could then be applied in the airfoil design process. There needs to be more research done in this field to find reliable ways to mitigate the adverse effects of dynamic stall in all environments and scenarios.

I look forward to continuing my research in these topics in my future career.

5.3. Other Works

In the summer of 2020, I interned in the Thermal/Fluid Science & Engineering Department at Sandia National Laboratory. During that summer internship, I implemented an Alternative Fuels Risk Assessment Models (AltRAM) toolkit to model propane. The toolkit includes fast-running models for the unconstrained (i.e., no wall interactions) dispersion and flames for non-premixed fuels. Originally, the models were developed for use with hydrogen, but the toolkit was expanded to include other fuels, like propane and methane. I performed validation work for the physics models of propane. Specifically, my work involved predicting and modeling the flame length and width, heat flux and radiation, trajectory, and dispersion profiles for propane flames. I also set up a solver to calculate pressure and mass flow rates for choked and unchoked flow conditions. Ultimately, the results of my work have been published in the Journal of Process Safety and Environmental Protection and I have been listed as a co-author in that journal paper [31]. The purpose of this published chemical engineering journal paper is to help inform users of the toolkit on the range over which the fuel models are validated as well as give an indication of when the fuels are over- or under-predicting quantities of interest from the models.

CHAPTER 6

Publications

- **J.G.Shum**, S. Lee, K. Salari, R.C. McCallen, "Effect of Particle Impact Induced Surface Roughness on Dynamic Stall using Delayed Detached Eddy Simulations", AIAA Aviation Forum, Las Vegas, NV, July 29-August 2, 2024. [89]
- **J.G.Shum** and S. Lee, "Computational Study of Airfoil Design Parameters and Sensitivity Analysis for Dynamic Stall", AIAA Journal, Vol. 62 (4), April 2024, pp. 1611-1617. [85]
- **J.G.Shum** and S. Lee, "Numerical Investigation of the Effect of Trailing-Edge Morphing on Dynamic Stall using Delayed Detached Eddy Simulations", AIAA Paper 2023-3892, AIAA Aviation Forum, San Diego, CA, June 12-16, 2023. [88]
- Q. Guo, E.S. Hecht, M.L. Blaylock, **J.G.Shum**, and C. Jordan, "Physics Model Validation of Propane and Methane for Hydrogen Plus Other Alternative Fuels Risk Assessment Models (HyRAM+)", Journal of Process Safety and Environmental Protection, Vol. 173, May 2023, pp. 22-38. [31]
- **J.G.Shum** and S. Lee, "Effect of Airfoil Design Parameters on Deep Dynamic Stall under Pitching Motion", AIAA Paper 2023-1029, AIAA SciTech, National Harbor, MD, January 23-27, 2023. [87]
- **J.G.Shum** and S. Lee, "Computational Fluid Dynamics Best Practices for 2D Dynamic Stall Predictions", AIAA Paper 2020-2743, AIAA Fluid Dynamics Conference, Virtual Event, June 15-19, 2020. [86]
- S. Lee and **J.G.Shum**, "Prediction of Airfoil Trailing Edge Noise Using Empirical Wall Pressure Spectrum Models", AIAA Journal, Vol. 57 (3), March 2019, pp. 888-897. [51]
- S. Lee and **J.G.Shum**, "Validation of Empirical Wall Pressure Spectrum for Airfoil Trailing Edge Noise Predictions", AIAA Paper 2018-3791, 24th AIAA/CEAS Aeroacoustics Conference, Atlanta, GA, June 25 – 29, 2018. [52]

APPENDIX A

PARFOIL (Additional Equations)

The purpose of this Appendix A page is to further provide the detailed equations for thickness crest position, trailing-edge camber, and boat-tail angle design parameters presented in Chapter 2 Section 2.2.3.

When there is a change in the position of the camber or thickness crest, the difference in the airfoil horizontal coordinate, denoted as Δy, is added to the baseline value for both the leading-edge and trailing-edge regions. The same polynomial function can be employed to describe the changes in the airfoil coordinates for these two crest positions. For instance, the change in the position of the thickness crest can be mathematically represented as:

$$y_x = y + \Delta y_x \tag{A.1}$$

where

$$\Delta y_x = C_3(y - x_0)^3 + C_2(y - x_0)^2 + (x_1 - x_0) \tag{A.2}$$

$$C_2 = -\frac{(x_1 - x_0)(1 - 3x_0 + 3x_0^2)}{(1 - x_0)^2 x_0^2} \tag{A.3}$$

$$C_3 = \frac{(x_1 - x_0)(1 - 2x_0)}{(1 - x_0)^2 x_0^2} \tag{A.4}$$

Note that in the above expressions, x_0 and x_1 are the thickness crest positions of the baseline and the morphed airfoil, respectively. Furthermore, y is the horizontal coordinate of the airfoil and Δy_x is the change in the horizontal coordinate resulting from the change in the thickness crest position.

When the trailing-edge camber changes in magnitude (Δn) or its crest position moves from a baseline value q_0 to an updated value q_1 (in this study, both q_0 and q_1 are fixed at 0.8), the corresponding change (Δt_n) of the airfoil thickness (t) is added to the baseline vertical coordinates in the trailing-edge region. The updated trailing-edge camber in morphed airfoil geometries can be obtained as follows:

$$t_n(y) = t(y) + \Delta t_n \tag{A.5}$$

1) For $y_R \leq y \leq q_1$

$$\Delta t_n = D_3(y - q_1)^3 + D_2(y - q_1)^2 + \Delta n \tag{A.6}$$

$$D_2 = -\frac{3\Delta n}{(q_1 - y_R)^2} \tag{A.7}$$

$$D_3 = -\frac{2\Delta n}{(q_1 - y_R)^3} \tag{A.8}$$

2) For $q_1 \leq y \leq 1$

$$\Delta t_n = E_2(y - q_1)^2 + \Delta n \tag{A.9}$$

$$E_2 = -\frac{\Delta n}{(1 - q_1)^2} \tag{A.10}$$

In the above expressions, y_R is the reference position that represents a boundary point of the trailing-edge region. In this work, y_R is set to $0.60c$, where c stands for the airfoil chord length.

Similarly, when the boat-tail angle changes in magnitude (Δb), the thickness (t_b) due to a change in boat-tail angle is modified for the trailing-edge region as follows:

(A.11) $$t_b(y) = t(y) + \Delta t_b$$

where

(A.12) $$\Delta t_b = \Delta b \cdot \frac{(y - y_R)^4}{(y_B - y_R)^4} \frac{(y-1)}{(y_B - 1)}$$

In the above expressions, y_B is the horizontal position where the boat-tail angle is measured, and y_B is set to 0.80c in this study.

APPENDIX B

NACA0012 Airfoil Mesh Generation and Turbulence Model Selection

The following information in this chapter of the Appendix further elaborates on the details relating to mesh generation and numerical scheme presented in subsections 2.2.4 and 2.2.5 in the Methodology section of Chapter 2.

B.1. 2-D vs. 3-D Mesh Generation

This section discusses the necessity of choosing a 3-dimensional (3-D) airfoil mesh for the mesh generation method presented in Chapter 2 on investigating the effect of airfoil design parameters. I have generated 2-D and 3-D NACA 0012 airfoil meshes and I have also conducted simulations using 2-D RANS and compared them with 3-D RANS results. The comparison shown below in Fig. B.1 highlights a discrepancy in the accuracy of the 2-D predictions, particularly near the peak where the results are overestimated. Notably, the 2-D simulations incorrectly indicate a higher peak and suggest the presence of a stronger secondary stall behavior for the drag and pitching moment coefficients that is absent in both experimental data and 3-D RANS simulations. Additionally, the locations of the stall AoAs for the 2D simulations also occur at an earlier AoA compared to the 3-D simulations and the experimental data. In light of these findings, it is the belief that 3-D RANS is essential for capturing the unsteady dynamic stall behavior accurately.

B.2. Turbulence Model Selection

This section discusses the necessity of choosing a transitional turbulence model as part of the numerical scheme approaches presented in Chapter 2 on investigating the effect of airfoil design parameters. I have conducted additional simulations comparing the transition model with the fully turbulent model, as shown below in Fig. B.2. The results and analysis suggest that the transition model is crucial in capturing the nuances of dynamic stall development, even at this high Reynolds number. The primary objective of these simulations is to align the peaks of the

lift, drag, and moment coefficients, along with their corresponding stall angles of attack (AoAs), with experimental data. In the results obtained from the fully turbulent model, one can observe an overprediction in the peaks of the lift and drag coefficients. Additionally, the magnitude and extent of the primary dynamic stall event are also overestimated. The pitching moment coefficient exhibits a significant secondary stall behavior, which is absent in both the experimental data and the results from the transitional model. Moreover, the stall AoAs for the lift, drag, and pitching moment coefficients are predicted to occur at higher AoAs in the fully turbulent model. Based on these findings, it can be concluded that the transitional model is not only necessary but also reliable for this flow setup condition.

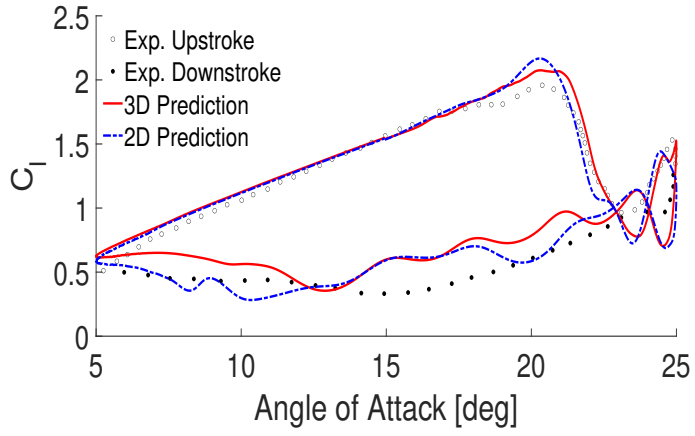

(a)

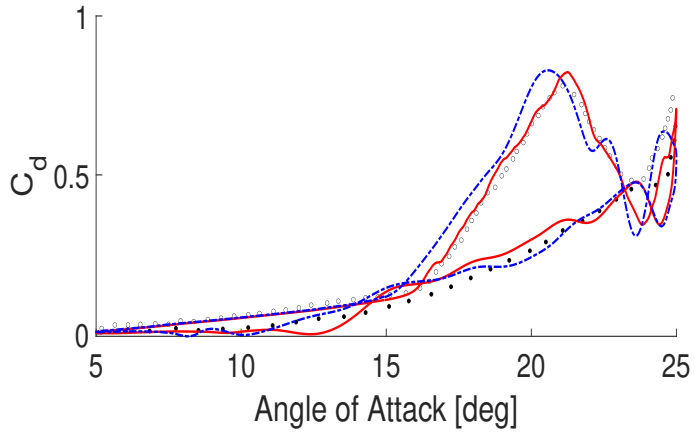

(b)

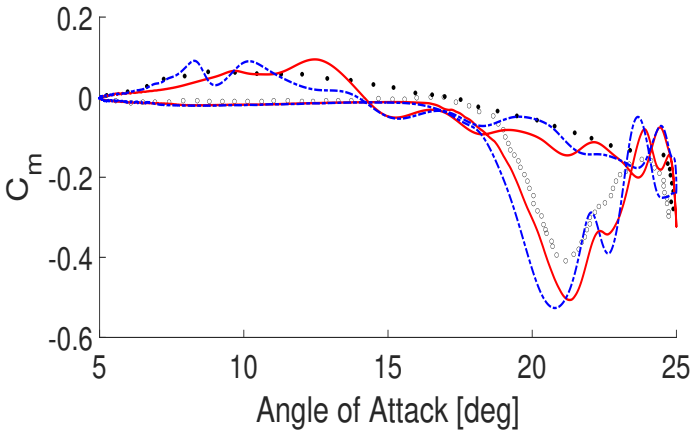

(c)

FIGURE B.1. Comparison of the aerodynamic loads for baseline airfoil undergoing a sinusoidal pitching motion generated from a 2-D and 3-D airfoil mesh: (a) coefficient of lift, (b) coefficient of drag, and (c) coefficient of pitching moment.

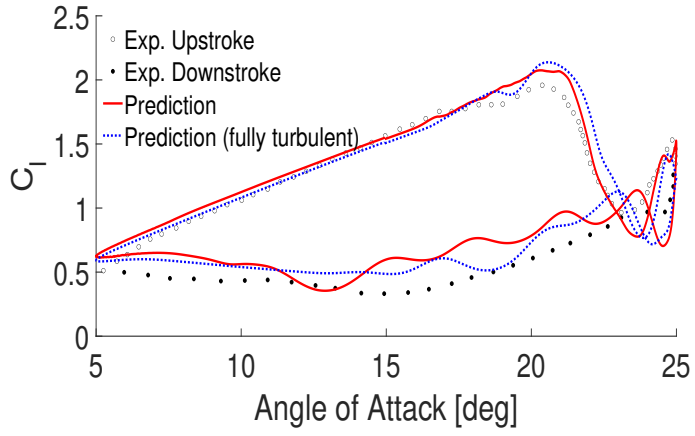

(a)

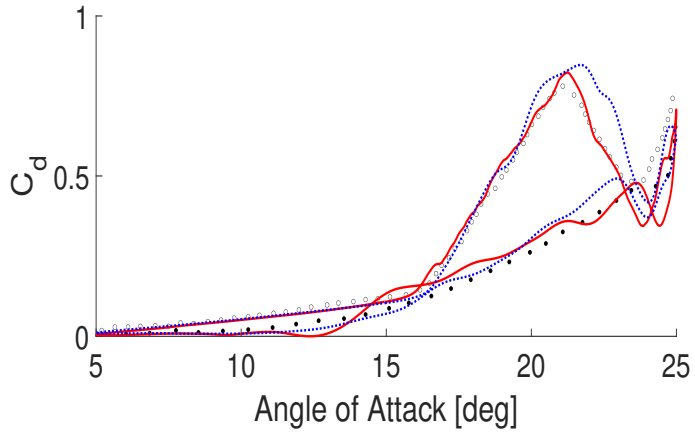

(b)

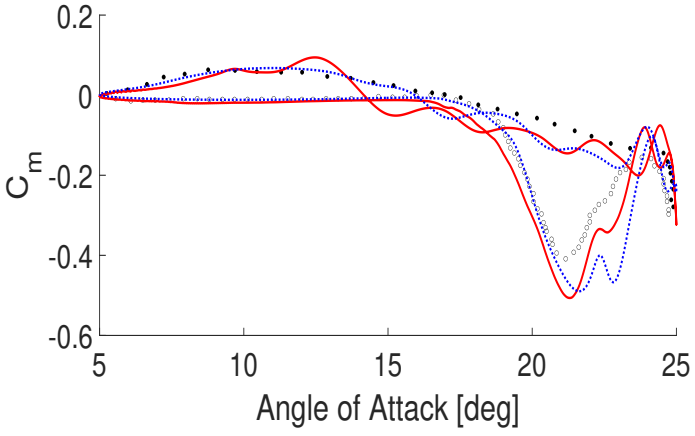

(c)

FIGURE B.2. Comparison of the aerodynamic loads for baseline airfoil undergoing a sinusoidal pitching motion for a transitional model and fully turbulent model: (a) coefficient of lift, (b) coefficient of drag, and (c) coefficient of pitching moment.

Bibliography

[1] I. H. Abbott and A. E. Doenhoff. *Theory of Wing Sections*. Dover Publications, Inc., 1959.

[2] S. M. Awadh. Impact of north african sand and dust storms on the middle east using iraq as an example: Causes, sources, and mitigation. *Atmosphere*, 14(1), 2023.

[3] R. Barger. Procedures for the design of low-pitching moment airfoils. NASA TN D-7982, 1975.

[4] J. Batther and S. Lee. Numerical investigation of a pitching airfoil undergoing dynamic stall using delayed detached eddy simulations. *Computers & Fluids*, 249, 2022.

[5] J. Batther and S. Lee. Investigation of dynamic stall leading-edge flow features at a low transitional reynolds number. In *Proceedings of the 78th Annual Forum of the Vertical Flight Society*, Vertical Flight Soc., Fairfax, VA, May 10–12, 2022.

[6] S. I.. Benton and M. R. Visbal. The onset of dynamic stall at a high, transitional reynolds number. *Journal of Fluid Mechanics*, 861:860–885, 2019.

[7] S. I. Benton and M. R. Visbal. Effects of compressibility on dynamic-stall onset using large-eddy simulation. *AIAA Journal*, 58(3):1194–1205, 2020.

[8] W. G. Bousman. A qualitative examination of dynamic stall from flight test data. *Journal of the American Helicopter Society*, 43(4):279–295, 1998.

[9] J. M. Brandon. Dynamic stall effects and applications to high performance aircraft. NASA Tech. Rep. AGARD R-776, March 1991.

[10] L. Brevault, M. Balesdent, N. Bérend, and R. Le Riche. Comparison of different global sensitivity analysis methods for aerospace vehicle pptimal design. In *10th World Congress on Structural and Multidisciplinary Optimization*, Orlando, FL., May 19-24, 2013.

[11] S. Cant. High-performance computing in computational fluid dynamics: progress and challenges. *Phil. Trans. R. Soc. A*, 360:1211–1225, 2002.

[12] L. Carr and K. McAlister. The effect of a leading-edge slat on the dynamic stall of an oscillating airfoil. *Aircraft Design, Systems and Technology Meeting*, AIAA Paper 1983–2533, Oct. 1983.

[13] L. W. Carr. Progress in analysis and prediction of dynamic stall. *Journal of Aircraft*, 25(1):6–17, 1988.

[14] L. W. Carr, K. W. McAlister, and W. J. McCroskey. Analysis of the development of dynamic stall based on oscillating airfoil experiments. NASA TN D-8382, January 1977.

[15] T. Cebeci. Effects of environmentally imposed roughness on airfoil performance. NACA Contractor Report 179639, June 1987.

[16] N. M. Chaderjian. Numerical simulation of dynamic stall using near-body adaptive mesh refinement. *10th International Conference on Computational Fluid Dynamics (ICCFD10)*, Paper ICCFD10-102, July, 2018.

[17] W. Chakroun, I. Al-Mesri, and S. Al-Fahad. Effect of surface roughness on the aerodynamic characteristics of a symmetrical airfoil. *Wind Engineering*, 28(5):547–564, 2004.

[18] W. M. Chan. The overgrid interface for computational simulations on overset grids. *32nd AIAA Fluid Dynamics Conference*, AIAA Paper 2002–3188, June 2002.

[19] W. M. Chan, S. E. Rogers, S. A. Pandya, D. L. Kao, P. G. Buning, R. L. Meakin, D. A. Boger, and S. M. Nash. Chimera grid tools user's manual version 2.2. June, 2018.

[20] Carr L. W. Chandrasekhara, M. S. and M. C. Wilder. Interferometric investigations of compressible dynamic stall over a transiently pitching airfoil. *AIAA Journal*, 32(3):586–593, 1994.

[21] A. Choudhry, M. Arjomandi, and R. Kelso. Methods to control dynamic stall for wind turbine applications. *Renewable Energy*, 86:26–37, 2016.

[22] J. G. Coder. Enhancement of the amplification factor transport transition modeling framework. *55th AIAA Aerospace Sciences Meeting*, AIAA Paper 2017–1709, Jan. 2017.

[23] A. De Gaspari, L. Riccobene, and S. Ricci. Design, manufacturing and wind tunnel validation of a morphing compliant wing. *Journal of Aircraft*, 55:2313–2326, 2018.

[24] R. S. Ehrmann, E.B. White, D. C. Maniaci, R. Chow, C. M. Langel, and C.P. van Dam. Realistic leading-edge roughness effects on airfoil performance. *31st AIAA Applied Aerodynamics Conference*, AIAA Paper 2013–2800, June 2013.

[25] J. A. Ekaterinaris and M. F. Platzer. Computational prediction of airfoil dynamic stall. *Progress in Aerospace Sciences*, 33(11-12):759–846, 1998.

[26] L. E. Ericsson and J. P. Reding. Fluid dynamics of unsteady separated flow. part ii. lifting surfaces. *Progress in Aerospace Sciences*, 24(4):249–356, 1987.

[27] W. Geissler and H. Haselmeyer. Investigation of dynamic stall onset. *Aerospace Science and Technology*, 10(7):590–600, 2006.

[28] K Gharali and D.A. Johnson. Numerical modeling of an s809 airfoil under dynamic stall, erosion and high reduced frequencies. *Applied Energy Journal*, 93:45–52, 2012.

[29] B. Glaz, L. Liu, P. P. Friedmann, J. Bain, and L. N. Sankar. A surrogate based approach to reduced-order dynamic stall modeling. In *51st AIAA/ASME/ASCE/AHS/ASC Structures, Structural Dynamics, and Materials Conference*, Orlando, FL, April 12-15, 2010.

[30] R. B. Green and R.A.McD. Galbraith. An investigation of dynamic stall through the application of leading edge roughness. *The Aeronautical Journal*, 98:17–19, 1994.

[31] Q. Guo, E. S. Hecht, M. L. Blaylock, J. G. Shum, and C. Jordan. Physics model validation of propane and methane for hydrogen plus other alternative fuels risk assessment models (hyram+). *Process Safety and Environmental Protection*, 173:22–38, 2023.

[32] T. Guo, J. Jin, Z. Lu, D. Zhou, and T. Wang. Aerodynamic sensitivity analysis for a wind turbine airfoil in an air-particle two-phase flow. *Applied Sciences Journal*, 9(18), 2019.

[33] R. Gupta and P. J. Ansell. Unsteady flow physics of airfoil dynamic stall. *AIAA Journal*, 57(1):165–175, 2019.

[34] N. D. Ham and M. S. Garelick. Dynamic stall considerations in helicopter rotors. *Journal of the American Helicopter Society*, 13(2):49–55, 1968.

[35] H. H. Hu. Chapter 10: Computational fluid dynamics. In P.K. Kundu, I. M. Cohen, and D. R. Dowling, editors, *Fluid Mechanics (Fifth Edition)*, pages 421–472. 2012.

[36] W. W. Huebsch and A. P. Rothmayer. Effects of surface ice roughness on dynamic stall. *Journal of Aircraft*, 39(6):913–1103, 2002.

[37] R. Jain, A. Le Pape, A. Grubb, M. Costes, F. Richez, and M. J. Smith. High-resolution computational fluid dynamics predictions for the static and dynamic stall of a finite-span oa209 wing. *Journal of Fluids and Structures*, 78:126–145, 2018.

[38] Z. Jia and S. Lee. Impulsive loading noise of a lift-offset coaxial rotor in high-speed forward flight. *AIAA Journal*, 58(2):687–701, 2020.

[39] Z. Jia and S. Lee. Aerodynamically induced noise of a lift-offset coaxial rotor with pitch attitude in high-speed forward flight. *Journal of Sound and Vibration*, 491, 2021.

[40] Z. Jia and S. Lee. Computational study on noise of urban air mobility quadrotor aircraft. *Journal of the American Helicopter Society*, 67(1):1–15(15), 2022.

[41] Z. Jia and S. Lee. High-fidelity computational analysis on the noise of a side-by-side hybrid vtol aircraft. *Journal of the American Helicopter Society*, 67(2):1–14(14), 2022.

[42] Z. Jia, S. Lee, K. Sharma, and K. S. Brentner. Aeroacoustic analysis of a lift-offset coaxial rotor using high-fidelity cfd/csd loose coupling simulation. *Journal of the American Helicopter Society*, 65(1), 2020.

[43] J. Jin, Z. Lu, T. Guo, and Q. Li. Comparative study of dynamic stall between an aircraft airfoil and a wind turbine airfoil in an air-particle flow. *Applied Sciences Journal*, 11(22), 2021.

[44] B. Kayser, B. Gauvreau, and D. Ecotière. Sensitivity analysis of a parabolic equation model to ground impedance and surface roughness for wind turbine noise. *The Journal of the Acoustical Society of America*, 146(5):3222–3231, 2019.

[45] M. Kerho. Adaptive airfoil dynamic stall control. *Journal of Aircraft*, 44(4):1350–1360, 2007.

[46] N. M. Khalifa, A. Rezaei, and H. E. Taha. On computational simulations of dynamic stall and its three-dimensional nature. *Physics of Fluids*, 35(10), 2023.

[47] N. M. Khalifa, A. S. Rezaei, and H. E. Taha. Comparing the performance of different turbulence models in predicting dynamic stall. *AIAA SciTech Forum*, AIAA Paper 2021–1651, Jan. 2021.

[48] T. Knopp, B. Eisfeld, and J. B. Calvo. A new extension for k-ω turbulence models to account for wall roughness. *International Journal of Heat and Fluid Flow*, 30(1):54–65, 2009.

[49] C. L. Ladson, C. W. Brooks Jr., A. S. Hill, and D. W. Sproles. Computer program to obtain ordinates for naca airfoils. NASA TM 4741, December 1996.

[50] R. B. Langtry and F. R. Menter. Correlation-based transition modeling for unstructured parallelized computational fluid dynamics codes. *AIAA Journal*, 47(12):2894–2906, 2009.

[51] S. Lee and J. G. Shum. Prediction of airfoil trailing edge noise using empirical wall pressure spectrum models. *AIAA Journal*, 57(3):888–897, 2019.

[52] S. Lee and J.G. Shum. Validation of an empirical wall pressure spectrum model for airfoil trailing edge noise predictions. *24th AIAA/CEAS Aeroacoustics Conference*, AIAA Paper 2018-3791, June 2018.

[53] J. G. Leishman. *Principles of Helicopter Aerodynamics*. Cambridge University Press, second edition, 2006.

[54] H. Li and S. Guo. Aerodynamic efficiency of a bioinspired flapping wing rotor at low reynolds number. *R. Soc. Open Sci.*, 5(3), 2018.

[55] X. Li and L-H. Feng. Critical indicators of dynamic stall vortex. *Journal of Fluid Mechanics*, 937(A16), 2022.

[56] X. Li, K. Yang, J. Bai, and J. Xu. Effects of vortex generators on aerodynamic performance of thick wind turbine airfoils. *Journal of Wind Engineering and Industrial Aerodynamics*, 156(1):84–92, 2016.

[57] X. Li, K. Yang, J. Bai, and J. Xu. A new optimization approach to improve the overall performance of thick wind turbine airfoils. *Energy*, 116(1):202–213, 2016.

[58] N. D. Liggett and M. J. Smith. Temporal convergence criteria for time-accurate viscous simulations of separated flows. *Computers & Fluids*, 66:140–156, 2012.

[59] J. W. Lim. Application of parametric airfoil design for rotor performance improvement. In *44th European Rotorcraft Forum*, Delft, Netherlands, Sep. 18-21, 2018.

[60] J. W. Lim, L. D. Allen, R. B. Haehnel, and I. D. Dettwiller. An examination of aerodynamic and structural loads for a rotor blade optimized with multi-objective genetic algorithm. In *Proceedings of the 77th Annual Forum of the Vertical Flight Society*, Vertical Flight Soc., Fairfax, VA, May 10–14, 2021.

[61] H. Lin, C. Xu, C. Jiang, S. Hu, and C. Lee. Finite particle approach for high-fidelity simulation on helicopter brownout. *AIAA Journal*, 62(1):193–208, 2024.

[62] C. Liu and S. Lee. Parametric airfoil design and sensitivity analysis for turbulent boundary layer trailing-edge noise reduction. *AIAA Journal*, 60(4):2324–2341, 2022.

[63] C. Liu and S. Lee. Surrogate-based optimization for airfoil trailing-edge noise reduction using morphed trailing-edge shapes. In *Inter-noise Conference*, Seoul, Korea, August 23-26, August 23-26, 2020.

[64] H. Lomax. Lift developed on unrestrained rectangular wings entering gusts at subsonic and supersonic speeds. NACA-TN 2925, April 1953.

[65] K. W. McAlister, L. W. Carr, , and W. J. McCroskey. Dynamic stall experiments on the naca 0012 airfoil. NASA Report 1100, 1978.

[66] K. W. McAlister and L. W. Carr. Water tunnel visualizations of dynamic stall. *Journal of Fluids Engineering*, 101(3):376–380, 1979.

[67] K. W. McAllister, S. L. Pucci, and and Carr L. W. McCroskey, W. J. An experimental study of dynamic stall on advanced airfoil sections, volume 2. pressure and force data. NASA TM 84245, 1982.

[68] W. J. McCroskey. Unsteady airfoils. *Annual Review of Fluid Mechanics*, 14:285–311, 1982.

[69] W. J. McCroskey, L. W. Carr, and K. W. McAlister. Dynamic stall experiments on oscillating airfoils. *AIAA Journal*, 14(1):57–63, January 1976.

[70] W. J. McCroskey, K. W. McAlister, L. W. Carr, S. L. Pucci, O. Lambert, and R. F. Indergrand. Dynamic stall on advanced airfoil sections. *Journal of the American Helicopter Society*, 26(3):40–50, 1981.

[71] M. D. Morris. Factorial sampling plans for preliminary computational experiments. *Technometrics*, 33(2):161–174, 1991.

[72] R. Nichols and P. Buning. User's manual for overflow 2.2. University of Alabama at Birmingham, Birmingham, AL, 7 March 2019.

[73] C. Opp, M. Groll, H Abbasi, and M. A. Foroushani. Causes and effects of sand and dust storms: What has past research taught us? a survey. *Journal of Risk and Financial Management*, 14(7), 2021.

[74] L Piegl and W Tiller. *The NURBS Book*. Springer-Verlag, 2nd edition, 1997.

[75] V. Raul and L. Leifsson. Aerodynamic shape optimization for delaying dynamic stall of airfoils using cokriging regression. *AIAA SciTech Forum*, AIAA Paper 2021–0340, Jan. 2021.

[76] O. Reynolds. On the dynamical theory of incompressible viscous fluids and the determination of the criterion. *Philosophical Transactions of the Royal Society of London*, 186:123–164, 1895.

[77] C. L. Rumsey. Apparent transition behavior of widely-used turbulence. *International Journal of Heat and Fluid Flow*, 28(6):1460–1471, 2007.

[78] J. Sagaga and S. Lee. Performance, aerodynamics, and aeroacoustics of side-by-side rotors using high-fidelity computational fluid dynamics. *AIAA Journal*, 61(12):5429–5445, 2023.

[79] J. Sagaga and S. Lee. Acoustic predictions for side-by-side air taxi in full configuration. *AIAA Aviation Forum*, AIAA Paper 2023–4522, June 2023.

[80] K. Salari. Overview of llnl particletsim code. *LLNL-ABS-858016*, Nov., 2023.

[81] A. Saltelli, M. Ratto, T. Andres, F. Campolongo, J. Cariboni, D. Gatelli, M. Saisana, and S. Tarantola. *Global Sensitivity Analysis: The Primer*. Wiley, New York, 2008.

[82] A. Sharma and M. Visbal. Numerical investigation of the effect of airfoil thickness on onset of dynamic stall. *Journal of Fluid Mechanics*, 870:870–900, 2019.

[83] A. Sheidani, S. Salavatidezfouli, and P. Schito. Study on the effect of raindrops on the dynamic stall of a naca-0012 airfoil. *Journal of the Brazilian Society of Mechanical Sciences and Engineering*, 44(203), 2022.

[84] C Shih, L. Lourenco, L. Van Dommenelen, and A. Krothapalli. Unsteady flow past an airfoil pitching at a constant rate. *AIAA Journal*, 30(5):1153–1161, 1992.

[85] J. G. Shum and S. Lee. Computational study of airfoil design parameters and sensitivity analysis for dynamic stall. *AIAA Journal*, 62(4):1611–1617, 2024.

[86] J. G. Shum and S. Lee. Computational fluid dynamics best practices for 2d dynamic stall predictions. *AIAA Aviation Forum*, AIAA Paper 2020–2743, June 2020.

[87] J. G. Shum and S. Lee. Effect of airfoil design parameters on deep dynamic stall under pitching motion. *AIAA SciTech Forum*, AIAA Paper 2023–1029, Jan. 2023.

[88] J. G. Shum and S. Lee. Numerical investigation of the effect of trailing-edge morphing on dynamic stall using delayed detached eddy simulations. *AIAA Aviation Forum*, AIAA Paper 2023–3892, June 2023.

[89] J. G. Shum and S. Lee. Effect of particle impact induced surface roughness on dynamic stall using delayed detached eddy simulations. *AIAA Aviation Forum*, June 2024.

[90] M. L. Shur, P. R. Spalart, M. Kh. Strelets, and A. K. Travin. A hybrid rans-les approach with delayed-des and wall-modelled les capabilities. *International Journal of Heat and Fluid Flow*, 29(6):1638–1649, 2008.

[91] H. Sobieczky. Parametric airfoils and wings. In *Recent Development of Aerodynamic Design Methodologies, Springer Vieweg*, 1999.

[92] P. R. Spalart, S. Deck, M. L. Shur, Strelets M. Kh. Squires, K. D., and A. Travin. A new version of detached-eddy simulation, resistant to ambiguous grid densities. *Theoretical and Computational Fluid Dynamics*, 2006.

[93] P. R. Spalart, W-H. Jou, M. Strelets, and S. R. Allmaras. Comments on the feasibility of les for wings, and on a hybrid rans/les approach. *1st AFOSR International Conference on DNS/LES*, 1997.

[94] A. Tempelis and L. Mishnaevsky. Surface roughness evolution of wind turbine blade subject to rain erosion. *Materials & Design*, 231, 2023.

[95] H. Tennekes and J. L. Lumley. *A First Course in Turbulence*. MIT Press, 1972.

[96] T. Theodorsen. General theory of aerodynamic instability and the mechanism of flutter. NACA-TR 496, January 1949.

[97] K. T. Tran and P. He. Unsteady aerodynamic optimization of airfoils consideringshape and propeller parameters. *AIAA Aviation Forum*, AIAA Paper 2021–3033, Aug. 2021.

[98] Steven A. Tran, Manikandan Ramasamy, and Jayanarayanan Sitaraman. Experimental/computational study to identify sources of clusters in pitching airfoil measurements. *AIAA Journal*, 61(1):189–205, 2023.

[99] A. K. Travin, M. K. Shur, P. R. Spalart, and M Kh. Strelets. Improvement of delayed detached-eddy simulation for les with wall modeling. *European Conference on Computational Fluid Dynamics*, 2006.

[100] V. Udoewa and V. Kumar. Computational fluid dynamics. *Applied Computational Fluid Dynamics*, 2012.

[101] M. R. Visbal and S. I. Benton. Exploration of high-frequency control of dynamic stall using large-eddy simulations. *AIAA Journal*, 56(8):2974–2991, 2018.

[102] M. R. Visbal and D. J. Garmann. Analysis of dynamic stall on a pitching airfoil using high-fidelity large-eddy simulations. *AIAA Journal*, 56(1):46–63, 2018.

[103] P. Wernert, W. Geissler, R. Raffel, and J. Kompenhans. Experimental and numerical investigations of dynamic stall on a pitching airfoil. *AIAA Journal*, 34(5):982–989, 1996.

[104] F. M. White. *Fluid Mechanics 9th Edition*. McGraw-Hill Education, 2021.

[105] Y. Wu, Y. Dai, C. Yang, Y. Hu, and G. Huang. Effect of trailing-edge morphing on flow characteristics around a pitching airfoil. *AIAA Journal*, 61(1):160–173, 2023.

[106] Y. Zhang. Effects of distributed leading-edge roughness on aerodynamic performance of a low-reynolds-number airfoil: an experimental study. *Theoretical and Applied Mechanics Letters*, 8(3):201–207, 2018.

[107] C. Zhu, Y. Qiu, Y. Feng, T. Wang, and H. Li. Combined effect of passive vortex generators and leading-edge roughness on dynamic stall of the wind turbine airfoil. *Energy Conversion and Management*, 251, 2022.